ISSN 2435-1288

Nikon Research Report

Vol.2 2020

Purpose of publication

This publication is being created to widely introduce the achievements of research and development activities conducted by Nikon Corporation. This is a result of R&D based on Nikon's core technologies of "opto-electronics" and "precision" technologies that have been incorporated in new products and/or often valued by external organizations such as academic societies. At the end of the report, the papers presented and published by our engineers in the previous year are listed.

Foreword

Representative Director
President

Toshikazu Umatate

In today's globalized society, in 2020, we find ourselves in the midst of a pandemic the likes of which the modern world has never experienced. Rapid changes are required, and it is unavoidable that macroeconomic and social structures will be affected. However, I do not believe that the direction of business and technology needed for the future will fundamentally change. For Nikon, we think that the long-term growth area will remain the same, although there will be many aspects that must be moved up ahead of schedule. This has made us realize once again how critical it is to react quickly.

The ability to react quickly can only be acquired through the accumulation of everyday efforts. Nikon possesses two valuable core technologies: "opto-electronics technologies" and "precision technologies" which have been steadily built upon since the company was established. In addition, we will incorporate new technologies inside and outside the company, build up, refine, and make better preparations so that we can react immediately and realize the value unique to Nikon.

This year we will publish the second issue of The Nikon Research Report, which was first published in 2019. It reports on Nikon's achievements in which its accumulated technologies have expanded into areas of long-term growth for improving enterprise value. I am pleased to share some of the progresses Nikon has made through this report.

General Manager
Research & Development Division

Kazuhiro Kido

Now that the world is facing a great deal of difficulty, the way we think about technological values as well as their applications requires greater diversity and flexibility than ever before. Given these circumstances, we believe that the importance of communicating to everyone the development results at each Nikon research and development section is further increasing.

Continuing from last year, we are issuing the Nikon Research Report to widely disseminate the newest achievements of our research and development. This issue contains technical explanations of products released in 2019, and papers valued by external organizations during the same year. It also describes the successful results of applying the technologies cultivated since the company's foundation to Nikon's basic business, and the annual best in the field of theoretical research award received from the largest academic society in Japan, as an example of sophisticated technological achievements.

I hope that this report provides you with a deeper understanding of the technologies we are working on and an opportunity for you to widely utilize the results.

Nikon Research Report Vol.2
目次／ CONTENTS

技術解説/Technical Reports

研究開発論文/Research and Development Reports

技術解説

Technical Reports

ニコンZマウント用大口径レンズ NIKKOR Z 58mm f/0.95 S Noctの開発

坪野谷啓介，藤原　誠

Development of the NIKKOR Z 58mm f/0.95 S Noct Large aperture lens for the Nikon Z mount

Keisuke TSUBONOYA and Makoto FUJIWARA

2019年10月，「NIKKOR Z 58mm f/0.95 S Noct」を発売した．大口径・ショートフランジバックのニコンZマウントだからこそ実現できた開放F値0.95.「Noct」を冠したこの大口径レンズの設計思想は，1977年に発売された「AI Noct Nikkor 58mm f/1.2」に端を発している．ここでは，新生Noctに詰め込まれた新しい技術とニコンのDNAについて説明する．

The NIKKOR Z 58mm f/0.95 S Noct was launched in October 2019. It has a maximum aperture of f/0.95 which facilitates usage of the Z-mount, which has a large diameter and a short flange back. The design concept of the fastest lens, to which the term “Noct” was added, started with the AI Noct Nikkor 58mm f/1.2 launched in 1977. In this study, we explain a new technology and DNA of NIKON packaged into the new and updated “Noct.”

Key words ニコンZマウント，交換レンズ，大口径レンズ，ノクト，開放F値0.95
Nikon Z mount, Interchangeable lens, large aperture lens, Noct, maximum aperture 0.95

1 Introduction

The Nikon Z mount system lens “NIKKOR Z 58mm f/0.95 S Noct” was launched in October 2019 (Fig. 1).

Fig. 1　NIKKOR Z 58mm f/0.95 S Noct.

2 History of Development

The Nikon Z mount system has a maximum inner mount diameter of ϕ55 mm and a short flange back of 16 mm. With these features, this product demonstrates the potential of the Z mount by realizing both the highest peak performance of NIKKOR to date, and the brightness that surpasses the maximum aperture of f/1. In addition, this product is expected to open up new possibilities for visual expression.

3 Features of NIKKOR Z 58mm f/0.95 S Noct

The most remarkable features of the lens include the maximum f/0.95 ultra-large aperture, the fastest in NIKKOR history[*1], and a superior optical performance that alters the common knowledge of conventional large-aperture lenses. Aberrations, ghosting, and flares are suppressed through special glass materials for the optical system consisting of 17 lens elements in 10 groups, and by adopting the latest optical technologies such as ground Aspherical surface and ARNEO coat (Fig. 2).

Another major feature of the lens is that it is a manual focus lens. At f/0.95, which has an extremely shallow depth of field, the requirements for focus accuracy are extremely stringent. By matching the high-definition electronic viewfinder (EVF) of the Nikon Z mount camera with the manual

[*1] In interchangeable lens for Nikon camera

focus mechanism of this product, it is possible to exactly adjust the focus according to the intention of the photographer.

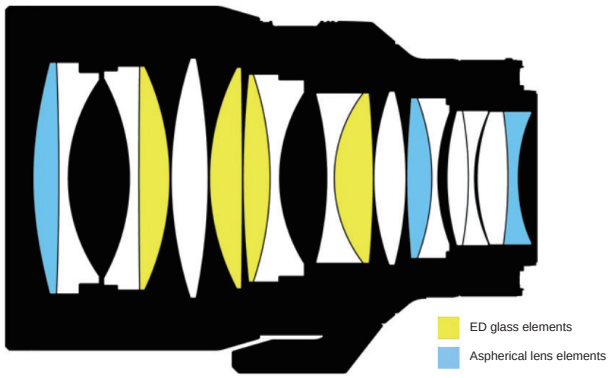

Fig. 2 Lens configuration diagram.

Moreover, it has a high-quality exterior design suitable for a lens that symbolizes the Nikon Z mount system. The details of these outstanding features are explained hereafter.

4 The World of Maximum Aperture f/0.95

"Spherical aberration is proportional to the cube of the aperture". This is the basis of the optical design derived from the third-order aberration theory[1]. In short, if the spherical aberration for f/2.8 is taken as 1, it will be approximately 2.8 times for f/2, 8 times for f/1.4, and approximately 25.6 times for f/0.95. Both f/2.8 and f/1.4 are said to have large apertures; hence, with this comparison alone, f/0.95 can be said to be far superior. Since the value of F is determined by "focal length ÷ effective aperture", F has a close physical relationship with the lens size and light exposure amount. According to the specifications, the effective aperture of f/0.95 is about $\sqrt{2}$ times that of f/1.4, and its exposure is about twice as bright. Further, as brighter F value corresponds to larger effective aperture size, the product size tends to increase. However, even if the focal length and the F value are the same, the product size may differ, as there are some uncertain aspects due to other factors, such as performance, mechanism, design, operability and so on.

A large aperture means the lens has a shallow depth of field and a large blur. There are four major factors that affect the blur size: the focal length of the lens, the F value, the shooting distance, and the distance between the subject and the blur target. Among these, the F value is the only one that does not affect the composition and can be easily set. Moreover, to create beautiful circular blurs in the illumination, vignetting of the lens is important. Even at maximum aperture, it is ideal to have no vignetting as it also has the adverse effect of increasing the lens size. In that respect, vignetting can be improved by stopping down. For example, if f/0.95 is narrowed down by 2 stops, it will still be less than f/2, and be able to achieve large circular blurs without vignetting. This also has the advantage of improving the resolution.

The need for a larger aperture is often questioned due to the improved high-sensitivity characteristics of the sensor and the focusing accuracy associated with the shallow depth of field. However, since lower sensitivity has a wider dynamic range and less noise than a higher one, the benefits of being able to shoot with low sensitivity are greater. Since the depth of field is approximately proportional to the F value, focusing with f/0.95 is extremely severe. However, the resulting picture is one that can only be enjoyed with the large aperture of f/0.95.

Finally, the F value is also related to the resolution limit. If the aperture is narrowed down, the resolution could deteriorate due to the influence of diffraction. The F value is related to the numerical aperture (NA) during image formation by the following equation:

$$NA = \frac{1}{2F} \quad (1)$$

As the F value becomes smaller, NA increases and the resolution becomes finer. If there are no aberrations, f/0.95 has the potential to achieve high resolution by itself.

5 What is Noct

Noct is derived from the word "Nocturne", and is named after the AI Noct Nikkor 58mm f/1.2 (hereinafter, AI Noct), released in 1977[2]. The AI Noct was commercialized as a lens suitable for night photography; a lens for night photography must satisfy the following two points: First, it must have a "bright large-aperture" that can ensure a higher shutter speed with appropriate ISO sensitivity. Second, "a point light source must be projected as a point (point image reproducibility)", which is essential. As an F mount, AI Noct has a brightness limit of f/1.2, and it has been devised to improve point image reproducibility by overcoming the sagittal coma flare that occurs in many large-aperture lenses. The NIKKOR Z 58mm f/0.95 S Noct (hereinafter, Z Noct) was also named Noct because it has a larger aperture, f/0.95, made possible with the Z mount, and can realize a more ideal point image reproducibility than the earlier version.

However, the reproducibility of ideal point image is possible due to the lens having "no aberration". This is because

it can capture a dot as a dot without the slightest of deviation. Further, it also enables the realization of an ideal blur. With no aberration, there exists no peculiarities in the front and rear blurs; the blurs are uniform and continuous. This is the purpose of Z Noct, with which actual shooting gives a strong impression of the three-dimensionality of the subject.

In the development of Z Noct, various restrictions and common practices that are inherent in the optical design are eliminated so that the optical specifications and performance are satisfied. Therefore, its size, price and performance are amazing.

6 Axis of Z Noct – Double Gauss Type

The optical system of Z Noct can be approximately divided into three parts, namely the front group, the master group, and the rear group. The front and rear groups are f/0.95, and they form an auxiliary optical system that provides the performance suitable for the new Noct. The master group, which is the core, is based on a famous optical system called the "double Gauss-type (hereinafter, Gauss-type)". Since the Gauss-type is often used in large-aperture standard lenses, AI Noct is also a Gauss-type lens, similar to many others. Further, the f/0.95 lenses released by other companies are also based on the Gauss-type. The characteristics of Gauss-type include good symmetry, excellent aberration correction, and high flatness of the image plane, which are the capabilities required for the point image reproducibility of Noct.

Symmetry is an important factor for aberration correction. In Z Noct, the general framework of the front, master and rear groups have a symmetrical structure, making the optical system more powerful in terms of aberration correction. Further, to achieve the target high-performance, the design of the Gauss-type Z Noct is different from the usual one in the way aberrations are corrected.

As its name suggests, the Gauss-type optical system is comprised of two Gaussian objective lenses, which can be schematically written as "convex-concave-concave-convex". A more general form is the six-element structure, "convex-convex-concave-concave-convex-convex". Although adopted in many large-aperture standard lenses, the biggest drawback of the Gauss-type is the aberration called sagittal coma flare, which requires some ingenuity. Since the Gauss-type has powerful concave surfaces facing each other, it can strongly correct spherical and coma aberrations, Petzval sum, and so on. In layman's terms, it is a method of "controlling poison with poison", and in exchange for correcting the lower order aberrations, sagittal coma flares of higher order aberrations occur. The means of avoiding this powerful concave surface include "increasing the number of lens elements", "increasing the refractive index", and "making the surface aspherical".

In AI Noct, the sagittal coma flare is improved mainly by "increasing the refractive index" and "making the surface aspherical"[2]. The former is a very useful method because the correction effect of all five Seidal aberrations can be obtained with a little change in the shape of the glass material. On the other hand, there is a tendency of an increase in the cost of glass material and worsening of chromatic aberrations. With aspherical surface, the aberration to be corrected changes depending on the location where the optical system is used. In AI Noct, by using a front lens with the largest luminous flux diameter, spherical and coma aberrations, as well as sagittal coma flares are effectively corrected. The disadvantage of aspherical lenses is its costly mass production, where the difficulty level depends on the size and required accuracy of the aspherical lens. Moreover, since many aspherical lenses are made by a glass molding method, there are also restrictions on the glass materials that can be used.

Moreover, Z Noct utilizes the "increase in the number of lens elements" in the front and rear groups to achieve high performance at f/0.95. Increasing the number of lens elements is an orthodox means to avoid the occurrence of aberration as much as possible by guiding the light rays straight without much bending. It is for the same reason that many existing large-aperture standard lenses also have optical systems where multiple lens elements are added to the Gauss-type. The unique feature of Z Noct is that the configurations added at the front and back are independent. This configuration has been made possible by making full use of the large aperture short flange back of the Z mount.

To achieve high performance without compromise, it is necessary to compensate for the deterioration due to chromatic aberration, which is a disadvantage of "increasing the refractive index". The influence of chromatic aberration is high in the master group and low in the front and rear groups. Therefore, high refractive index glass materials are used for the front and rear lens groups, giving priority to the correction of the five Seidal aberrations, while low refractive index and low dispersion ED lens elements are frequently adopted for the Gauss-type master group.

Although corrections of spherical aberrations and sagittal coma flares become difficult when using low refractive index lens elements for the Gauss-type, three ideas have been imple-

mented. The first is, reducing the load of aberration correction on the master group by adding the front and rear groups to share the aberration. The second is, using aspherical surfaces in each of the three groups to suppress the aberration amount occurring in each group, thereby suppressing the higher order aberrations at the same time. This is a usage opposite to that of AI Noct. The third is, making the cemented lens elements of the Gauss-type master group into old achromatic cemented lens elements, which is advantageous for spherical and coma aberration correction. (Old achromatic cemented lens: Cementing of lens elements where the concave lens has a higher refractive index than the convex lens. The opposite is called the new achromatic cemented lens).

Even with a normal Gauss-type lens, if an extra-low dispersion lens (ED lens) is used with an aspherical surface or an old achromatic cemented lens element, the same effect can be obtained. However, one thing that cannot be corrected is the Petzval sum, the cornerstone of field curvature, which is determined by the refractive power and refractive index of the surface. In many camera lenses, as the refractive index of the convex lens is high and that of the concave lens is low, the presence of a powerful concave surface is necessary for correction. The presence of ED lens for improving chromatic aberration, the presence of an old achromatic cemented lens for the correction of spherical aberration, and the relaxation in the powerful concave surface for the correction of sagittal coma flare contribute to increase in the Petzval sum, causing the occurrence of field curvature, and thus, impairing the image reproducibility. Therefore, in addition to having the front and rear groups share the aberration, Z Noct uses a new achromatic junction to eliminate this Petzval sum; it also has a strong concave surface.

Thus, at f/0.95, Z Noct overcomes sagittal coma flare, the weak point of Gauss-type, while improving chromatic aberration and point image reproducibility, and becomes the ultra-large aperture lens with the highest performance in history.

7 Ground Aspherical Surface

There are two new optical technologies that support the astonishing performance and specifications of Z Noct. One is the ground aspherical surface. Although the technology itself is not new, Nikon has updated it into a unique precision machining technology with high accuracy.

Recently the performance of camera lenses has improved remarkably, and aspherical surfaces have become an indispensable technology. Many camera lenses use aspherical surfaces, most of which are molded glass aspherical surfaces. The reason why ground aspherical surfaces are not often adopted is its complex mass production process due to the processing method. However, since the ground aspherical surface is very useful to improve the performance, it has become an indispensable part of Z Noct.

The advantage of the ground aspherical surface is its high degree of freedom in selecting glass materials. Restriction in the glass material corresponds to constraints in the control of light rays, and there are optical disadvantages such as failure to meet the performance goals. Because it is made by a thermoforming process, a molded glass aspherical surface can be created only with the glass molding materials. Meanwhile, as the ground aspherical surface, is made by a grinding process, any glass material where spherical surface processing is possible, can be adopted. Optically attractive glass materials that are not found in molding materials have high refractive index, as well as high and anomalous dispersion. The term “anomalous dispersion” used here includes not only the ED lenses having positive anomalous dispersion, but also the glass materials having negative anomalous dispersion. Although it is easy to understand that such characteristic glass materials can be made aspherical, the fact that other glass materials can be made similar is also important. The reason is, although camera lenses tend to have combinations and arrangements of glass materials for achromatism, regardless of those arrangements, aspherical lens elements are the most effective. Since high refractive index and chromatic aberration are key in Z Noct, it was necessary to make a glass material having a high refractive index and low dispersion as aspherical as possible. Further, it is also possible to achieve higher precision than with a molded glass aspherical surface. During the thermal process, various deformations and alterations occur. On the other hand, a ground aspherical surface is determined only by the machining accuracy. Although the ground aspherical lens element of Z Noct has a large lens diameter of f/0.95, it has high surface accuracy of submicron level (about 1/200th of the thickness of hair) over its entire surface. Z Noct is able to achieve high performance because of the presence of ground aspherical surface technology that enables the stable production of large lenses with high accuracy.

8 ARNEO Coat

Another new technology that supports the high performance and specifications of Z Noct is the newly developed anti-reflection coating, “ARNEO coat”. The characteristic of ARNEO coat is that it exerts a high suppression effect on

the reflection of light that is incident perpendicular to the lens surface[3] (Fig. 3).

The coating technology suppresses ghosts and flares by preventing reflection on the lens surface. If there is no coating, the light to be imaged will be blocked by reflection. Meanwhile, the reflected and incident light that would not have reached the imaging surface if it were the original optical path, will reach the imaging surface while being reflected multiple times inside the lens barrel, and be captured as the image. Some of the reflected light will diverge and appear as flares, whereas others converge and appear as ghosts. Naturally, if more light is taken in, together with Z Noct, ghosts and flares are more likely to appear.

As a result of pursuing high optical performance, Z Noct has a shape that guides light in a natural manner. In other words, this means that the incidence angle on the lens is often nearly vertical. Thus, without the ARNEO coat, it is impossible to obtain higher performance, as the configuration that guides the light in an unaffected manner must be compromised.

Since normal incidence is not limited to Z Noct, but can occur in any setting, ARNEO coat is expected to benefit many lenses. It can be said that by combining NIKKOR lens with Nano Crystal coating, which is strong against oblique incidence, omnidirectional cover has become possible.

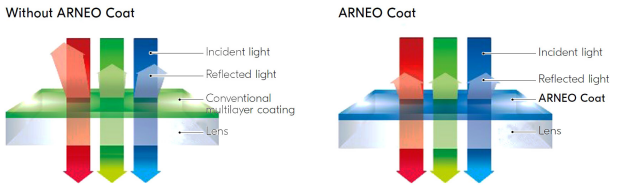

Fig. 3 Difference between conventional coat and ARNEO coat.

9 Manual Focus Mechanism

First, we will explain the reason why Z Noct is a manual focus lens.

The maximum aperture f/0.95 results in very shallow depth of field making focusing difficult. For example, when photographing a person obliquely with the eye as the focusing point, in the case of extremely shallow field depth of f/0.95, depending on whether you focus on the corner of the eye, pupil or the inner corner of the eye, the impression of the work may vary. In the case where a majority of the eye fits inside the focus-aid frame of the camera, the focus position can be determined only by the photographer. To maximize the optical performance of Z Noct, manual focus is considered to be the best.

There is also another reason. In reality, the focus lens group is so heavy that a practical autofocus mechanism cannot be constructed from the viewpoint of product size and focus accuracy.

For these reasons, when designing a manual focus mechanism, two main points must be considered: ① - The photographer must be able to focus as he/she desires, even with an extremely shallow field depth of the maximum aperture f/0.95, in other words, the operation resolution must be ensured. ② - Even with an extremely heavy focus lens, the photographer must be able to operate it easily, and the feel of the focus ring must be comfortable. In order to realize these two points, it was necessary to increase the rotation angle of the focus ring to reduce the lead angle of the helicoid mechanism used for driving the focus lens.

Therefore, to determine the required degree of operation resolution, the rotational operation that can perform the minimum movement was verified. Based on verifications of multiple people, from beginners to heavy camera users within our company, the amount of rotational operation that can move the focus ring at a minimum, regardless of the skill of the photographer, was confirmed to be about 0.5 mm in circumference. The change in focus for the amount of rotation operation of the focus ring was set to about 20 μm in terms of the image plane. This is based on the assumption that focusing by the photographer will not be stopped by continuous rotation operation, but rather by pitch operation, in which the focus ring is rotated gradually.

Based on this operation resolution, to absorb the focus shift due to the focus ring movement from infinity to the shortest shooting distance, temperature changes, manufacturing errors, etc., the amount of extreme rotation in both the infinity side and the near-side was secured. Consequently, the focus ring rotation angle was close to 360 degrees.

The other point was about the feel of the operation. It was assumed that with the above-mentioned focus ring rotation angle, anyone would feel the light operational torque. If the operation torque is too light, it may cause the camera to rotate more than what is intended by the photographer, and thus, proper focusing may fail to be performed. Moreover, for manual focus, a graceful feel with a certain weight tends to be preferred.

In Z Noct, the focus ring diameter is as large as ϕ102 mm. Therefore, for example, in order to obtain the same feel of operation (= tangential force) as a focus ring of ϕ70 mm, it is necessary to use an operating torque proportionate to the focus ring radius, which is about 1.5 times. Usually, a large amount of grease is applied to the helicoid part to give a

solid and graceful feel of operation. However, with a lens of this diameter, increasing the torque only with the grease amount is challenging, it is dealt with by providing a mechanism that applies a torque load by pressing the two parts that rotate inside the focus lens drive mechanism toward the optical axis. While ensuring a moderate operating torque by pressing in the direction of the optical axis, compared to conventional products, a graceful and smooth operation is realized by adjusting the grease amount and increasing the roughness of the sliding surface of the helicoid. Because a backlash removal effect due to the pressing is also obtained, the tracking delay of the focus lens with respect to the focus ring operation is eliminated, enabling precise focusing even during reversing operations.

10 Design

The design keyword of Z Noct that aims to express the highest optical performance and quality is “craftsmanship”. Because all the external parts are machined in metal and carefully finished one-by-one, it has both a high-quality texture and high part precision to maintain performance (Fig. 4). In addition, engraving the characters “Noct” in cursive style gives a special feeling that it has been made by a craftsman (Fig. 5) [4].

Fig. 4　Cut of cross-section.

The design of the functional parts can be appreciated as the core concept of Z system design that emphasizes operability.

In order to improve the finger grip, the focus ring has a wider pitch (perimeter) than the focus ring knurls of other NIKKOR Z lenses. If the pitch is made the same as that of other products, it will become slippery due to the large ring diameter. Further, by making the unevenness of the knurling clear, it was possible to give a more vivid impression. The

Fig. 5　“Noct” character engraving process.

tripod mount is designed in such a way that it does not interfere with the operation even when shooting handheld. Since it is better to have only a small number of components partially protruding from the lens barrel, the tripod mount is made as close to the lens barrel as possible, with the size also reduced. The tripod mount is designed such that it cannot be detached, and the locking mechanism was also eliminated. By doing this, it was possible to realize full functionality and operability, without disturbing the shape of the lens body. Although the ring width looks thin at first glance, sufficient rigidity is assured through the thickness of materials.

The lens hood of Z Noct has a round shape. By making the outer diameter the same as that of the lens barrel and mounting it on the tip of the focus ring, the lens hood itself is designed in such a way that it gives a sense of unity, as if it were a part of the lens barrel (Fig. 6). It gives a feeling of better balance between the total length and the outer diameter of the lens when the hood is attached. In addition to the lens hood’s original function of blocking light from outside of the view angle, the role of protecting the lens has also been considered. Although the focus lens of Z Noct is of a type that extends forward as it is focused, the lens hood is mounted on the tip of the focus ring and not on the tip of the lens as mentioned earlier, it covers the extending lens without moving back and forth; even in the most extended state, the lens does not protrude from the lens hood. This prevents accidental bumping of the extended lens tip. Moreover, rubber is installed on the tip of the lens hood to ensure the impact is less likely to be transmitted to the entire lens barrel during a hit. Further, it is designed such that even when placed face down, the lens hood does not slip easily or damage the other side. Such design concept is followed not only in Z Noct but also in all NIKKOR Z lenses.

Fig. 6　Product appearance with hood attached [5].

11 Summary

NIKKOR Z 58mm f/0.95 S Noct is a product made with thorough consideration of functionality, operability, and design, as well as the optical performance. Although it is large in size and heavy, making the manual lens difficult to shoot with, we hope you will greatly enjoy its performance and functions, and appreciate the joy of shooting. We wish that with the high-performance world of f/0.95, new visual expressions will be created.

By developing products that exceed customer expectations, we will continue to strive for the development of Nikon Z mount system, together with the development of camera and visual culture.

Reference

1) Yoshiya Matsui: Lens Design Method, 1 (Kyoritsu Shuppan, 1972) (in Japanese)
2) Koichi Oshita: "16th night AI Noct Nikkor 58mm F1.2". NIKKOR – The Thousand- and One-Nights Story. https://imaging.nikon.com/history/story/0016/index.htm, (Reference 2020-05-01)
3) Nikon Imaging Japan Inc.: "NIKKOR Z Technology". ARNEO coat. https://www.nikon-image.com/sp/nikkor_z/technology/ (Reference 2020-05-01) (in Japanese)
4) Nikon Corporation: "The design embodies a new dimension of optical performance". *Works*. https://www.nikon.co.jp/technology/design/works/nikkor_z_lenses.htm (in Japanese)
5) Toshihiko Sugimoto: "The unknown story of the development of the Large aperture mount NIKKOR Z (sequel)". *Digicame Watch*. https://dc.watch.impress.co.jp/docs/interview/1240053.html (in Japanese)

坪野谷啓介
Keisuke TSUBONOYA
光学本部
第三設計部
3rd Designing Department
Optical Engineering Division

藤原　誠
Makoto FUJIWARA
光学本部
第二開発部
2nd Development Department
Optical Engineering Division

光加工機 Lasermeister 100A/101A の開発

上野和樹

Development of the Lasermeister 100A/101A optical processing machine

Kazuki UENO

ものづくりに新たな市場と産業を創出することを目的に，従来の「大きい」「高価」「操作が複雑」という金属3D プリンターのイメージを刷新する光加工機「Lasermeister 100A」を2019年 4 月，さらに「5 軸化による造形制約の開放」「対応材料の拡充」に対応した「Lasermeister 101A」を2020年 5 月にリリースした．本稿では光加工機の基礎となる様々な開発要素について説明する．

In April 2019, Nikon released the optical processing machine Lasermeister 100A that renews the image of the conventional large, expensive, and complex-operation metal 3D printer with an aim of creating a new market and industry for manufacturing. Thereafter, the optical processing machine Lasermeister 101A was released in May 2020, which has features such as opening of molding restrictions by 5 axes and the expansion of compatible materials. This paper describes various developmental factors that form the basis of optical processing machines.

Key words 光加工機，金属3D プリンター，積層造形，レーザーメタルデポジション
optical processing machine, metal 3D printer, additive manufacturing, laser metal deposition

1 Introduction

In April 2019, Nikon released its first optical processing machine Lasermeister 100A, followed by its successor model Lasermeister 101A in May 2020. This paper describes various developmental factors that form the basis of optical processing machines.

2 Laser Metal Deposition

Nikon's first optical processing machine was created to open a new market and industry for manufacturing. The optical processing machine not only functions as a 3D printer capable of metal additive manufacturing, but also as a composite machine that uses light to perform operations such as improving the surface roughness of the modeled object by laser re-melting, and marking on a metal surface. Particularly, in the main feature, which is metal additive manufacturing, laser metal deposition (LMD) method is adopted instead of the generally used powder bed fusion (PBF) approach.

The PBF and LMD methods are explained in Fig. 1. In the PBF method, a metal powder material is preliminarily laid on a flat surface and sintered by scanning with laser; this process is repeated for each layer to form the modeled object. While it has the advantage of having a relatively good molding accuracy, the disadvantages include the limitation of being modeled only on certain standard base materials, and the large amount of metal powder used, while the molded object gets buried in the metal powder. Conversely, in the LMD method, first, a melt pool is formed by laser irradiation, followed by melting and solidifying while spraying the metal powder, which is repeated for each layer to form the molded object. The advantages include the possibility of additional processing regardless of the form of the base material, and the less amount of metal powder used, while the modeled object can be observed and confirmed from the outside, as it does not get buried in the metal powder. However, modeling accuracy is a problem.

"Lasermeister 100A/101A" employs the LMD method, which is considered to be reasonable with high future potential, and incorporates various development factors to improve modeling accuracy.

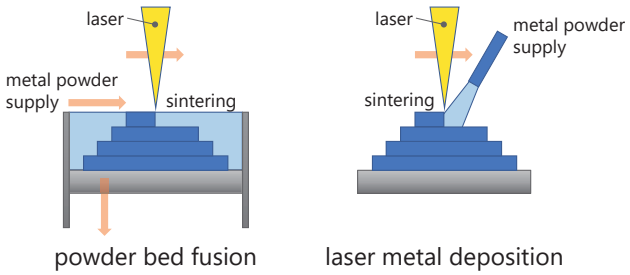

Fig. 1 Illustration of PBF (left) and LMD (right) methods

3 Usable Metal Power Materials and Safety

Lasermeister 100A can use the stainless-steel metal powder SUS316L to lower Mn, which is performed in consideration of the Ordinance on Prevention of Hazards Due to Specified Chemical Substances. Because the dust explosiveness evaluation revealed that it does not come under dangerous materials in the small gas flame ignition, the hurdle in its introduction is less. The equipment has also been evaluated for safety by a third-party certifying body, according to the European standards. By filling the process chamber with nitrogen gas during laser processing, we ease its use in consideration of high safety against an accidental dust explosion. Although invisible infrared laser is used as the processing light, the window provided on the front door has multiple light-shielding measures, and the laser product as a device has achieved Class I, regardless of the interior being visible. Therefore, from the viewpoint of laser equipment, it can be used safely. Furthermore, by developing a special recipe for Lasermeister 101A, it is made compatible with high-speed steel and nickel-based metals.

4 Miniaturization and Semiconductor Laser

The device dimension is W: 850 mm × D: 750 mm × H: 1700 mm, which is much more compact than conventional metal 3D printers, and thus, space saving is realized (Fig. 2). Because the laser and all other equipment are packaged in one housing, when power supply, together with exhaust and nitrogen gases, is provided, it can be operated on a standalone basis. The weight of the equipment excluding metal powder is 320 kg. The processing range of Lasermeister 100A is W: 297 mm × D: 210 mm (A4 size) × H: 200 mm, while that of the five-axes version, Lasermeister 101A, is ϕ150 mm × H: 150 mm.

As a point of miniaturization, the use of semiconductor lasers can be mentioned. Usually, a semiconductor laser used as a special light, such as a fiber laser, is directly used for processing through an optical lens barrel designed by Nikon. The maximum output is 200 W, and by using air cooling, the units surrounding the coolant are eliminated, which has greatly contributed to downsizing. Moreover, by utilizing the semiconductor exposure equipment development technology, the internal units are modularized by appropriate partitions to achieve both exterior design and functionality. An interface called the operator console is provided on the front of the device, and using the touch panel, operation and confirmation of device status by various sensors become possible.

Since a lightweight and compact device has been realized, it can be loaded into a normal elevator when bringing in, and be started up immediately after connecting the wiring and piping. Hence, it is highly mobilizable, as it can be installed anywhere.

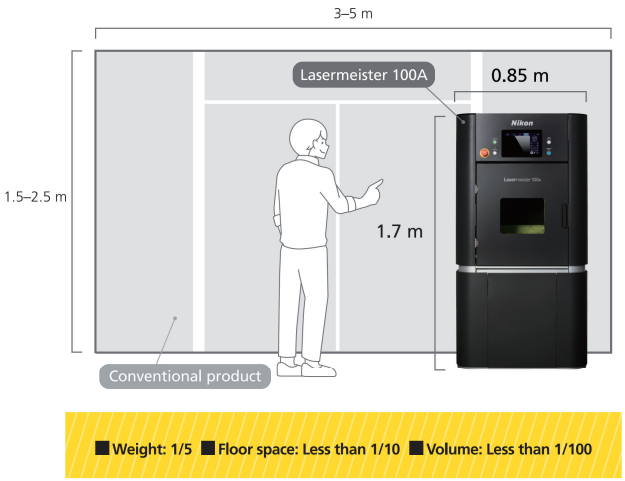

Fig. 2 Light and compact design.

5 Setup-less due to 3D Alignment

The greatest feature of Lasermeister 100A/101A is its 3D alignment function, which automatically positions the workpiece using a 3D scanner uniquely designed by Nikon and placed inside. Since there is no need for complicated positioning work after placing the base material to be processed, a setup-less process is achieved.

The process is explained step by step in Fig. 3. First, the machining base material and the 3D model of the product are prepared. Next, the machining base material is placed at an arbitrary position on the machining table. Conventionally, as a setup, the position of the machining base material placed on the machining table is measured with a stylus or the like, after fixing it with a jig. Conversely, in 3D

alignment, the coordinates of the machining base material are estimated by measuring the unique points using the built-in 3D scanner and matching them against the 3D model of the machining base. Based on it, by placing the 3D model of the machining base material at the recognized position on the machining table in the virtual space, the actual arrangement is reproduced on the computer. Furthermore, by placing the modeled 3D model at an arbitrary position on the 3D model of the machining base material, it is possible to easily perform additional processing at any desired position.

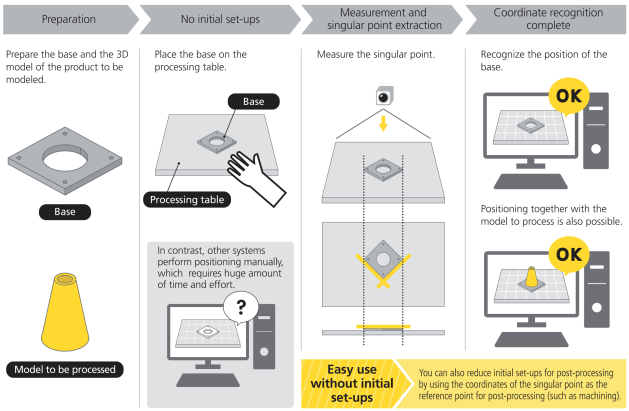

Fig. 3　3D alignment

Among the various methods, such as those of the optical cutting and time-of-flight, the 3D scanner employs the stereoscopic phase shift method. In this method, multiple stripe patterns are projected on to the measurement target through a projector, which is the light source, while the target shape is measured by a two-lens camera (Fig. 4). Since the base material, which is the measured object, is a metal, it is difficult to capture the reflected light, and there exist aspects where the measurement is challenging. However, the reason for choosing this method is that, in the evaluation of methods by comparison, measurement of a metal was relatively easy, and it was suitable in terms of the device size and measuring distance.

The basic process is straightforward with a simple graphical user interface via a touch panel, and the measurement, including the processing of measured data, can be completed in a short time. In addition, it has a function that teaches the manually machining the starting points more easily by using the two guide lights provided on the lens barrel, without using the 3D alignment, together with functions to teach multiple points and specify a virtual plane.

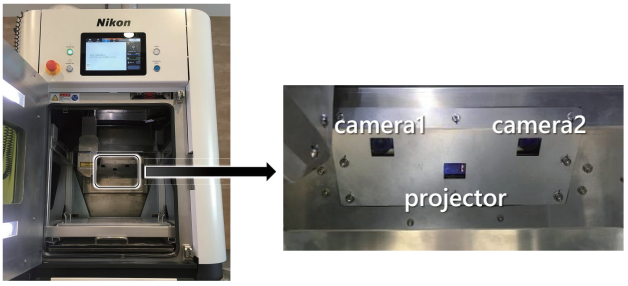

Fig. 4　Built-in stereoscopic phase shift 3D scanner

6 Changing to Five-axes and Relaxation of Modeling Restrictions

The details of the drive unit are described below. “Lasermeister 100A” is equipped with a gantry type XYZ orthogonal three-axes stage, and has a structure called processing head that drives the lens barrel and the powder supply nozzle. Lasermeister 101A is equipped with a tilt rotation stage that has two axes, with θx rotating around the X-axis, and θz around the Z-axis, and a five-axes configuration that drives the base material side. In each device, the machining path corresponds to the G code used in the NC program. Since Lasermeister 100A has a three-axes configuration, G code can be created manually. However, with the dedicated software installed in the device, it can be automatically generated using STL data, which is in 3D CAD file format. Using the function called slicer, a machining path can be generated for each layer at a fixed pitch in the height direction of the model. The optimized parameters for the driving speed of the processing head, the output of the laser, the rate of supply of the metal powder at that time, are automatically selected according to the material. Since, by providing the STL data, the user can perform modeling immediately without having to evaluate complex modeling recipes, and thus, a great convenience is realized. In addition, when performing additional processing on an existing part, it is possible to consider an arrangement in which the 3D model of the workpiece overlaps that of the machining base material. However, since the model difference extraction function is available, it can be easily used to repair missing parts. In the usual PBF-type metal 3D printer, when modeling an overhang shape as shown in Fig. 5, it is necessary to simultaneously model multiple pillar structures called the support material. This is to prevent sagging when melted by laser irradiation, as there is no base in the overhang portion. The support material is set by the user when generating the machining path for modeling. In addition to affecting the accuracy, the cutting and removing after modeling to make the final product takes huge effort.

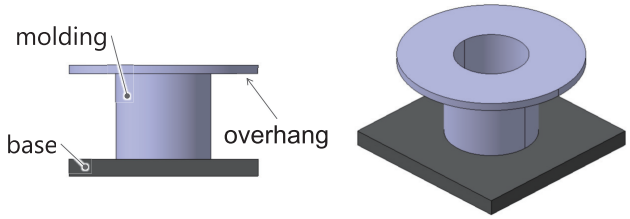

Fig. 5 Example of modeling an overhang shape

On the other hand, if LMD method and five axes are used, modeling without support is possible by performing tilting and rotation at the overhang part, as shown in Fig. 6. Although it is partially possible to model an overhang part protruding at an angle even with the three-axes type, since large angles cannot be obtained, the merit of using the five-axes type becomes large. In the case of five-axes machining, it is difficult to manually create the machining path. Hence, Lasermeister 100A/101A is compatible with some of the machining paths of five-axes machining CAM software.

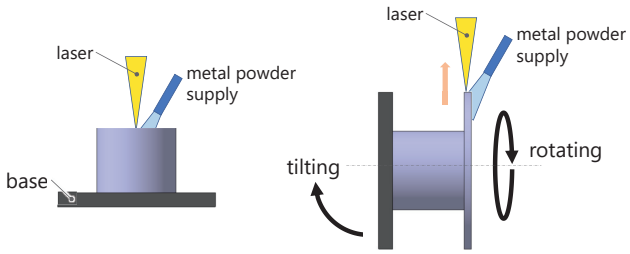

Fig. 6 Example of modeling an overhang shape by LMD five-axes modeling method.

7 Metal Powder Feeder

Although the LMD method has problems in terms of accuracy in general, one breakthrough is the stabilization of the rate of supply of metal powder.

This is only due to the material volume put into the melt pool. Forming the modeling bead with a stable volume leads to accuracy improvement of the final modeled object. In particular, the metal powder feeder is uniquely designed, and as shown in Fig. 7, it realizes metal powder feeding without a pulsation of even 5 mg in the short term.

A comparative image of the modeling bead that uses a powder feeder actually available in the market, and the modeling bead that uses the uniquely designed powder feeder, are shown in Fig. 8. This is a modeling bead formed by modeling multiple first layers in a line. It can be observed that the modeling bead eliminates fine cracks and difference in levels, and the stabilization of the rate of metal powder supply is directly linked to the modeling quality.

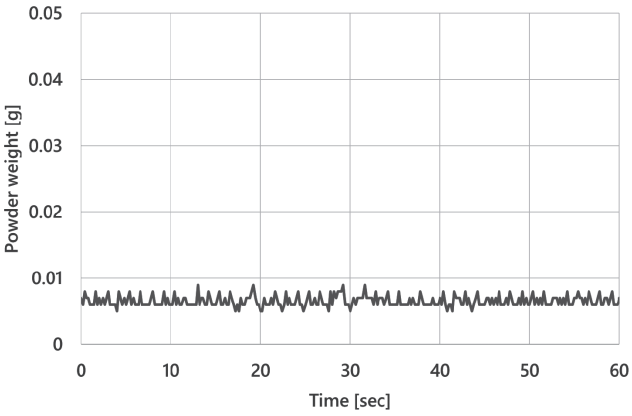

Fig. 7 Stabilization of the rate of metal powder supply by the original method.

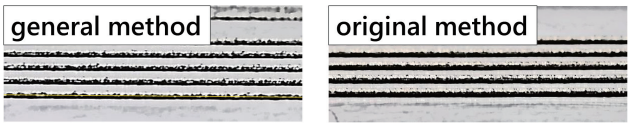

Fig. 8 Comparison of modeling beads

8 Feed-forward Control by Simulation

The shape of the modeling object has a great influence on the pursuit of modeling accuracy. Normally, it is difficult to automatically change the conditions for generating the machining path for the slicer according to the modeling shape. In Lasermeister 100A/101A, the parameters are automatically selected by a dedicated software, which can be converted into machining paths, while further optimization is also possible through a uniquely developed simulation. The mechanism is such that the optimal modeling parameters are calculated beforehand based on the simulation results, and the machining paths are adjusted directly.

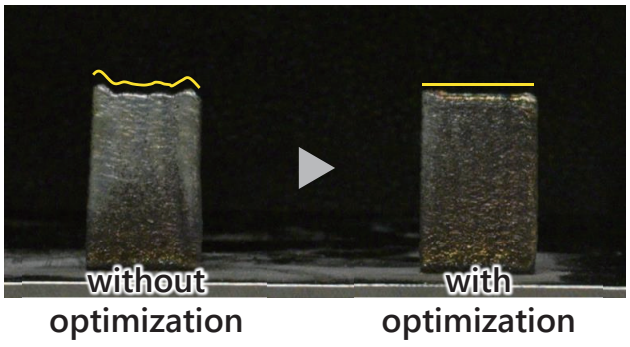

Fig. 9 Optimization of machining conditions and modeling accuracy.

Using this function to operate the device like a feed-forward control that reflects the modeling shape, the problem of modeling accuracy in the LMD method is resolved (Fig. 9).

9 Examples of Mechanical Characteristics of Modeled Objects

The mechanical characteristics of the modeled object become crucial when considering the final product. The mechanical characteristics of an in-house standard test piece, which is modeled using SUS316L powder, with the material used in Lasermeister 100A/101A being standard, is explained as follows.

JIS standard stainless-steel bars are used for reference and comparison. First, the results of the tensile test of the model without any processing, such as heat treatment, are given in Table 1. The sample size is set to five. It can be seen that the maximum stress, which is the 0.2% proof stress, and the elongation, meet the standard values for stainless-steel bars. Although there is no standard value, the Young's modulus is measured by the resonance method, as shown in Table 2. It can be seen that the numerical value is higher than that of the test piece modeled by the PBF method, and is almost comparable to that of the rolled material.

Table 1 Tensile Test Results

Test piece No.	Maximum stress [MPa]	0.2% proof stress [MPa]	Elongation [%]
1	498	309	52.2
2	494	327	51.5
3	495	330	48.7
4	496	328	49.9
5	495	328	49.8
Standard value	480 or more	(175 or more)	40 or above

Table 2 Results of Young's Modulus Test by Resonance Method

Test piece	Temperature [°C]	Young's modulus [GPa]
Made by Nikon	25	184
Made by PBF method	25	168
Rolled material (rolling direction)	25	187
Rolled material (direction orthogonal to rolling)	25	194

Next, the results of the hardness test are presented in Table 3, in which the sample size is three, whereas the minimum, maximum and average values measured at multiple locations are also given. Without solution heat treatment, there are some points in the area near the base material, the starting point of modeling, where the hardness exceeds the standard value (HRBS90 or less). However, after the solution heat treatment, the standard values are satisfied at all measurement points.

Table 3 Hardness Test Results (Before and After Solution Heat Treatment)

HRBS	Before heat treatment			After heat treatment		
	No. 1	No. 2	No. 3	No. 1	No. 2	No. 3
Min	88.5	89.0	88.0	84.5	84.5	84.0
Max	94.5	93.5	94.5	88.0	88.0	88.0
Avg	91.8	91.6	91.7	86.2	85.9	85.6

Moreover, the inverse pole figure orientation map for crystal analysis by electron backscatter diffraction is demonstrated in Fig. 10.

For comparison, materials made by PBF and rolling methods were also analyzed. From the map, it can be seen that, while the crystal grains of the modeled object are as large as those of the rolled material, those of the PBF method are smaller. None of the crystals have orientation, and since the modeled object and the rolled material have less color unevenness, the intra-grain strain is considered to be small.

From the aforementioned results, it can be inferred that the mechanical characteristics of the modeled object are closer to the rolled materials than to the PBF method. This could be explained as follows: the LMD method forms a melt pool and sprays metal powder so that it completely melts and solidifies; unlike the PBF method where high-speed laser operation is used, here, because the processing head is physically driven, the rapid thermal change of the model is small.

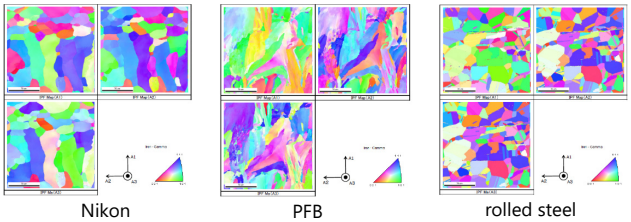

Fig. 10 Inverse pole figure orientation map.

10 Modeled Sample

A sample of modeling a heat exchanger with a lattice structure by Lasermeister 100A/101A is shown in Fig. 11. In

such lattice structure, a coolant flow path that maintains the overhang angle without support material, is provided inside, while the surface area is increased by modeling the structure to greatly enhance the heat exchange efficiency. This is a shape difficult to be achieved through conventional machining.

A repaired and finished sample is shown in Fig 12, in which cracks simulating pipe damages were made and the overlay was repaired by modeling.

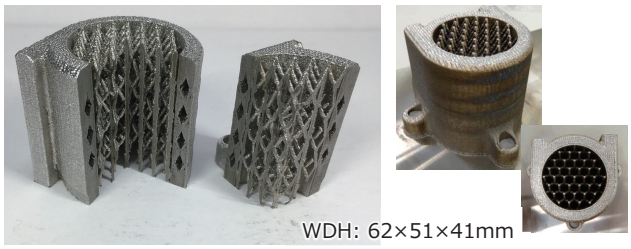

Fig. 11　Heat exchanger with a lattice structure.

The overlay welding restoration, which generally requires craftsmanship by skilled welders, can be easily performed by Lasermeister 100A/101A.

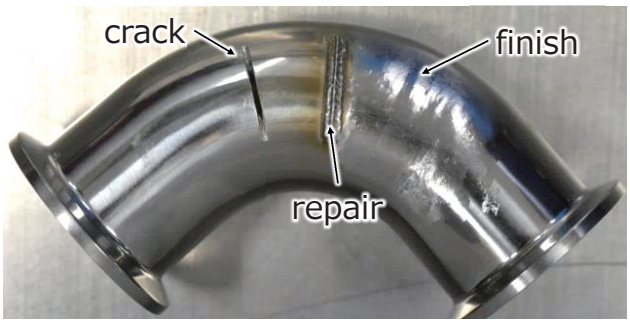

Fig. 12　Repair of damage in a pipe.

A sample is shown in Fig. 13, in which additional processing of a pipe of diameter 14 mm was performed on an existing flange using five-axes and then the surface was finished. Thus, bending points can be provided at any position within the modeling range, while designing and modeling at any angle is possible. Because this is a process of direct addition to the flange, unlike the PFB method, wire cutting of the model is not required, which is a great advantage. By contrast, in the conventional method, it is necessary to manually prepare a mold according to the bending process and angle, together with welding work.

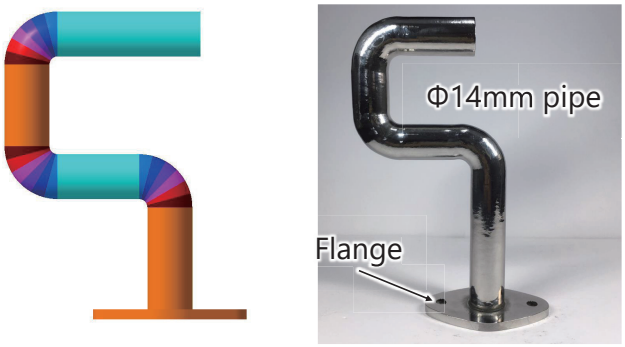

Fig. 13　Sample of pipe modeling with five-axes.

11 Summary

Lasermeister 100A/101A is a device developed to renew the conventional image of “large”, “expensive”, and “complex-operation” 3D metal printers with a goal to create a new market and industry for manufacturing. In addition to incorporating various uniquely developed items to improve modeling accuracy, which was a problem in the LMD method, we also offer easy operability to the user. Shapes that were difficult to process up to now, such as the samples introduced, can be realized with this device. In the future, we will continue to challenge new possibilities of material processing while adding and evolving functions that directly correspond to the pain points of users.

上野和樹
Kazuki UENO
次世代プロジェクト本部
第一開発部
1st Development Department
Next Generation Project Division

FPD 用高精度フォトマスクブランクスの開発

八神高史，小澤隆仁，宝田庸平，林　賢利，宮城茂彦，瀧　優介

Nikon's High-definition Photomask Blanks for Flat Panel Displays

Takashi YAGAMI, Takashi OZAWA, Yohei TAKARADA, Kento HAYASHI,
Shigehiko MIYAGI and Yusuke TAKI

フォトマスクブランクスは，微細な配線パターン等を転写するために，パターン形成用の遮光膜・位相シフト膜を石英ガラス製のフォトマスク基板の上に成膜した製品である．フォトマスクブランクスを用いてパターンを転写したガラスプレートは，フラットパネルディスプレイ（FPD）として TV やスマートフォンに使用されている．

FPD の大型化に伴い，FPD を露光するためのフォトマスクブランクスも大型化しており，最も大型の G10世代では 2 m 四方近くある．大型のフォトマスクブランクスにおいては，平面度の面内均一性，遮光膜・位相シフト膜の光学特性面内均一性という要素が大きな課題となる．なぜならば，フォトマスク基板のサイズが大きいので，均一に表面を研磨する技術，スパッタリング法によりパターン形成用膜を広範囲にわたり均一に成膜する技術，広いエリアを精度よく測定する技術が確立し難いためである．同時に，基板平面度の面内均一性・膜の面内均一性はパターンの転写精度に大きな影響を及ぼすため，FPD 露光装置側からの要求が厳しいためでもある．

ニコン製 FPD 用高精度フォトマスクブランクスは，非常に高い基板平面度，膜の光学特性面内均一性を有し，次世代の高精細ディスプレイの製造に不可欠な製品である．また，その測定値は，高い測定精度を誇るニコン製の測定装置により保証されている．

Photomask blanks consist of a photomask substrate and a binary film or a phase shift film on the surface to transfer the circuit pattern. High-volume panels with transferred circuit pattern are embedded into flat panel displays (FPDs).

The demand for larger-sized displays has been increasing, and, accordingly larger panels are required. Currently the largest photomask substrate size is approximately 2 m × 2 m (G10 Mask). Uniformities of flatness and optical characteristics are significant issues in realizing larger-sized photomask as attaining these uniformities over large areas is highly challenging. However, these uniformities require pattern-transfer accuracy; therefore, the demand for high-definition photomask blanks must be satisfied.

Nikon's high-definition photomask blanks exhibit high precision over G10 photomask area, such as the higher flatness uniformity, optical characteristics uniformity resulting from Nikon's high precision polishing, film deposition and measurement technologies.

In this report, we introduce these excellent properties of these photomask blanks for application in advances FPD Panels.

Key words FPD フォトマスクブランクス，フォトリソグラフィー，平面度測定，重ね合わせ精度，位相シフト膜
FPD photomask blanks, photolithography, flatness measurement, overlay, phase shift mask

1 Introduction

Liquid crystal and organic EL displays present images by controlling the emission color and brightness of each pixel. Although a thin-film transistor circuit is formed on the display to control the light emission, in FPD lithography, the pattern of this circuit is transferred from the original plate using light (Fig. 1). By repeating the transfer from original plates having different wiring patterns, a circuit having a three-dimensional wiring pattern can be eventually transferred. Displays are mass-produced by performing this transfer process on a large number of panels. The quartz glass, which forms the original plate, is called the photomask substrate, whereas the film (light-shielding / phase-shift) formed on its surface, and used for pattern formation that becomes the original plate, is called a photomask blank.

The size of the display is increasing year by year, while the size of the photomask original plate is also increasing correspondingly. The largest photomask, called the Generation 10.5 photomask (hereinafter called the G10 mask blank, and the one without a film formed on the surface is called the G10 substrate), has a size of approximately 2 m × 2 m.

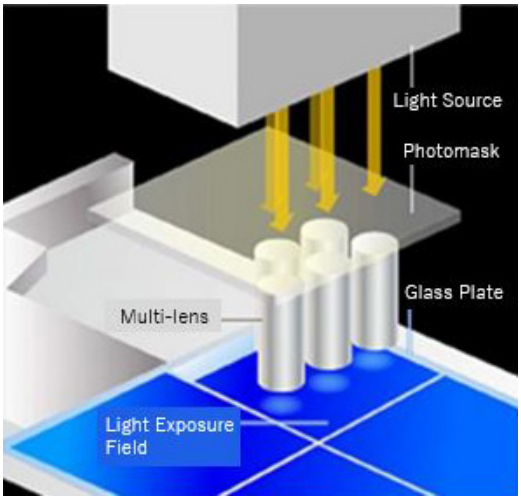

Fig. 1 State of light exposure in an FPD exposure device[1].

When forming a film for pattern formation on a G10 substrate, the film forming area is also close to 2 m × 2 m, making it an extremely large photomask blank. In this paper, we introduce photomask substrates with high flatness to improve the pattern transfer performance.

Moreover, there are variations in the film of the circuit pattern forming layer; it can be a light-shielding mask (binary film), whose purpose is to transfer the pattern by blocking the light exposure, or a phase-shift film, whose purpose is to make the light exposure semi-transparent and invert the phase to improve the contrast of the transferred pattern (Fig. 2). In this paper, we introduce the phase-shift film required for the mass production of high-definition displays.

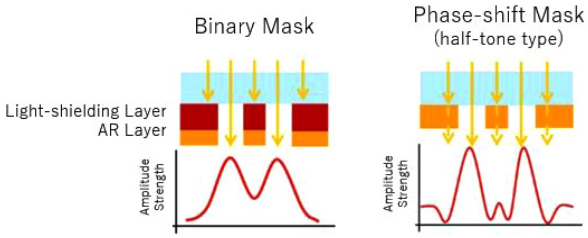

Fig. 2 Film structure of the pattern forming film.

2 Characteristics required for the FPD photomask blanks

The performance of the photomask blanks greatly influences the pattern transfer characteristics. For example, when setting a photomask on an FPD exposure device, deflection occurs, which must be corrected. However, because this correction is based on the premise that the photomask substrate is a perfect flat surface, if the flatness of the photomask substrate is insufficient, the correction deviates greatly. Further, if the in-plane uniformity optical property of the light-shielding film and phase-shift mask used in pattern formation is low, it will lead to dimensional deviation of the circuit when the pattern is transferred to the glass plate. Therefore, photomask blanks are required to have the aforementioned high in-plane uniformity, that is, they must have a high precision.

However, as mentioned earlier, because photomask blanks for FPDs have become comparatively large in the recent years, it is difficult to meet the aforementioned requirement. Therefore, it is necessary to have a polishing technology that can increase the flatness of a quartz glass surface with a maximum size of around 2 m × 2 m, a film-forming technology that can improve the in-plane uniformity optical property of light-shielding films, and phase-shift masks of size approximately 2 m × 2 m, as well as a measurement technology that can measure these physical property values repeatedly over a wide area with high accuracy.

3 Characteristics of the High-precision Photomask Blanks used in Nikon FPD

Nikon FPD photomask substrates have high in-plane flatness uniformity. In addition, the in-plane uniformity optical property of the photomask blank, on which the light-shielding film and phase-shift mask are formed, is high, even in maximum-sized G10 mask blanks. Hence, it is an important product in the manufacture of next-generation high-definition displays.

- **In-plane flatness uniformity**

The in-plane flatness of the G10 substrate is shown in Fig. 3. For all of the front, back and plate thickness variations (total thickness variation, TTV), an in-plane flatness uniformity of 3 μm or less has been achieved. Further, it can be seen that the flatness is extremely high compared to the normal specifications of 20 μm for the front and back surfaces, and 30 μm for the plate thickness. We have commercialized this photomask substrate with the specification called Super Flat Mask (SFM)-SS. Other standards are also available, which are shown in Table 1.

In order to obtain such high flatness even with G10 substrates, a polishing technology that can control the flatness of any part of the substrate is required, and Nikon has been refining its polishing technology by accumulating know-hows over the years.

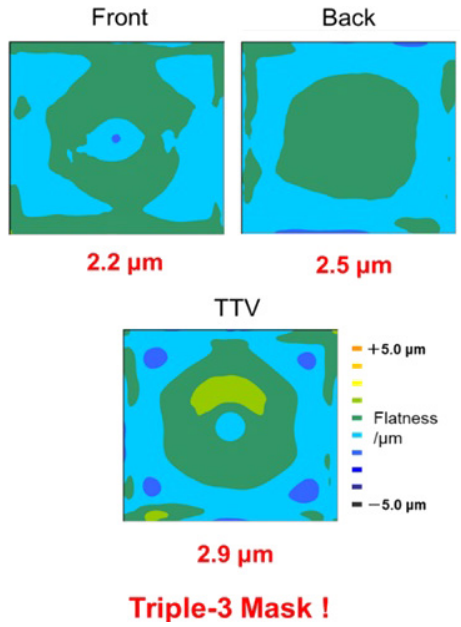

Fig. 3 In-plane flatness of G10 substrate.

Table 1 Flatness specifications of photomask substrates

Subjects	SFM-SS	SFM-S	SFM	Normal
Flatness of front surface	≦ 3 μm	≦ 5 μm	≦ 7 μm	≦ 20 μm
Flatness of back surface	≦ 3 μm	≦ 5 μm	≦ 10 μm	≦ 20 μm
TTV (Total Thickness Variation)	≦ 3 μm	≦ 5 μm	≦ 10 μm	≦ 30 μm

• Photomask substrate flatness and overlay accuracy

With the cooperation of a display manufacturer, we evaluated the flatness effect of the photomask substrate on the pattern overlay accuracy (overlay), during the low-temperature poly silicon (LTPS) TFT manufacturing process.

The schematic diagram of the evaluation procedure is given in Fig. 4. The photomask substrate, glass plate, and light exposure, are of the sixth generation. Considering the error influence, three glass plates were prepared. We compared the overlay accuracy among 14 patterns that are required to have high accuracy (between A-B, between B-C, and between B-D of the figure). The size of the photomask substrates used for comparison was 800 × 920 mm; the flatness levels were of two types, normal specification and SFM-S; the overlay accuracy was normal specification × normal specification; and the two sets, SFM-S × SFM-S, were used. The overlay accuracy was measured for 168 points (= 14 points * 3 rows * 4 scans) per glass plate, and a total of 504 points for 3 glass plates, while the variation 3 σ was obtained.

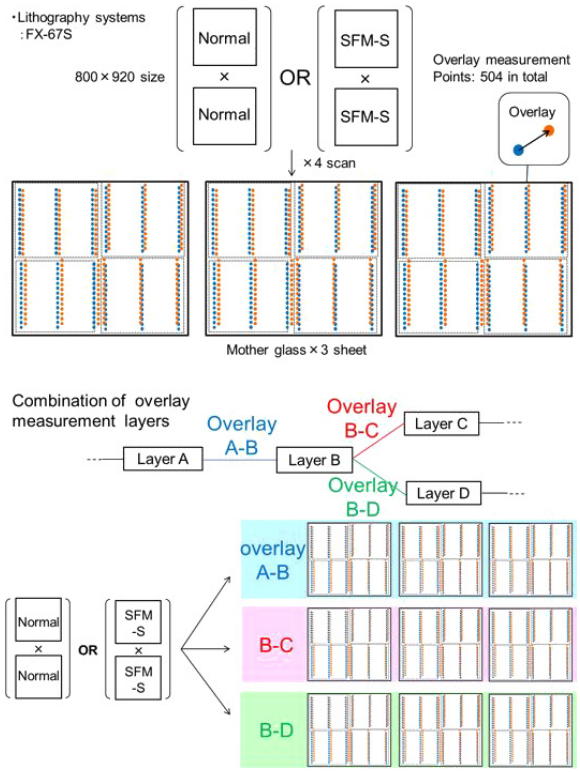

Fig. 4 Procedure for checking overlay accuracy based on the flatness of the photomask substrate.

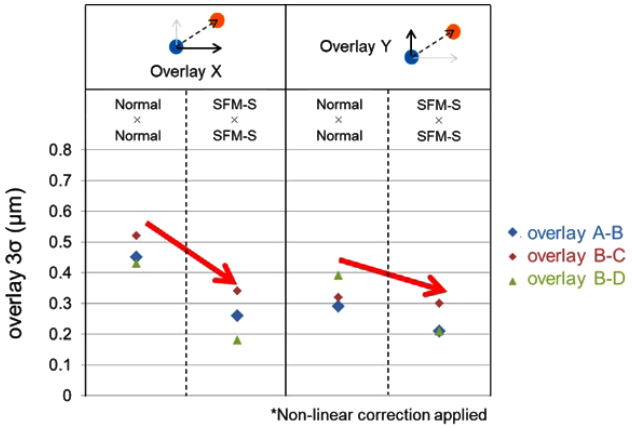

Fig. 5 Results of the overlay accuracy verification experiment.

From the results, it can be observed that the overlay accuracy improved when using SFM-S, compared to the photomask substrate with normal specifications (Fig. 5). In other words, using a photomask substrate with high flatness is suitable for the production of high-definition displays.

4 Measurement technology to support high-precision blanks

Even if a photomask substrate with high flatness is manufactured, its flatness cannot be guaranteed unless measured accurately. Further, even if a photomask blank with high in-

plane uniformity optical property is manufactured, if the optical properties cannot be measured accurately, the in-plane uniformity will be worse than it actually is due to the variations of the measuring equipment.

Thus, high-precision measurement technology is indispensable for the production of high-precision photomask blanks. In this paper, we introduce the Nikon flatness measuring instrument ALGS (Analyzer for Large size Glass Surface). With ALGS, the flatness can be accurately measured at multiple points even on a G10 substrate, while the in-plane flatness uniformity can be precisely adjusted.

• **Photomask substrate flatness measuring instrument ALGS**

The Nikon flatness measuring instrument ALGS is a device that can measure the flatness of the photomask substrate with high accuracy. Sizes up to G10 substrate can be mounted.

The high accuracy is due to the adoption of a highly rigid frame that suppresses the deformation and vibration of the entire device, and a substrate holding system that suppresses the distortion of the substrate that occurs when the measuring instrument is set in.

Moreover, since it is a device manufactured in-house, detailed analysis of the flatness measurement results is carried out, and the device is being remodeled to expand and improve its precision year by year.

ALGS also verifies the deviation accuracy by performing periodic measurements while changing the substrate posture, whose results are demonstrated in Fig. 6.

From Fig. 6, it can be seen that the measurement deviation is suppressed to 0.4 μm, which is sufficiently accurate to guarantee the measurement value of SFM-SS. Thus, the quality of the Nikon photomask blanks is assured by high measurement technology.

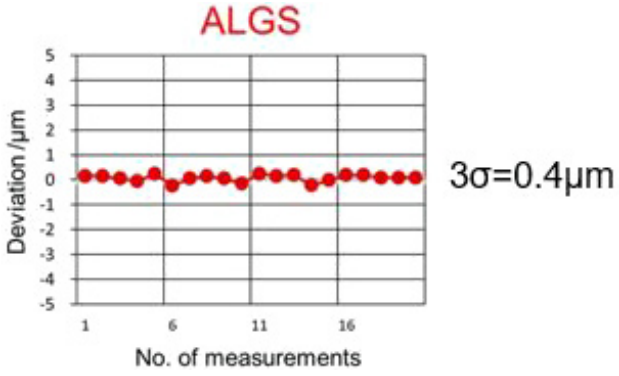

Fig. 6 Repeated flatness measurement reproducibility of ALGS.

• **In-plane uniformity optical property**

In a light-shielding or a phase-shift film formed on a photomask substrate, low uniformity optical property leads to deterioration of the imaging characteristics. Hence, it is required that the light-shielding film has high reflectance, whereas the phase-shift film has high transmittance and in-plane uniformity of the film. In this paper, we focus on the phase-shift film.

The in-plane uniformities of the transmittance and phase shifting angle of the G10 Cr phase-shift mask blank are given in Fig. 7. The general specifications of high-definition phase shift mask blanks are a transmittance in-plane uniformity of 0.7%, and a phase shifting angle in-plane uniformity of 10° . From the figure, it can be deduced that the specifications for high-definition masks have been achieved, regardless of whether it is a G10 mask blank or not.

Such high in-plane uniformity optical property is obtained by feedback control based on the local changes in the film-forming conditions. This is Nikon's unique method that improves the in-plane uniformity by measuring the in-plane uniformity of the immediately preceding batch and automatically adjusting the film-forming conditions at the locations where deviation from the target value is large.

• **Cross-sectional shape of the phase-shift film**

The phase-shift film requires not only the in-plane uniformity optical property, but also a nearly vertical cross-sectional shape after pattern formation. If the cross-sectional shape is inclined, the amount of phase shifting angle in the inclined portion greatly deviates from 180°, which leads to the reduction of contrast improvement effect, as the amplitude cancellation of the exposed light at the edge of the pattern is weakened.

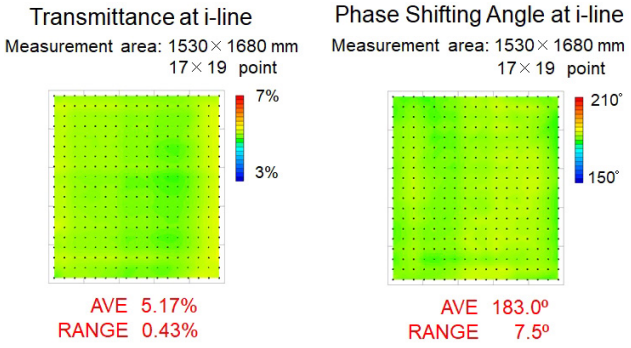

Fig. 7 In-plane uniformities of the transmittance and phase shifting angle in G10 Cr phase-shift mask blanks.

The cross-sectional shape of the Cr phase-shift mask after pattern formation is shown in Fig. 8. It can be seen that as the time of immersion of the Cr film in the etching solution

increases, the cross-sectional angle of the film becomes almost vertical. Hence, even in terms of cross-sectional shape, Nikon's phase-shift mask is suitable for the mass production of high-definition displays.

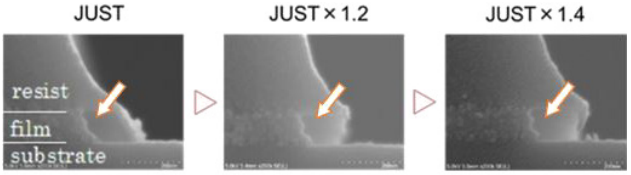

* JUST: Time taken for the film to be dissolved completely, as seen visually

Fig. 8 Cross-sectional SEM image of the Cr phase-shift film after pattern formation.

5 Summary

Nikon photomask blanks have high in-plane uniformities of the substrate flatness, with optical properties guaranteed by high measurement technology, which are preserved even in the G10 mask blanks. These are the high-precision photomask blanks suitable for mass production of next-generation high-definition displays.

References

1) Nikon Corporation FPD Lithography Business Unit. "Accommodating larger glass plates with the multi-lens system". https://www.nikon.com/products/fpd/technology/story03.htm

八神高史
Takashi YAGAMI
ガラス事業室
製造部
Production Department
Glass Business Unit

林　賢利
Kento HAYASHI
ガラス事業室
製造部
Production Department
Glass Business Unit

小澤隆仁
Takashi OZAWA
ガラス事業室
製造部
Production Department
Glass Business Unit

宮城茂彦
Shigehiko MIYAGI
ガラス事業室
製造部
Production Department
Glass Business Unit

宝田庸平
Yohei TAKARADA
ガラス事業室
製造部
Production Department
Glass Business Unit

瀧　優介
Yusuke TAKI
ガラス事業室
製造部
Production Department
Glass Business Unit

研究開発論文

Research and Development Reports

微細構造特性評価のための暗視野落射照明系搭載ミューラー行列撮像偏光計顕微鏡システム開発

齋藤直洋，佐藤憲司，藤井　透，Heather Lynn Durko，Goldie Lynne Goldstein，
Alton Hugh Phillips，Photini Faith Rice，Joceline Dominguez-Cooks，
Gabrielle Vanessa Hutchens，Harrison Taylor Thurgood，Jennifer Kehlet Barton

Mueller matrix imaging polarimeter microscope system development incorporating dark-field episcopic illumination system for microstructure characterization

Naooki SAITO, Kenji SATO, Toru FUJII, Heather Lynn DURKO, Goldie Lynne GOLDSTEIN,
Alton Hugh PHILLIPS, Photini Faith RICE, Joceline DOMINGUEZ-COOKS,
Gabrielle Vanessa HUTCHENS, Harrison Taylor THURGOOD and Jennifer Kehlet BARTON

偏光は，光と物質の相互作用を表す特徴量の一つである．偏光状態は，光学系が解像できないような微細構造でも反応して変化する．偏光イメージングは，多様な分野で容易に見ることができない情報を可視化するツールとなりつつある．我々は，物質と光の相互作用を記述できる16次元の情報をもつミューラー行列を計測できる顕微鏡の試作機を開発した．生体組織からの散乱光の偏光計測を行うことで，見た目には分からない組織構造の違いを識別することが可能である．このシステムは，落射暗視野偏光照明系とフルストークス撮像偏光計の構成されており，組織表面付近の構造により変化した散乱光の偏光状態を効率的に計測することができる．アリゾナ大学での長期的な実験検証を通じて，我々のシステムは高い安定性と共に信頼性を実証し，組織計測の結果は先行研究例と一致した．

Polarized light is one of the characteristic quantities representing the interaction between light and matter. The state of polarization changes in response to fine structures that cannot be resolved by an optical imaging system. Polarimetric imaging is becoming a tool in a variety of fields to visualize information that cannot otherwise be easily seen. We have developed a prototype microscope that can measure the 4×4 Mueller matrix that describes the interaction between matter and light. By performing the polarimetric measurement of the scattered light from the biological tissue, it is possible to discriminate a difference in the tissue structure that cannot be detected visually. This system, which comprises an epi-illumination dark-field polarized illumination system and a full-Stokes imaging polarimeter, can efficiently measure the polarization state of light scattered by the structure near the tissue surface. Through long-term experimental validation at the University of Arizona, our system has demonstrated reliability with high stability, and tissue measurement results are consistent with those reported in the literature.

Key words 偏光計測，偏光撮像計，ミューラー行列，多波長撮像，散乱撮像
polarimetry, imaging polarimeter, Mueller matrix, multispectral imaging, scattering imaging

1 Introduction

Polarimetric imaging enables us to detect information that is not visually apparent. It is well known that the state of polarization (SOP) of light can change as it transmits through, reflects from, or scatters within an object due to the object's optical properties, surface features, and microscopic structures[1]. Therefore, techniques to visualize polarization information have been developed for many fields.

Combining microscopy and polarimetry can create a powerful tool for optical measurement. Microscopes are high-precision and highly reliable optical measurement devices having both an illumination system and an observation system[2], and can be employed for industrial as well as biomedical applications.

Many attempts to utilize polarimetry in the medical field have been studied[1)3)4)]. Most commonly, it is employed to detect cancerous tissues for early cancer diagnosis. With the resolution of standard cancer detection methods such as CT, MRI, and PET, it is not easy to visualize cancerous regions

smaller than 1 mm in size. Discriminating and detecting microscopic cancer tissue can lead to early cancer detection and contribute to improved five-year survival rate.

Nikon Corporation has developed a microscope system to identify differences in the microstructure of biological tissue using polarimetry to detect early cancer[5]. Proper control of the SOP of the illumination light on the sample makes it possible to measure a Mueller matrix that describes the complex interaction between the sample and polarized light. The realization of the Mueller matrix measurement in a microscope system can provide a quantitative polarization measurement environment that cannot be achieved with a conventional polarization microscope. The system performance was verified and a tissue study was performed in collaboration with the University of Arizona.

2 Principle and Methods

(1) System concept

The configuration of the Mueller matrix polarimeter can be conceptualized as shown in Fig. 1[6]. For the Mueller matrix measurement, the optical system consists of two essential parts: a polarization state generator (PSG) that illuminates the sample on the sample stage with known polarization states, and a polarization state analyzer (PSA) that measures the SOP of the scattered light from the sample as Stokes parameters. The Mueller matrix of the sample can be estimated using the Stokes parameter information obtained under a plurality of polarized illuminations.

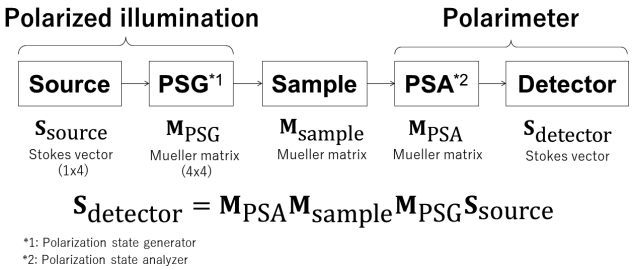

Fig. 1 The schematic of Mueller matrix polarimeter

Image contrast of the microstructure near the surface of the tissue sample can be enhanced by using dark-field epi-illumination, which prevents specular reflections from contributing to the polarimetric measurements. Epi-illumination can also be used to measure the surface of thick tissue samples, which accommodates a variety of sample forms without the need for sample slide preparation.

Multispectral measurements can take advantage of the difference in tissue light absorption. The light absorption coefficient of hemoglobin contained in biological tissue varies across the visible spectrum. At shorter wavelengths, the appearance of the tissue surface and the presence of blood can be revealed. At longer wavelengths, we can image deeper into the tissue. Spectral imaging can also provide information that is relevant to tissue identification tasks.

The imaging polarimeter incorporated in the observation path collects the full Stokes measurement in a single image. In the conventional method, the Stokes vector is measured by mechanically or electrically modulating the polarization of the measured light and acquiring a plurality of images. Fig. 2 shows the imaging polarimeter using the modified Savart plates (MSPs) in this optical system[7][8].

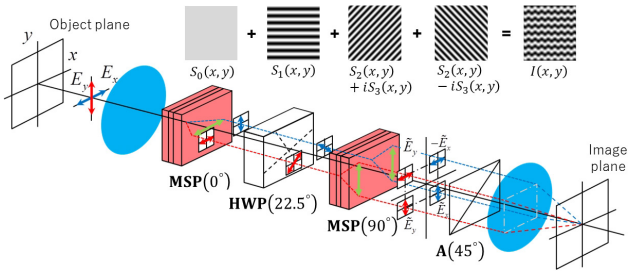

Fig. 2 Full-Stokes Imaging Polarimeter

The imaging polarimeter module generates polarization-dependent interference carrier fringes, so that all Stokes parameters can be encoded into one image. With this approach, since there are no mechanical moving parts or electrical modulation, stable and high-speed Stokes measurements are achieved.

(2) Mueller matrix imaging polarimeter microscope

We prototyped an optical system that combines a dark-field epi-illumination polarization generator with a polarizing microscope and a full-Stokes polarimeter. The system was constructed using a modified Nikon ECLIPSE LV100N POL polarizing microscope.

The PSG is incorporated as part of an epi-illumination system in which the outer NA of the objective lens pupil are used to realize a dark-field epi-illumination system. An incoherent illumination light source (SPECTRA X Light Engine, Lumencor) connects to the epi-illumination path with an optical fiber. The light source has can select between five bands with center wavelengths at 405 nm, 442 nm, 473 nm, 543 nm, and 632 nm. Interference filters constrain each band to 3 nm widths.

In the epi-illumination system, an arbitrary polarization is controlled by a combination of one polarizer and one quarter-wave plate. Each polarizing element is mounted on a rotary stage (K10CR1A2/M, Thorlabs, Inc.) to set an arbi-

trary azimuthal angle. Achromatic quarter-wave plates (APSAW-5, Astropribor) are employed to provide stable performance within the operating wavelength range.

The position of the light source fiber corresponds to the illumination path position in the pupil of the objective lens. In practice, the position of the fiber end is optimized to couple into the outer NA of the objective lens while minimizing stray light in the PSG optics. Fig. 3 shows the microscope and a diagram of the optical path.

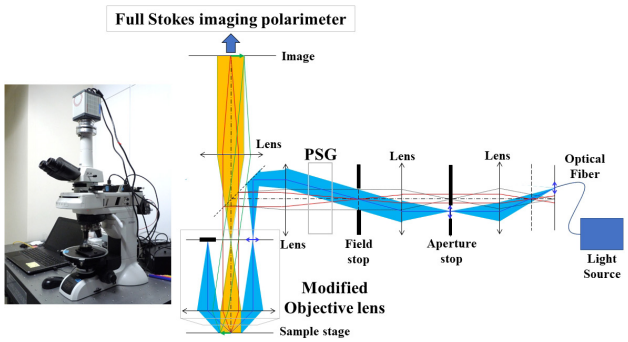

Fig. 3 Mueller matrix polarimeter microscope (left), and dark-field epi-illumination and observation optical paths (right)

Dark-field illumination is achieved by passing light from the illumination system through an aperture defined by a mask at the objective lens pupil. The specular reflected light on the sample surface is blocked by the pupil mask. Only polarized light scattered by the fine structure on the sample surface can enter the observation optical path through the central NA of the objective pupil.

The modified objective lens enables both dark-field epi-illumination and polarimetry of scattered light from the sample. The center NA of the pupil of the objective lens and the polarimeter installed on the camera adapter play the role of PSA. We modified a Nikon brightfield objective lens (Nikon CFI TU Plan Fluor EPI 5×, 10×) with minimal polarization distortion. The performance parameters after modification are as shown in Table 1.

The imaging polarimeter module uses modified Savart plates to enable snapshot measurements of Stokes parameters from polarized light that scatters from the sample. Two MSPs (Kogakugiken Corp.) installed in the camera adapter realize the separation of polarization components and the spatial shear with minimal crosstalk. A scientific CMOS camera (2048×2048-pixel, ORCA Flash 4.0, Hamamatsu Photonics K. K.) is positioned at the image plane to detect polarization-dependent interference fringes with high sensitivity and low noise. The spatial frequency of the interference fringes is set by the wavelength-dependent shear in the Savart plates, which determines the spatial resolution of the polarization measurement. The spatial resolutions are provided in Table 1.

Table 1 System specifications

Parameter	Specification	
Illumination		
Wavelength	405, 442, 473, 543, 633 nm (limited by interference filter; FWHM < 3 nm)	
State of polarization	Automatically switched by software	
Imaging	5 × objective	10 × objective
Effective magnification	3 ×	6 ×
Field of view (mm)	3.67	1.83
Working distance (mm)	23.5	17.5
Imaging NA (Max.)	0.075	0.150
Illumination NA (Max.)	0.150	0.300
Polarimeter	5× objective	10× objective
Spatial resolution	9.8 μm (at 442 nm) 10.6 μm (at 543 nm) 14.5 μm (at 632 nm)	4.9 μm (at 442 nm) 5.3 μm (at 543 nm) 7.3 μm (at 632 nm)
Sensor	2048 × 2048 pixels, 13.312 × 13.312 mm	

Full Mueller matrix measurements can be automatically obtained by this system. The custom software and external PC control the wavelength and SOP of the illumination light and automatically perform a series of Stokes parameter measurements required for Mueller matrix calculations. A similarly automated post-imaging process computes Mueller matrix maps of the imaged sample from the measured images at each measured wavelength.

Polarization errors caused by the optical system have been characterized through calibration and are removed from the sample measurements.

3 Stability enhancement

Because the MSP-based polarimeter used in this system encodes the Stokes parameters into the polarization-dependent carrier fringes, to determine the Stokes parameters from each measured image, the phase components of the carrier fringes are extracted relative to a reference measurement of a known SOP that is performed in advance of the sample measurement. If the polarimeter imaging environment does not change, the carrier phase components of the spatial carrier fringes remain constant. However, thermal variations in the imaging environment can change the carrier phase components between the reference measurement and the sample measurement, the demodulated information includes an error component corresponding to the mismatch in carrier phases.

We developed a model for the variation of spatial carrier fringes caused by temperature disturbances and developed a method to reduce the errors. The amount of shear generated in the birefringent crystal plates in the MSP is temperature-dependent. When the temperature changes, so does the carrier phase determined by the shear amount of the MSP. If a temperature disturbance occurs between the reference measurement and the sample measurement, the carrier phase component cannot be properly removed. Factors that cause a temperature disturbance include temperature changes in the room where the microscope is installed, and exhaust heat from the scientific CMOS camera. We identified the fringe fluctuation caused by the camera exhaust and removed the effect with post-processing compensation.

Through experiments and data analysis, we analyzed influence of each potential source or error by extracting the fringe variation error measured by the microscope system and performing quantitative analysis. From the analysis results, it was found that the errors caused by the vibrations caused by the operation and refocusing of the stage and the errors caused by the exhaust heat of the cooling camera were the dominant factors. We reduced the Mueller matrix element error caused by the temperature-dependent phase shift of the carrier fringes, improving the measurement stability. Table 2 compares the variation (3σ) of the average value across the field of view of the Mueller matrix error before and after the fluctuation compensation for each error factor. Regarding the error due to thermal fluctuation, the post-processing reduced the Mueller matrix element 3σ error from 0.046 to 0.021. Furthermore, by incorporating a function to monitor the fringe position, the error is expected to be suppressed to 0.010 or less.

Table 2 Comparison of Mueller matrix error of the system between before and after stability compensation

Error factors	Mueller matrix error (3σ)	
	Before compensation	After compensation
Repeatability + Resetability of automated contol	0.002	0.002
Temperature fluctuation	0.042	0.007
Resetability of objective revolver	< 0.001	< 0.001
Resetability of rotational stage	0.018	0.019
Resetability of standard element	0.004	0.004
Mueller matrix error of whole system	0.046	0.021

4 Results

We measured Mueller matrices of some biological samples using the prototype system.

Fig. 4 shows an example of measurement of porcine liver as a biological tissue sample.

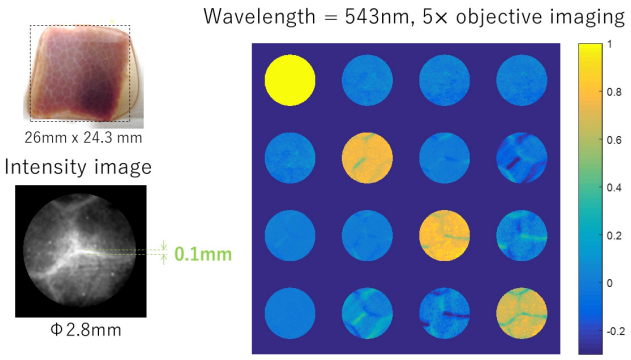

Fig. 4 The photo of porcine liver (upper left), the m_{00} microscope image at 543 nm (lower left), and the m_{00}-normalized measured Mueller matrix map

A color map of the Mueller matrix elements is shown. The Mueller matrix is normalized by the m_{00} intensity so that the polarization characteristics are displayed in an easy-to-understand manner. Porcine liver comprises many hepatic lobules surrounded by connective tissue. The connective tissue is known to have birefringent properties. In the m_{00} image, the connective tissue appears white, but in the Mueller matrix visualization, the same regions are represented in various colors that relate to the microscopic orientation of the birefringent tissue.

The polarization characteristics differ depending on the alignment direction of the connecting tissue, and the values of the Mueller matrix differ accordingly. This result indicates that the measurement and discrimination of the polarization characteristics of the submicron-sized tissue structure can be acquired with a Mueller matrix measurement.

We investigated the performance of this polarimeter microscope system by using it for cancer tissue imaging studies in collaboration with the research group led by Professor Jennifer Barton at the University of Arizona (Tucson, AZ USA).

Samples were obtained from discarded surgical resections of human colon tissue. The samples are cut from the discarded tissue immediately after the operation. Sample sections were obtained from visibly diseased and healthy tissue regions. Each sample is examined for the condition of the cancer tissue in pathological diagnosis after microscopic observation.

Fig. 5 shows an example of Mueller matrix measurements

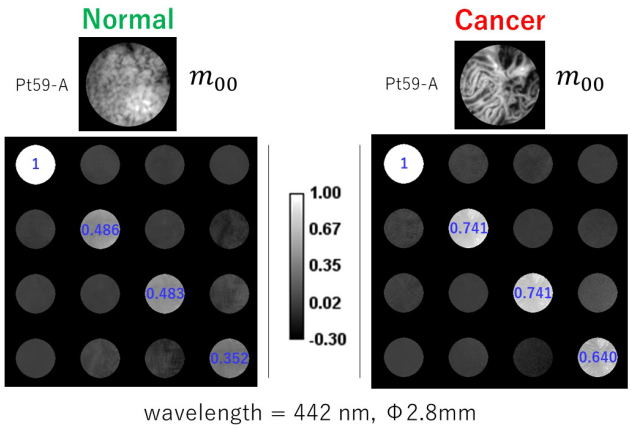

Fig. 5 m_{00}-normalized Mueller matrix maps of normal (left) and cancerous (right) human colon tissue

of normal and cancerous human colon tissue obtained from one patient and illuminated with 442 nm light. The average value across the field of view of the diagonal elements of the Mueller matrix is shown in blue. The intensity image shows the morphology of the samples, which are characteristic of each type of tissue. For both types of tissue, the diagonal components are dominant. However, cancerous tissue tends to have larger diagonal element values.

We compared the diagonal values using data from multiple patients. Fig. 6 shows the distribution of the Mueller matrix measurement results for multiple human colon tissues.

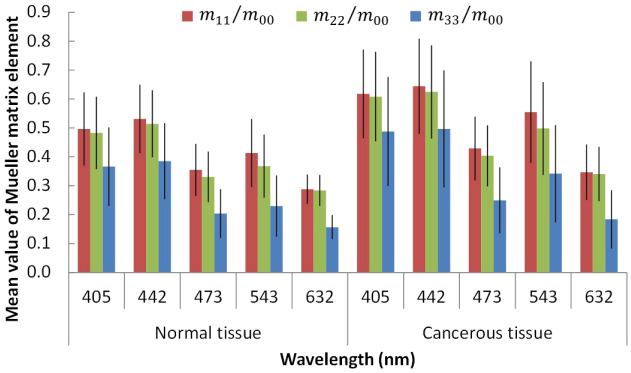

Fig. 6 The statistics of the diagonal element values across the field of view of the Mueller matrix for 18 patients, mean value and standard deviation

We calculated the statistics of the mean value across the field of view of the Mueller matrix element values of multiple patients. In Fig. 6, each color is the average of each diagonal element value at the five wavelengths. Black bars indicate the standard deviation among 18 patients.

From these results, although the variation between patients is large, the diagonal element values of the Mueller matrix tend to be larger in cancer tissues than in normal tissues. This result is consistent with previous studies reported by Novikova[9]. The colon-tissue Mueller matrices obtained with this microscope have also been utilized for additional related studies[10].

5 Conclusion

We developed a novel Mueller matrix polarimeter microscope system that consists of a dark field epi-illumination system and a full-Stokes imaging polarimeter. The dark-field observation provided by the combination of the epi-illumination system and the modified objective lens performs polarization measurements of the light scattered from thick biological samples. The software automatically controls the illumination wavelength and SOP, and measurements acquired from a set of incident SOPs provide sufficient information to calculate the Mueller matrix of a sample at several wavelengths. The polarization error of the optical system in the system is minimized with calibration, and errors from thermal fluctuations can be stably reduced.

We have shown the effectiveness of the microscope system in biological tissue experiments. The Mueller matrix measurements of porcine liver tissue indicate an increased contrast between microscopic tissue structures when measured by the difference in polarization state. The statistical difference between the Mueller matrices of cancer and normal tissues in human colon replicated the results of previous studies and proved the validity of the system. Through this research, we showed the possibility of a new medical imaging technology using polarized light.

References

1) V. V. Tuchin, L. Wang and D. A. Zimnyakov: *Optical Polarization in Biomedical Applications* (Springer Science & Business Media, 2006).
2) S. Schwartz, S. Ross, K. Spring, T. Fellers, M. Parry-Hill, D. Murphy, J. Lippincott-Schwartz, G. Patterson, D. Piston and M. Davidson: *Nikon MicroscopyU*, https://microscopyu.com/ (2005).
3) Z. Chen, Y. Yao, Y. Zhu and H. Ma: "A colinear backscattering Mueller matrix microscope for reflection Muller matrix imaging", *SPIE Proceedings*, 104890M (2018).
4) T. Novikova, J. Rehbinder, S. Deby, H. Haddad, J. Vizet, A. Pierangelo, P. Validire, A. Benali, B. Gayet, B. Teig, A. Nazac, B. Drévillon, F. Moreau and A. De Martino: "Multispectral Mueller Matrix Imaging Polarimetry for Studies of Human Tissues", *OSA Technical Digest* (online) (Optical Society of America, 2016), paper TTh3B.2. (doi: 10.1364/

TRANSLATIONAL.2016.TTh3B.2)
5) N. Saito, K. Sato, T. Fujii, H. L. Durko, G. L. Goldstein, A. H. Phillips, J. Dominguez-Cooks, G. V. Hutchens, H. T. Thurgood, P. F. Rice and J. K. Barton: "Multispectral Mueller matrix imaging dark-field microscope for biological sample observation", *SPIE Proceedings*, 108901A (2019).
6) D. H. Goldstein: *Polarized Light*, 3rd ed. (CRC press, 2010).
7) K. Oka and N. Saito: "Snapshot complete imaging polarimeter using Savart plates", *SPIE Proceedings*, 629508 (2006).
8) N. Saito, S. Odate, K. Otaki, M. Kubota, R. Kitahara and K. Oka: "Wide field snapshot imaging polarimeter using modified Savart plates", *SPIE Proceedings*, 88730M (2013).
9) T. Novikova, A. Pierangelo, S. Manhas, A. Benali, P. Validire, B. Gayet and A. De Martino: "The origins of polarimetric image contrast between healthy and cancerous human colon tissue", *Applied Physics Letters*, **102** (2013) 241103.
10) T. Fujii, Y. Yamasaki, N. Saito, M. Sawada, R. Narita, T. Saito, D. L. Heather, P. F. Rice, G. V. Hutchens, J. Dominguez-Cooks, H. T. Thurgood, S. Chandrae, V. Nfonsam and J. K. Barton: "Polarization characteristics of dark-field microscopic polarimetric images of human colon tissue", *SPIE Proceedings*, 108902J (2019).

齋藤直洋
Naooki SAITO
研究開発本部
光技術研究所
Optical Research Laboratory
Research and Development Division

佐藤憲司
Kenji SATO
FPD 装置事業部 開発統括部
第二開発部
2nd Development Department
Development Sector
FPD Lithography Business Unit

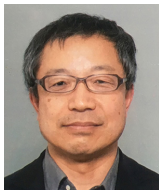

藤井　透
Toru FUJII
研究開発本部
光技術研究所
Optical Research Laboratory
Research and Development Division

Heather Lynn DURKO
Nikon Research Corporation of America

Goldie Lynne GOLDSTEIN
Nikon Research Corporation of America

Alton Hugh PHILLIPS
Nikon Research Corporation of America

Photini Faith RICE
The University of Arizona

Joceline DOMINGUEZ-COOKS
The University of Arizona

Gabrielle Vanessa HUTCHENS
The University of Arizona

Harrison Taylor THURGOOD
The University of Arizona

Jennifer Kehlet BARTON
The University of Arizona

アポディゼーション位相差顕微鏡法と生物医学応用

大瀧達朗

Apodized Phase Contrast Microscopy and Its Biomedical Applications

Tatsuro OTAKI

人間の目や普通のカメラは物体の像を明暗のコントラストとして捉える．色は光の波長に応じた明暗を表現している．顕微鏡は小さな物体を観察する重要な器械で，細胞や微生物の発見は今日の医学や生物学の基礎となった．無色透明な細胞などは染色して観察するが，細胞毒性の問題がある．位相差法は無色透明な位相物体を透過した直接光と回折光に光学系で位相差を与え像面で干渉させて像にコントラストを与える．無染色で観察する優れた方法だが従来法では像に現れるハロという現象で微細部分がつぶれる問題があった．この問題の解決のためアポディゼーション位相差顕微鏡法を発案し開発した．細胞などの位相物体で光波に生じる回折角と位相差に関係があることを見出し，大きな物体で生じるハロを減らし微小物体を高コントラストで観察可能にした．最近我々はコントラストの異なる検出力の高い ABH（apodized bright contrast high）法を開発した．応用として肺疾患の原因のアスベスト繊維の検出に用いた．また生細胞の分析に細胞内小器官の屈折率分散が異なることに着目し，波長選択による像コントラストの違いからミトコンドリアと油滴の区別を示した．生殖補助医療分野では，初期胚のタイムラプス撮像で微細な顆粒状構造や繊維状構造を確認した．無染色観察は臨床分野で重要であり，アポディゼーション位相差顕微鏡法は広く応用が可能であろう．その原理と応用について報告する．

Human eyes and general imaging devices detect images as the contrast in brightness or intensity. A colour appears as a contrast depending on differences in wavelengths of light. Microscopes are important instruments for observing small objects, and have contributed to the progress in bacteriology, biology and medical science. Cells are typically colourless and transparent phase objects. Conventional phase-contrast microscopes are suitable for observing phase objects, but large phase-object images lose detailed structures because of halo artifacts. Other than for thin specimens, they are also often used for finding or checking cultured cells. Apodized phase-contrast microscopy was developed to reduce the halos when imaging fine anatomical structures. A relationship exists between the angle of diffraction and phase difference of objects in cells. Apodized phase-contrast microscopy weakens the diffracted light produced by large objects to lower their relative image contrast and increases the contrast of small objects. An apodized phase plate provides an optical filtering. In this study, a bright contrast method for apodized phase-contrast microscopy, called apodized bright contrast high (ABH), was developed. Various biomedical applications, such as analysis of asbestos, cellular organelles and early embryos, were experimented. Apodized phase-contrast microscopy provides images of fine structures. Its principles and biomedical applications are described in this paper.

Key words アポディゼーション位相差顕微鏡法，コントラスト，分散，屈折率，細胞内小器官
apodized phase contrast microscopy, apodization, contrast, dispersion, refractive index, organelle

1 Introduction

Human eyes and general imaging devices detect images as the contrast in brightness or intensity. Colours are expressed as contrasts depending on differences of wavelengths of light. An optical microscope is a useful instrument for observing small objects. Robert Hooke discovered the cell using early microscopes with eyepieces, and he published *Micrographia* in 1665. Robert Koch identified microorganisms, such as various bacteria, in the late 19th century, and supported his postulates describing relations between a disease and a microorganism. Progress in bacteriology, biology and medical science has been achieved as a result of many microscopic observations. Modern optical microscopes incorporate several important optical principles.

Microscopes and optical principles

Ernst Abbe introduced "numerical aperture", $n \sin \alpha$, and defined the limit of the delineating power d of the microscope (1881)[1]. It is expressed by

$$d = \lambda / (2n \sin \alpha),$$

where λ is the wavelength of light, n is the refractive index of the medium and α is the semi-angle of the maximum incident ray to the objective. This limit of the delineating power is known as under coherent illumination. The aperture radius, r, of the objective is calculated by $r = f n \sin \alpha$, where f is the focal length of the objective.

Abbe set up an arrangement of illumination from a point light source (coherent illumination) to the diffraction grating, and it was used as the starting point of imaging theory. For microscopic imaging, he used an arrangement, which illuminates equidistant parallel gratings with point light sources. When a plane wave generated from a point light source illuminates the diffraction grating with an interval d, the wave is diffracted in a direction u given by $\sin \alpha = m \lambda / d$, where m is an order of 0, ± 1, ± 2, ... This type of image is caused by Fraunhofer diffraction. In a lens with a focal length f, a point image is formed at a distance of $f \sin \alpha$ from the optical axis according to the angle α. These diffraction images represent spectra in the frequency domain of the diffraction grating. An object having an arbitrary amplitude distribution and spectrum related by the Fourier transform. Further, the light beam advances and forms an image on the optical conjugate plane of the object. This spectrum and image are also related through a Fourier transform. Whether the diffraction grating is an amplitude grating or a phase grating, a conjugate image is formed. This idea was applied to the imaging theory of the microscope.

Lord Rayleigh proposed the resolution limit of two optically independent points through an optical system (1896, 1903)[2][3]. He defined a criterion when the distance between two neighbouring images formed through an optical system becomes the distance to the first dark circle of the Airy pattern or radius of the Airy disc. When a plane wave illuminates a pinhole object, the wave is diffracted and imaged through an objective (convex lens). The image forms an Airy pattern on the image plane. The lens shall be ideal and it produces no aberration. Then the wavefront forms spherical waves to the image.

The Rayleigh criterion at the diffraction limit having a circular aperture is expressed by

$$d = 0.61 \lambda / (n \sin \alpha).$$

This shows that two neighbours cannot be clearly distinguished if the distance between them is less than roughly half wavelength of light. It is important to note that this resolution holds for human eyes when recognizing sufficiently bright point images. In many cases, single points may still be visible.

August Köhler developed an illumination method in 1893[4], which is called Köhler illumination. The illumination requires that the field is uniformly bright. The Köhler illumination system consists of, from a light source to the object plane, a collector lens, a field stop, an aperture stop, and a condenser. The light source is focused by the collector lens on the front focal plane of the condenser (which has the aperture stop) as an air image of the light source. Then, all diverging light through the aperture stop of the condenser uniformly illuminates the object plane if the light source does not have uniform distribution. The field stop and object plane (field) are in optically conjugate planes. In addition, the aperture stop and the exit pupil of the objective lens are in optically conjugate planes. They control the illumination field and the illuminating angles to the object plane, respectively. Most microscope illumination systems are based on Köhler illumination. Further, the field is conjugate to the image plane and projected on the retina by the eyepiece, and the aperture stop is conjugate to the objective back focal plane.

Microscopic observation of phase objects

Microscopic observations of unstained living cells are important for biomedical applications. Cells are typically phase objects. Many microscope systems are used for observing phase objects, with phase-contrast microscopy by Zernike (1935, 1953)[5][6], differential interference contrast (DIC) microscopy by Smith (1950)[7], and by Nomarski (1953)[8], and modulation contrast microscopy by Hoffman and Gross (1975)[9], which are mostly commercialized for observing unstained cells. Differential interference contrast microscopy uses the polarization and interference of light waves. Modulation contrast microscopy uses a kind of oblique illumination, which shades the image according to changes in the refractive index. It is suitable for observing large structures, and is widely used in fertility treatment such as in vitro fertilization (IVF). Many other methods have been proposed for observing phase objects, such as dark field illumination and optical staining method.

2 Phase-contrast microscopy

Incident light wave, $\varnothing 0 = \sin \omega t$, transmits through a phase object such as a colourless transparent cell. The transmitted light has a phase difference δ due to a difference in refractive index. Then the light transmitted is described as $\varnothing 1 = \sin (\omega t + \delta)$. If the phase object produces a small phase

difference as compared to the wavelength, ø 1 can be described as ø 1 ≈ sin $\omega t + \delta \cos \omega t$. This shows that a phase difference of 1/4 wavelength (or $\pi/2$ rad) is generated between the direct light, sin ωt, and the diffracted light, $\delta \cos \omega t$. Through bright field optical systems, the image cannot be seen because the direct light and the diffracted light do not interfere at the image plane. If the focus is changed slightly, an image contrast appears because the optical path difference between the direct light and the diffracted light is changed, which causes interference.

The phase-contrast method was discovered by Zernike[5)6)]. It alters a phase difference of $\pi/2$ between the direct and the diffracted light from the phase object, and the image is seen by an enhanced contrast caused by the interference of the lights. The phase-contrast method was described in detail in the literature, such as by Bennett et al. (1951)[10)] and Pluta (1975, 1989)[11)]. In Japan, phase-contrast method was described by Tojo (1942)[12)]. The phase-contrast microscope is now widely used by doctors and biologists. It is used to visualize almost transparent non-staining cells and microorganisms. When the phase difference is small, the transmitted light consists of two components, the direct light (zero order diffracted light) and weak diffracted light having a phase shift of 1/4 wavelength according to the phase difference of the specimen. The phase-contrast objective lens changes the phase shift between the incident direct light and the diffracted light to 0 (same phase) or 1/2 wavelength by an internal phase plate (phase ring). Then, the direct light (background light) and the diffracted light interfere with each other on the imaging plane, and the phase object appears as a contrasted image of bright and dark. Two contrast types of phase-contrast microscopy are bright contrast and dark contrast. Dark contrast refers to an object which phase is shifted 1/2 wavelength and an object which refractive index is higher than the surroundings looks dark relative to the background.

Conventional phase-contrast microscopes are suitable for observing phase objects; however, large phase-object images lose detailed structures because of halo artifacts. Other than for thin specimens, they are often used for finding or checking cultured cells. However, when the direct light is weakened to increase the contrast to observe fine structures, the halo phenomenon of light becomes large, and the fine portion collapses. Thus it was considered not suitable for observing fine parts and thick cells. If the halo can be reduced, it will be easy to observe inner details with no staining.

3 Apodized phase-contrast microscopy

To reduce halo artifacts and to enhance details, apodized phase-contrast microscopy was developed to image fine anatomical structures in 1998–2001[13)~15)]. It achieved reducing halos and enhancing details by applying an apodization method to the conventional phase-contrast method. Apodization is an optical filtering method[16)17)]. The halos are seen as either bright areas or dark areas on phase object images, such as thick cells, which give large optical path differences (*OPD*s), or phase differences (OPD/λ), to the light wave. The unwanted halos hide small phase differences behind large phase ones and prevent high resolution. We developed and confirmed the performance of 10×, 20× and 40× magnification objectives with apodized dark contrast low, or low absorption (ADL)[18)]. Compared to off-axis illumination, the effect of apodized phase-contrast microscopy using leaf replica specimens, a common phase object specimen, was reported[19)]. At the same period, the apodized method was applied to high magnification objectives with high numerical aperture (NA) for the purpose of obtaining high-resolution images. The magnification was 100× and NA was 1.30 with oil immersion. We reported its detection capability by imaging actin bundles in living cells[20)21)]. The diameters of actin bundles ranged from 20 nm to 60 nm[22)]. Furthermore, the image formation of isolated phase objects with a very small phase difference below the diffraction limit was considered, and estimations of the size of an observable phase object was reported in detail[23)]. Brief introductions to phase contrast microscopy and apodized phase-contrast microscopy were described in *Experimental Medicine*, *Jikken-Igaku*[24)25)].

4 Principle and experiment

Apodized phase-contrast microscopy has been developed to reduce halos and to enhance details[13)]. Figure 1 shows an optical layout of apodized phase-contrast microscopy with additional bandpass filter(s). The apodized phase plate sets on the transform plane, which is usually at the objective's back focal plane. The principle of conventional phase-contrast method is shown in Fig. 2. It shows that illuminating light (incident light) is diffracted by the phase object and forms (Fraunhofer) diffraction image. The phase plate alters phase and weakens the direct light, and then enhances image contrast at the image plane (not shown). Figure 3 shows the principle of apodized phase-contrast method. Apodization areas weaken selected diffracted lights caused by large pattern or objects. Therefore, large object images have

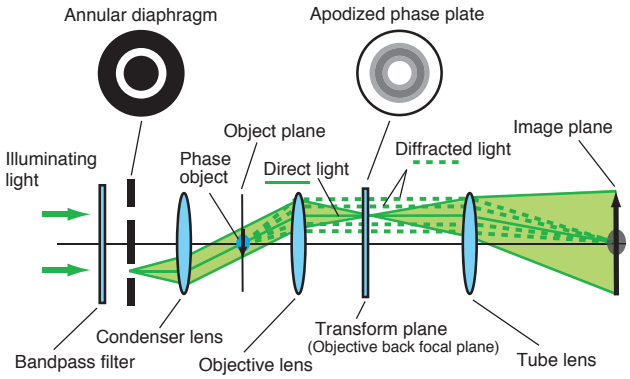

Fig. 1 Optical layout of apodized phase contrast microscopy with bandpass filters. The apodized phase plate was placed in the transform plane. It alters phase between direct and diffracted light to interfere at the image plane. One of the bandpass filters was added to provide selected wavelengths of illuminating light.

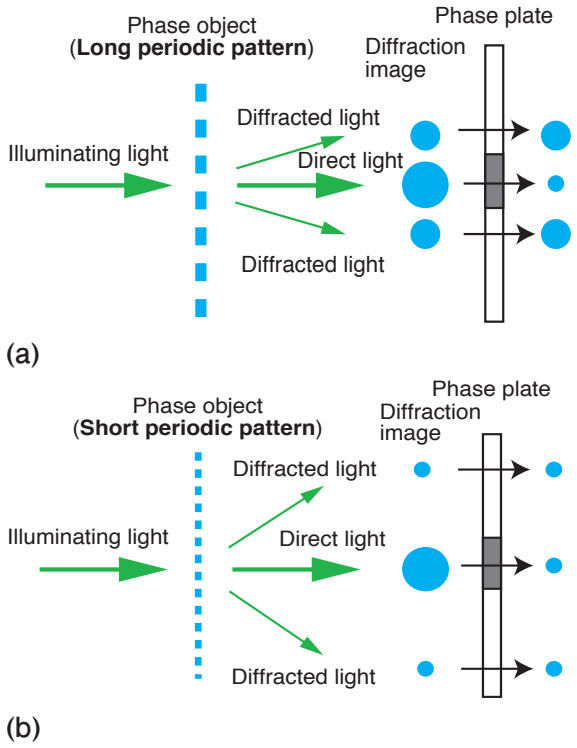

Fig. 2 Principle of conventional phase contrast [adapted from (23)]. To enhance the contrast, the direct light is weakened by the phase plate. (a) Halos appear because strong diffracted light is produced when phase difference is large. (b) Short periodic pattern diffracts light with large angle of diffraction.

weak contrast and small object images have relatively strong contrast.

Newly developed apodized phase plate has a phase ring for bright contrast, which has 1/4 wavelength phase shift throughout the most of visible region with 2% transmittances. In addition, it has two apodization areas with 8% transmittances[26)27)]. Apodized bright contrast high (ABH) performs that the direct light is especially weakened by the

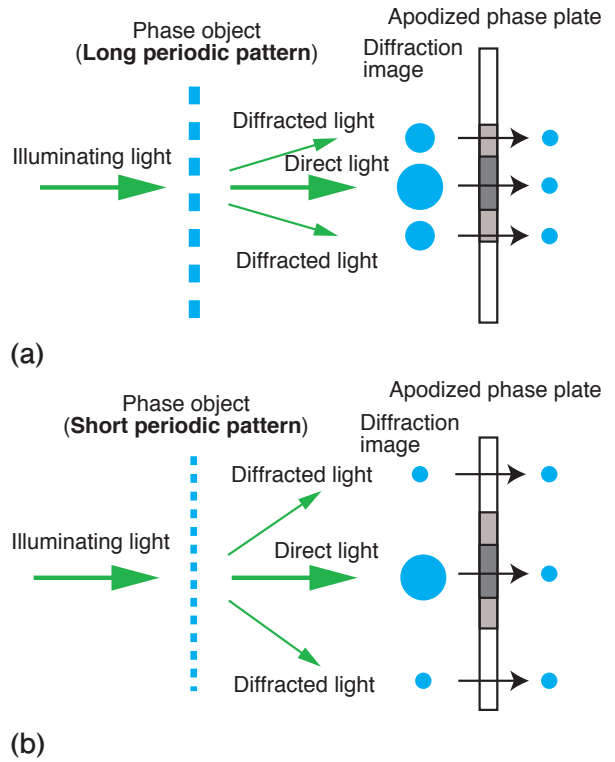

Fig. 3 Principle of apodized phase contrast [adapted from (23)], (a) Apodization areas (half tones) weaken selected diffracted lights caused by large pattern or objects. (b) Short periodic pattern diffracts light with large angle of diffraction, and passes no attenuation areas.

phase ring and selected diffracted light is weakened by apodization areas. We reported that the apodized phase-contrast microscopy (ABH) worked well for observing biological objects such as organelles in living cells. In addition, a new test method for identification of asbestos was reported[24)]. The principle of the test method was based on analysis of refractive indices. We applied this test method to distinguish organelles in unstained living cells[27)].

Microscope and specimens

Figure 4 shows an experimental set up of apodized phase-contrast microscopy. An inverted microscope was used for observing cultured cells.

Figure 5 shows comparison images between using (a) conventional bright medium (BM) and (b) apodized bright contrast high (ABH). Apodized bright contrast image provides wide latitude, for instance, nucleolus can be seen in details. The experiments were performed using the following: an inverted microscope Eclipse Ti-E with a 40× objective lens (CFI Plan Fuor 40X, 0.75 NA, developed ABH), a magnification 2.5× lens (VM 2.5X, Nikon, Japan), and a digital camera (iXon3, EMCCD 2/3", 512 × 512 pixels, Andor, USA). Bandpass filters (OD4 full width half maxi-

mum 50 nm, Edmund Optics Japan) were also used when the proposed method was performed. Specimens were cultured Cos-7 cells (African green monkey kidney fibroblast-like cells). To determine observing organelles, we compared apodized phase-contrast images with fluorescent images. Mitochondria, lipid droplets and nucleus were fluorescently labeled[27]. It was confirmed that mitochondria formed variety of shapes. Round shaped objects were difficult to distinguish mitochondria with lipid droplets. Lipid droplets were enhanced at 400 nm of wavelength, and mitochondria were relatively enhanced at 700 nm of wavelength. It was assumed that the dispersions of refractive index of lipids were larger than that of surrounding cytoplasm. By selecting wavelengths illuminations, the contrast of intracellular organelles changed. In addition, it was observed that image contrast of some dots in the nucleoli was changed by illuminating light wavelengths.

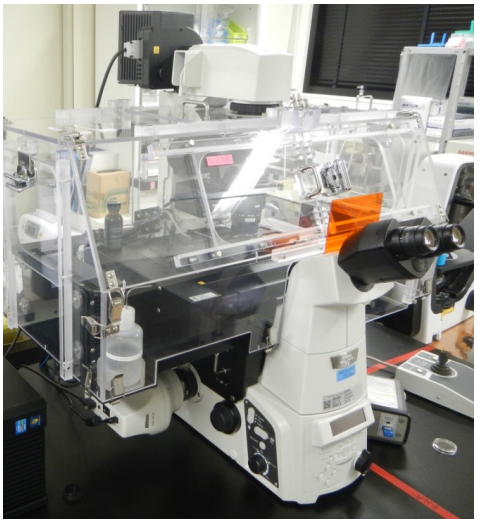

Fig. 4 Experimental set up of apodized phase-contrast microscopy with an inverted microscope and an incubation system for observing cultured cells.

Differentiation is one of the suitable applications of apodized phase-contrast microscopy due to thickness of specimens. Thick specimen (phase object) produces unwanted halos. Early embryos of mice are around 80 μm thick, while those of human are approximately 100 μm to 130 μm thick. Time-lapse imaging for observing early embryos using differential interference contrast microscopy has been proposed and used in assisted reproductive technology (ART)[28]. Apodized phase-contrast microscopy is also a good method for ART application because of resolution. In application for differentiation, early embryos were observed using apodized phase-contrast microscopy. We compared images among with conventional phase-contrast objectives and an apodized phase-contrast objective for capturing cultured mouse early embryos. Halo images were seen in inner early embryos using the conventional phase-contrast objectives. Their images obstructed detailed structure images. On the contrary, clear images were obtained using the apodized phase-contrast objective. Small granules were observed using ABH microscopy[29]. Figure 6 shows a micrograph of cultured mouse early embryos. Finer details appeared using ABH than any conventional type. Fine granules in the perivitelline space and fibrous structures in the cell body were observed.

In apodized phase-contrast microscopy, fibrous structures in mouse and human embryos and oocytes, as well as fine granules were observed[29]. Fine granules in the perivitelline

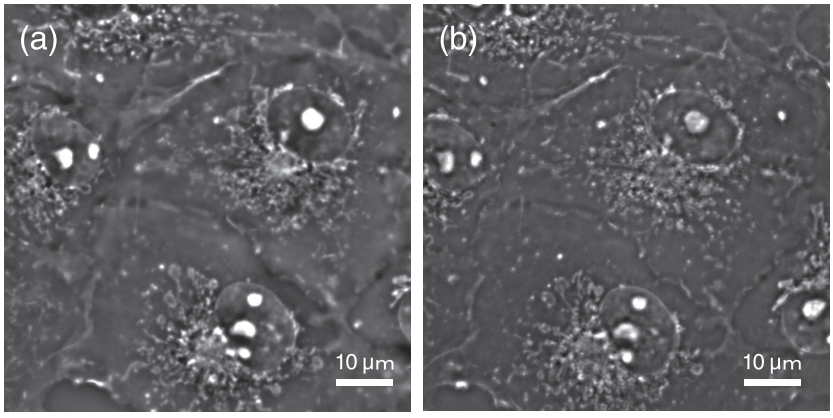

Fig. 5 Micrographs of Cos-7 cells using (a) conventional bright contrast medium (BM) and (b) apodized bright contrast high (ABH) [adapted from (23)]. Halo is useful for finding, but it obstructs image details, e.g. nucleoli's inner detail. Specimen: Cos-7, monkey kidney tissue origin cells. Objective lenses: magnification 40×, numerical aperture 0.75 (CFI Plan Fluor 40X, 0.75 NA).

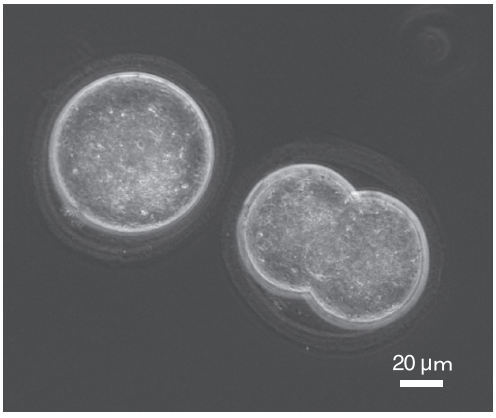

Fig. 6 Micrograph of mouse early embryos [adapted from (23)]. Enhanced contrast image. Minute granules or droplet were observed in the perivitelline space between cell membrane and zona pellucida.

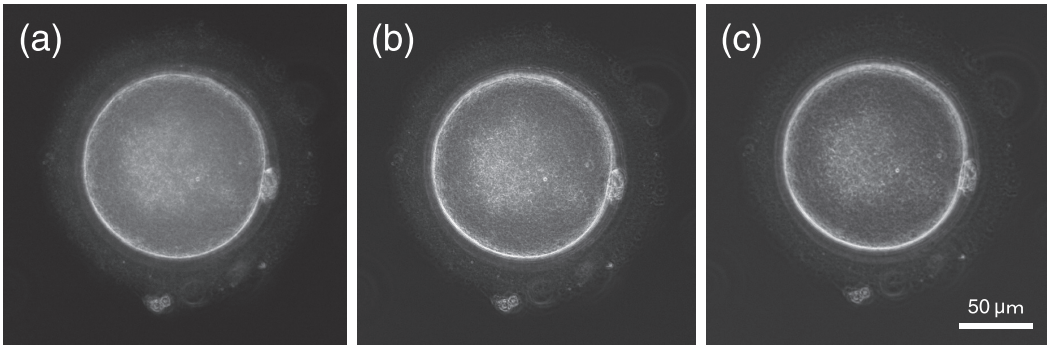

Fig. 7 Granularity images in human oocyte without staining, using selected wavelength illuminations. Centre wavelengths of illumination were (a) 450 nm, (b) 550 nm and (c) 650 nm. More contrast images of granularity (centre part) were obtained using 650 nm illumination than using 450 nm. Dispersion seems different between granularity and fibrous structures in the surrounding area. Objective lens: magnification 40×, numerical aperture 0.75 (CFI Plan Fluor 40X, 0.75 NA, ABH).

space were observed in some human embryos. The granularity was observed not as granular structures but as fibrous structures with higher contrast than surrounding area. Embryo images without staining, that imaged using bandpass filters. Higher contrast images of granularity were obtained using 650 nm illumination than with 450 nm (Fig. 7). Dispersion seems different between granularity and fibrous structures in the surrounding area. It was showed that this microscopy improves the visualization of human embryos and oocyte for clinical use. These experiments were performed using the following: an inverted microscope Eclipse Ti-E with a 40× objective lens (CFI Plan Fluor 40X, 0.75 NA, developed ABH, Nikon, Japan), and a digital camera (DS-Ri2, 24 mm × 35 mm, Nikon, Japan). A stage-top incubator (Tokai Hit, Japan) was also used.

5 Conclusion

Apodized phase-contrast microscopy and its biomedical applications were discussed. Structures were distinguished using apodized phase-contrast microscopy with bandpass filters. For living cell observation, attempts to identify intracellular organelles by forming phase-contrast images at specific wavelengths were described. In ART, culturing for several days by time-lapse imaging was performed. Very small granules in the cell were observed by time-lapse imaging at high speed. Intracellular organelles without staining and several intracellular organelles can be observed and distinguished using apodized phase-contrast microscopy at specific wavelengths of light. This method can be used for observing cellular organelles without staining. Apodized phase-contrast microscopy will be widely used for time-lapse and live-cell imaging. Analysis of intact intracellular organelles will elucidate the structure and function of living organisms. (Most of this review was presented at OPTIC 2019 in Taiwan[30]).

Acknowledgements. I am deeply grateful to Prof. Tetsu Tanaka (Tohoku University); Dr Kaoru Katoh, Ms Yoshie Kawamura (AIST); Dr Yasuyuki Mio, Dr Yoshiteru Kai (former), Ms Ayana Sonoda, Mr Keitaro Yumoto, Mr Jiroh Yamauchi, Mrs Toko Shimura (Mio Fertility Clinic); Dr Radek Pelc (Czech Academy of Sciences); Prof. Yi-Chin Fang (NKUST, Taiwan); Dr Tadao Tsuruta, Mr Toshiaki Nihoshi, Mr Shinjiro Kawashima, Mr Ryuichi Hoshika, Dr Yusuke Taki, Dr Seiji Nakano, Mr Makoto Hosobuchi, Mr Fumihiro Dake, Mrs Akiko Furuta and many colleagues (Nikon Corporation).

References

1) E. Abbe: “On the estimation of aperture in the microscope”, *J. Royal Microscopical Society*, **1** (1881), 388–423.
2) Lord Rayleigh: “On the theory of optical images, with special reference to the microscope”, *Philosophical Magazine*, **XLII** (1896), 167–195.
3) Lord Rayleigh: “On the theory of optical images, with special reference to the microscope (Supplementary paper)”, *J. Royal Microscopical Society*, **23** (1903), 474–482.
4) A. Köhler: “New method of illumination for photomicrographical purposes”, *J. Royal Microscopical Society*, **14** (1894), 261–262.
5) F. Zernike: “Das Phasenkontrastverfahren bei der Mikroskopischen Beobachtung”, *Z. Technische Physik*, **16** (1935), 454–457.
6) F. Zernike: “How I discovered phase contrast”, *Nobel Lecture* (1953).

7) F. H. Smith: “Improvements in or relating to microscopy”, U.K. Patent GB 639,014 (1950).
8) G. Nomarski: “Interferential polarizing device for study of phase objects”, U.S. Patent 2,924,142 (1960) Filed 1953.
9) R. Hoffman and L. Gross: “Modulation contrast microscope”, *Appl. Opt.*, **14** (1975), 1169–1176.
10) A. Bennett, H. Osterberg, H. Jupnik and O. Richards: *Phase Microscopy, Chap. 2 An elementary theory of phase microscopy*, (John Willey & Sons, Inc., New York, 1951) pp. 13–74.
11) M. Pluta: *Advances in Optical and Electron Microscopy, Vol. 6 Non-standard methods of phase contrast microscopy*, (Academic Press, London, 1975) pp. 50–133.
12) S. Tojo: *Lens, Chap. 5, Bunkaino-to Bairitsu-no Genkai* [Limitations of resolution and magnification], (Kawade Shobo, Tokyo, 1942) pp. 86–126 (in Japanese).
13) T. Otaki: “Artifact halo reduction in phase contrast microscopy using apodization”, *Opt. Rev.*, **7** (2000), 119–122.
14) T. Otaki: “Phase contrast observation device”, Japanese Patent 3663920 B2 (2005) Filed 1998.
15) T. Otaki: “Phase contrast observation device”, U.S. Patent 6,317,261 B1 (2001).
16) T. Asakura: “Diffraction patterns with non-uniform phase and amplitude aperture illumination (I)”, *Oyo Buturi*, **31** (1962), 730–738 (in Japanese).
17) T. Asakura: “Diffraction patterns with non-uniform phase and amplitude aperture illumination (II)”, *Oyo Buturi*, **32** (1963), 180–185 (in Japanese).
18) T. Otaki, K. Katoh and F. Yoshida: “Phase objects observing methods for video microscopy: apodized phase contrast, differential interference contrast with short shear and polarizing microscope using liquid crystals”, *Electron Microscopy*, **37 Suppl. 2** (2002), 105–108 (in Japanese).
19) R. Pelc, Z. Hostounský and T. Otaki: “Correlation between off-axis illumination and apodized phase-contrast: two complimentary microscopic phase-imaging modes”, *J. Biomed. Opt.*, **13**(5) (2008), 054067.
20) T. Otaki, K. Katoh and M. Suzuki: “Apodized phase contrast microscopy reveals dynamics of organelles in living cells”, Proc. 2004 Sympos. Optics Japan, (Osaka, 2004), 34–35 (in Japanese).
21) T. Otaki and K. Katoh: “Apodized phase-contrast microscopy, theory and images”, Proc. 16th International Microscopy Congress (IMC16), (Sapporo, 2006), 1546.
22) K. Katoh, K. Hammer, P. J. S. Smith and R. Oldenbourg: “Arrangement of radial actin bundles in the growth cone of *Aplysia* bag cell neurons shows the immediate past history of filopodial behavior”, *Proc. Natl. Acad. Sci. U.S.A. (PNAS)*, **96** (1999), 7928–7931.
23) T. Otaki: Doctor Thesis, Graduate School of Biomedical Engineering, Tohoku University, Sendai (2018).
24) T. Otaki and K. Katoh: “Phase-contrast microscopy”, *Experimental Medicine*, **36 Extra** (2018), 24–25 (in Japanese).
25) T. Otaki and K. Katoh: “Apodized phase-contrast microscopy”, *Experimental Medicine*, **36 Extra** (2018), 80–81 (in Japanese).
26) T. Otaki, Y. Mori, S. Kawashima, Y. Hashimoto, M. Konishi and Y. Konishi: “Finding and identification of asbestos and fibrous materials using apodized phase contrast microscopy”, *Fibrous Material Research*, **4** (2017), 62–66 (in Japanese).
27) T. Otaki, K. Katoh and T. Tanaka: “Identification of organelles in unstained living cells using apodized phase contrast microscopy”, Technical Digest 11th International Conference Optics-photonics Design and Fabrication (ODF ’18) (Hiroshima, 2018), 29S3–08.
28) Y. Mio: “Morphological analysis of human embryonic development using time-lapse cinematography”, *J. Mammalian Ova Research*, **23** (2006), 27–35.
29) T. Otaki, A. Sonoda, K. Yumoto, J. Yamauchi and Y. Mio: “Apodized phase contrast microscopy reveals fine granules and fibrous structures in early embryos”, Fertility Society Australia Annual Meet., FSA 2019 Abstr. (Hobart, 2019).
30) T. Otaki: “Optical design and biomedical applications of apodized phase contrast microscopy”, Optics & Photonics Taiwan, International Conference, OPTIC 2019 Abstr. (Taichung, 2019), Optical Engineering.

大瀧達朗
Tatsuro OTAKI
研究開発本部
光技術研究所
Optical Research Laboratory
Research & Development Division

ヒト大腸がん組織近傍の暗視野顕微観察像の偏光特性

藤井　透，山崎康子，齋藤直洋，澤田正康，成田　亮，齋藤　拓，Heather L Durko，
Photini Faith Rice，Gabrielle Vanessa Hutchens，Joceline Dominguez-Cooks，
Harrison Taylor Thurgood，Swati Chandra，Valentine Nfonsam，
Jennifer Kehlet Barton

Polarization characteristics of dark-field microscopic images of human colon tissue adjacent to tumor†

Toru FUJII, Yasuko YAMASAKI, Naooki SAITO, Masayasu SAWADA, Ryo NARITA, Taku SAITO,
Heather L DURKO, Photini Faith RICE, Gabrielle Vanessa HUTCHENS, Joceline DOMINGUEZ-COOKS,
Harrison Taylor THURGOOD, Swati CHANDRA, Valentine NFONSAM and Jennifer Kehlet BARTON

イメージング技術を用いたがんの早期検出は患者の生存率を大きく左右する．染色なしの従来の顕微画像に加え，共焦点顕微鏡，光干渉断層法，拡散反射分光法，などの情報を従来の医療光学画像に加えて使用し，in situ で早期癌を検出する多くの研究がなされている．豊富な偏光情報を有するミュラー偏光顕微測定を行い，組織による偏光変換のパラメーター空間の構造を調査するために，複数の照明波長で測定されたヒト大腸組織のミュラー行列成分を主成分分析した．またミュラー行列をコヒーレント行列にマッピングして分析し，固有値分析を行った．がん近傍領域の主成分分析を散布図表示した結果，非がん，非がんとがんの中間，がん，の 3 つのタイプに別れ，がんタイプは第 5 主成分以降の量が正常値の 3 倍程度見られた .

Early detection of cancer through medical imaging has a critical impact on patient survival rates. There are many efforts for detecting early cancer in situ using advanced optical imaging. Unlike traditional medical optical imaging of biological tissues, which only provides information about surface morphology, these advanced modalities provide information on subsurface structure or function, without the need for staining, including confocal microscopy, optical coherence tomography, diffuse reflectance spectroscopy, and Mueller polarimetry. We analyzed Mueller matrix components of human colon tissue measured by imaging polarimeter microscope, at illumination wavelengths of 405, 442, 473, 543 and 632 nm, by principal components analysis in order to separate novel information from traditional non-polarized gray image and to investigate the structure of the parameter space of polarization transformation by tissue. We also analyzed Mueller matrix by mapping it to coherent matrix and performed eigenvalue analysis. 99% information exists from first to fourth principal components and polarization information is less than 10% of the total information of Mueller matrix. Scatter plotted principal components of the non-cancer tissue adjacent to the affected area visually categorized in three types of non-cancer, between noncancer and cancer, and cancer. Residues of the first to fourth principal components of the last type showed abnormality, whose value is three times larger than the noise level of the instrument used.

Key words 偏光，主成分分析，ヒト大腸がん，暗視野照明，ミュラー行列，コヒーレント行列，固有値分析，エントロピー
polarization, principal component analysis, human colon cancer, dark-field illumination, Mueller matrix, coherent matrix, eigenvalue analysis, entropy

1 INTRODUCTION

Early detection of cancer through medical imaging has a critical impact on patient survival rates. Using traditional medical optical images of tissue, a convolutional neural network (CNN) showed performance better than the expert specialist, as demonstrated by AlphaGo developed by Alphabet Inc.'s Google DeepMind. Recently, CNN has been shown to detect gastric cancer as accurately as an experienced endoscopist[1]. CNN must become a powerful tool with tradi-

† This paper was modified from Ref 21 and added a new result as chapter 4.

tional visible medical images, whose performance is as high as doctors.

There are many efforts for detecting early cancer for in situ usage using other modalities than the traditional images, which contain additional information other than conventional micrographs of surface morphology, without staining. Fast and minimally invasive optical techniques such as confocal microscopy[2] and optical coherence tomography (OCT)[3] are well-suited for producing detailed morphological characterizations of small (mm^2) samples.

Polarization interaction is used in diffuse reflectance spectroscopy[4] and Mueller polarimetry[5] imaging because polarimetry is sensitive to micro to nanometer structures as is explained by Mie scattering theory[6]. Backman et al[7], present an optical-probe technique of based on light-scattering spectroscopy that is able to detect precancerous and early cancerous changes in cell-rich epithelia. They utilized the nature of early cancer cells which alter the epithelial-cell architecture in which the nuclei become enlarge. The diameter of non-dysplastic cell nuclei is typically 5–10 μm, whereas dysplastic nuclei can be as large as 20 μm across[8].

Intensive works concerning to Mueller matrix macro imaging of human colon tissue for cancer diagnostics with Mueller matrix decomposition to extract the essential polarimetric effects, namely the diattenuation, the retardation and the depolarization was done[9][10].

Polarization imaging with Monte Carlo simulations of backscattering Mueller matrix macro images of colon tissue were performed Novikova et al.[11], who measured spectral Mueller matrix images of *ex vivo* human colon tissue and have shown with experiments and modeling that light scattering by small scatterers and light absorption are the key factors for observed polarimetric image contrast.

An imaging polarimeter microscope that operates in a backscattering configuration has been developed for usage of tissue classification and early cancer detection[12][13]. The difference between the mean measured Mueller matrix values of healthy and cancerous human colon tissue agreed with previously reported results.

W. Wang et al.[14] measured histologically sliced sample Mueller matrix of the principal components analysis (PCA) derived from Mueller matrix elements for tissue differentiation.

In order to investigate polarization transformation dissect in pure components represented using Jones matrix and depolarization components induced by various human colon tissues, we analyzed 16 Mueller matrix components, measured by the imaging polarimeter microscope, by PCA. Each principal component was examined by comparing correlation to non-polarized gray images, which includes traditional tissue morphological information used in CNN cancer detection. We also mapped Mueller matrix to coherent matrix and performed eigenvalue analysis.

2 PRINCIPAL COMPONENT ANALYSIS

Mueller matrix components of human colon tissues from 21 patients, measured using our imaging polarimeter microscope[13] with 5x objective and 442 nm (FWHM < 3 nm) illumination, were used in our analysis. There are three types of human colon tissues, Tumor, Adjacent taken apart from 5 mm from Tumor edge, and Normal from 50 mm apart from Tumor edge.

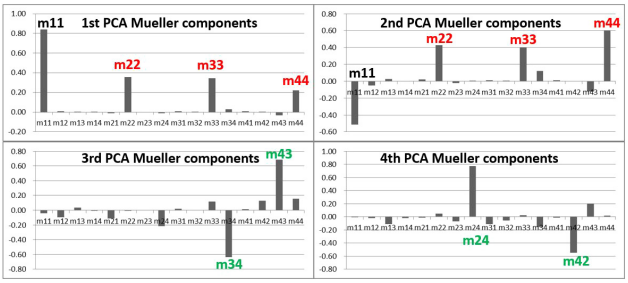

Fig. 1 Mueller matrix components of from first to fourth principal components of all 21 patients' tissues. Average vector of all images is 0.3 times of 1st PCA vector.

The imaging polarimeter system consists of an episcopic illumination system capable of dark-field illumination and a polarimetric imaging system for measuring the state of polarization (SOP) of scattered light from the tissue sample positioned at the microscope's specimen stage.

Figure 1 shows Mueller components of common PCA axes from 1st to 4th components analyzed by using 123 images of 21 patients. We also calculate PCA axes of each 123 images and found that 89.3 +/− 6.2% of the each 4-dimensional coordinate's space were found in the common PCA 4-dimensional space.

Figure 2 shows cumulative contribution rate principal

PC	value
1st	0.912
2nd	0.049
3rd	0.017
4th	0.012
5th	0.004
6th	0.003
7th	0.001

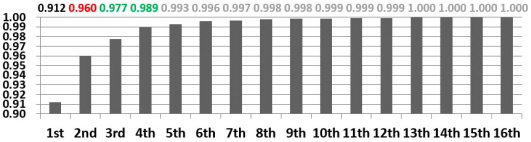

Fig. 2 Cumulative contribution rate principal components from 1st to 16th. Horizontal axis indicates number of cumulative components, in which components were added from 1st to N-th components. Vertical axis indicates value of cumulative components. A 4th cumulative component is 0.989.

components from 1st to 16th. Almost information of 99% is included from 1st to 4th PCA space.

When we treat these 4 matrices from 1st to 4th as Jones N-matrix[15], 1st to 4th axes correspond to scalar dissipation (extinction) i.e., attenuator (91.2% information), scalar depolarization (polarization extinction, 4.9% information), retardation difference between S1 and − S1 i.e., waveplate of S1 axis (1.7%), retardation difference between S2 and - S2 i.e., waveplate of S2 axis((1.2%). 5th and 6th (not shown in Fig. 1) correspond to transformation from S1 to S2 and S3 (0.4%), and transformation between S1 and S2 (0.3%).

Wang et al.[14] reported that significant differences in most parameters including retardance, depolarization, linear retardance, linear depolarization and circular depolarization between normal and cancer gastric samples and found that the combination of linear depolarization and linear retardance shows the best overall classification accuracy for gastric samples. In our case, for colon tissue, significant differences in polarization parameters were observed in the linear depolarization and linear retardance, which are the parameters for gastric cancer classification. The freedom of polarization parameter of colon might be slightly different from gastric of the stomach.

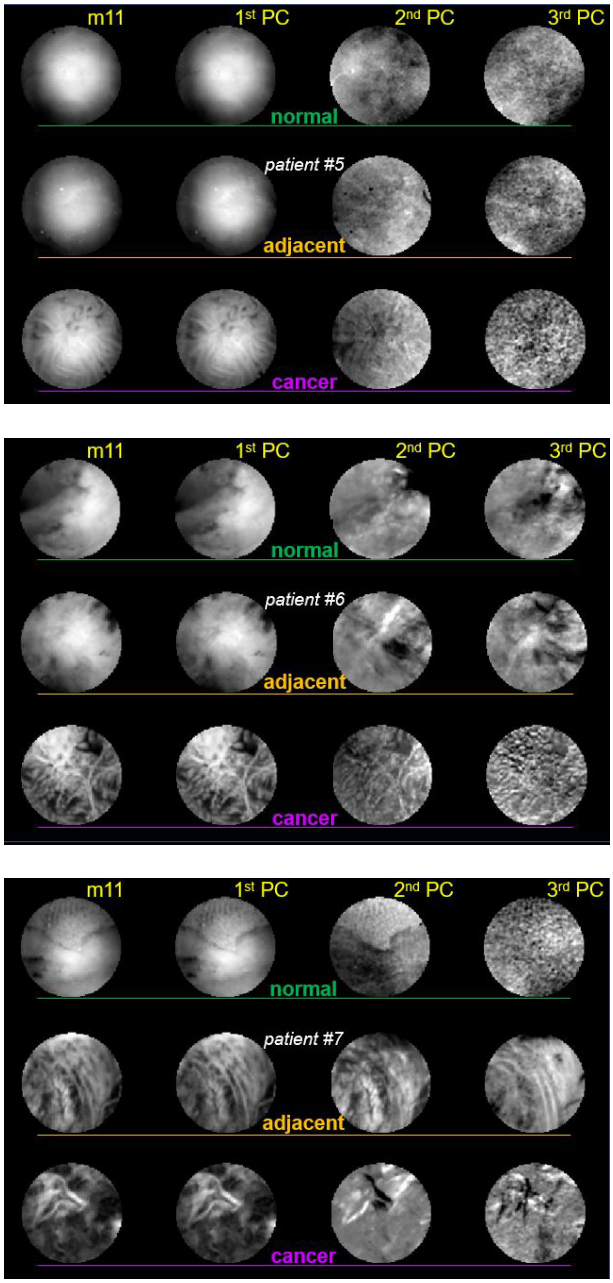

Fig. 3 m11, 1st to 3rd PCA score normal, adjacent and cancer images patient 5, 6 and 7. Field of view is 3.67 mm. Fine structures are not always related to each other.

Figure 3 shows m11 and 3 principal component images. As discussed above, we can interpret each image corresponding to gray image, which is similar to m11 image, depolarization component image, wave plate component images. The perturbation of scalar intensity and scalar depolarization are seen in 1st and 2nd PCA score images, whose modulations are closely related each other. The trace of intensity remains in 3rd PCA score images as seen in patient 5 cancer images, when an image intensity modulation is large.

Fine structures observed in 2rd score and 3rd score have different information from 1st score image, which is assumed to be traditional images. This result confirmed the high rate existence of information in 3-dimensional PCA space and the high sensitivity of the instrument we used for investigating polarization interaction of human colon tissues with high special resolution. However, no significant differences in the images of the adjacent tissue could be observed.

3 EIGENVECTOR ANALYSIS AND ENTROPY

Mueller matrix M_{ij} can be mapped to coherent matrix C_{ij} by (1), η_k is Dirac matrix[5].

$$C = m_{ij}\eta_{4(i-1)+(j-1)},\ 1 \le i, j \le 4, \eta_K, 0 \le k \le 15 \quad (1)$$

C_{ij} contains four eigenvectors, which correspond to 4 Jones matrices. Target entropy H_T is calculated by (2)[14)15)].

$$H_T = -\sum_{i=1}^{4} P_i \log_4 P_i \quad (2)$$

$$P_i = \frac{\alpha_i}{\sum_{j=1}^{4} \alpha_j}$$

α_j: eigenvalue of **C**

There are several methods to quantify entropy, which are related to such as depolarization index[16], average degree of polarization[17], and several decomposition based methods[18)~20)]. We used entropy because decomposed Jones matrix, which has the largest eigenvalue, can be used to

Table 1 Response of entropy against each patient with more precise diagnosis. Value of Site 1 and 2: Difference of mean entropy between tumor image pixels and normal image pixels (~5400 pixel each). Unit is a standard deviation of the each patient data. Higher number indicates that the tumor entropy is lower than that of normal, which means entropy response is positive and effective. Minus sign means tumor entropy is higher than normal one. We also analyzed images of patients 17 to 21, not shown in this table without precise clinical diagnosis nor pathology from hospital.

Patient No	Site1	Site2	Clinical Diagnosis	Pathology from hospital [a]	PCA type
1	**4.7**	**4.4**	right colon cecal mass	tubulovillous adenoma	N/A
2	0.1	0.7	sigmoid colon cancer	municous adenocarcinoma, low grade; T4aN1	normal
3	**1.5**	**1.2**	rectosigmoid colon mass	T4aN1a; focally invasive adenocarcinoma, moderately differentiated	normal
4	**1.8**	**2.3**	metastatic colon cancer	T3N1a adenocarcinoma	**A on C**
5	**2.9**	**3.9**	distal sigmoid colon adenocarcinoma staged as a T2N0M0 preop	well differentiated invasive adenocarcinoma arising from tubulovillous adenoma; pT1N1b	**between**
6	**5.1**	**2.2**	rectal mass	colonic mucosa fragments w/high-grade dysplasia concerning for invasive disease.	normal
7	**3.6**	**3.0**	rectal adenocarcinoma	ypT4bN0M1c; G2* moderately differentiated	**A on C**
8	**2.9**	−0.2	Cecal Mass	Tubulovillous adenoma	normal
9	0.2	0.0	Rectal cancer with a bowel obstruction	T3N2, invasive poorly differentiated adenocarcinoma	normal
10	0.5	**2.3**	Distal rectal polyp	Tubular adenoma	normal
11	**2.3**	**4.3**	Distal sigmoid colon cancer	pT3N0M0, Invasive adenocarcinoma, moderately to poorly differentiated, involving pericolonic adiposetissue	**between**
12	−1.2	−0.9	Ascending colon cancer	Sessile serrated adenoma with cytologic dysplasia	normal
13	**2.4**	**2.9**	Hepatic flexure adenocarcinoma		**between**
14	-1.9	−2.4	Rectal Cancer, patient 62 new mass, after chemoradiation	Invasive adenocarcinoma, T4bN1cM1c	normal
15	**4.2**	**4.1**	Sigmoid colon cancer	Medullary carcinoma, T4aN2b	**between**
16	−2.5	−3.5	Rectal cancer post chemotherapy	Moderately differentiated invasive adenocarcinoma, T3, N0	normal

[a] Staging index, Tumor (T): Tumor grown index, Node (N): Tumor spread index, Metastasis (M): Cancer metastasized index, *G2: the second subphase of interphases in the cell cycle directly preceding mitosis.

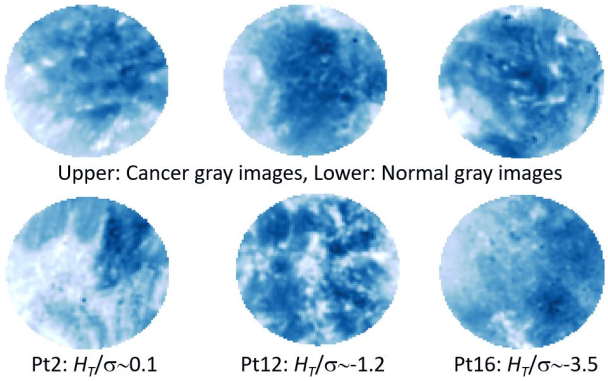

Fig. 4 Upper images: Gray scale traditional images of cancer, whose entropy is fairly lower than that of the normal images of the same patient. Lower images: Entropy images of the upper images. Field of view is 3.67 mm.

know optical characteristics when the largest eigenvalue is fairly larger than that of the rest ones.

Table 1 is an index that uses entropy and is shown in the columns of Site 1 and Site 2 and corresponding information of clinical diagnosis and Pathology from hospital. Totally analyzed sites i.e., images are 42 and 29 sites indicated lower entropy than that of normal site by the standard deviation of 5400 pixel data in each image. This result is well correlated with 3-dimensional PCA projected result shown in figure 3 because 2nd PCA axis correlates to a direction of a degree of depolarization.

The largest discrepancy is seen in the patients who got chemoradiation and chemotherapy. Even there is a correlation between entropy and cancer, as was shown in Fig. 4, entropy responses, in some cases, also depend on the apparent morphology. This table also indicates that the current diagnosis is not simply related to entropy.

4 PRINCIPAL COMPONENT SCATTER DIAGRAM

Tissue adjacent to the affected part visually determined as cancer and visually determined as non-cancerous is of great interest as a research subject for dysplasia that transitions from normal tissue to early cancer. Figure 5 shows the example of distribution of the 1st and 2nd score principal component scatter diagram.

The distribution of the three types of tissue, as is indicated c: cancer, a: adjacent and n: normal in Fig. 5 on the scatter plot can be roughly divided into three patterns.

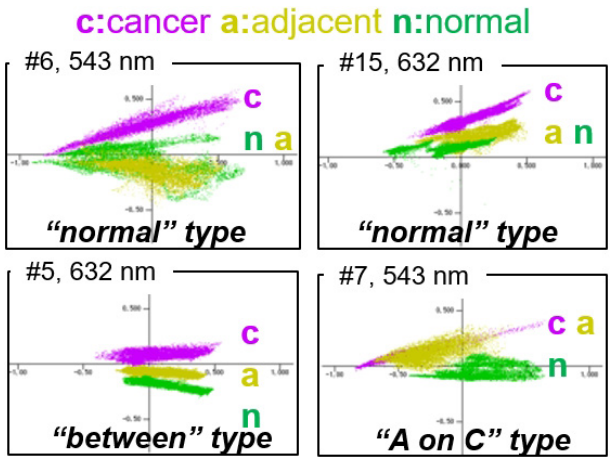

Fig. 5 1st and 2nd score principal component scatter diagram. Lateral and vertical axes are 1st and 2nd principal components, respectively. Each plotted region colored by purple, yellowish brown and green is cancer, adjacent and normal, respectively. "#" and nm indicates a patient number in table1 and illumination wavelength, respectively.

Which patterns belonged to each patient is shown in the rightmost column of Table 1. 1st pattern, called "normal" in Table1 shown in upper two scatter diagrams indicates distribution of the adjacent and the normal area overlap. The adjacent plots are located between the cancer and normal plots shown in #5, 623 nm plot as 2nd pattern, which is called "between" in table1. In the 3rd pattern called "A on C" of patient 7, which means adjacent is plotted on cancer region, the lower-right scatter plot in figure 5, the cancer and the transition region overlap. Residue of Mueller matrix 4 PCA components of patient 7 adjacent tissue is also three times larger than the noise level of the instrument used, as was reported in Ref. 23. Further investigation against adjacent tissue is expected to lead to early cancer detection.

5 CONCLUSION

We analyzed 16 Mueller matrix components, measured by the imaging polarimeter microscope whose illumination wavelength was 442 nm, by PCA in order to separate from traditional non-polarized gray image and to investigate polarization interaction between human colon and illuminated light. Each principal component was examined by comparing between non-polarized gray images, which is traditional tissue morphological information used in CNN cancer detection. We also analyzed the Mueller matrix by mapping it to coherent matrix and performed eigenvalue analysis. 99% information of human colon tissue exists from first to fourth principal components space and polarization information exists from second and later, whose amount is less than 10% of the total information of Mueller matrix. Optical interactions induced by each principal component from 1st to 4th are, scalar dissipation directly related to conventional image, scalar depolarization, and retarder of S1 and S2, respectively. Their percentages are 91.2, 4.9, 1.7, and 1.2. Microscopic fine structures observed in 3rd score and 4th score have different information from traditional gray images. There were several interesting examples in principal components scatter plot that non-cancer tissue adjacent to the affected area visually determined as cancer plotted between cancer and normal or on cancer. This result indicates that the relationship between 1st PCA image and 2nd PCA image, in other words, between intensity and depolarization effect, may be essential for very early development of human colon cancer. Further investigation against adjacent tissue will be performed.

References

1) Y. Sakai, S. Takemoto, K. Hori, M. Nishimura, H. Ikematsu, T. Yano and H. Yokota: "Automatic detection of early gastric cancer in endoscopic images using a transferring convolutional neural network", *Conf. Proc IEEE Eng. Med Bio Soc., Jul.*, (2018), 4138-4141.
2) James Pawley, (Ed.): *Handbook of biological confocal microscopy*, (Springer US 2006).
3) J. G. Fujimoto, C. Pitris, S. A. Boppart and M. E. Brezinski: "Optical Coherence Tomography: An Emerging Technology for Biomedical Imaging and Optical Biopsy", *Neoplasia. Jan.*, **2**(1-2) (2000), 9-25.
4) Z. Zonios, L. T. Perelman, V. Backman, R. Manoharan, M. Fitzmaurice, J. V. Dam and M. S. Feld: "Diffuse reflectance spectroscopy of human adenomatous colon polyps in vivo", *Appl. Opt.*, **38** (31) (1999), 6628-6637.
5) D. H. Goldstein, Polarized Light, CRC Press, (2003).
6) V. V. Tuchin, L. Wang and D. A. Zimnyakov: *Optical Polarization in Biomedical Applications*, (Springer Science & Business Media 2006).
7) V. Backman, R. Gurjar, K. Badizadegan, L. Itzkan, R. R. Dasari, L. T. Perelman and M. S. Feld: "Polarized light scattering spectroscopy for quantitative measurement of epithelial cellular structures in situ", *IEEE J. Sel. Top. Quantum Electron.*, **5** (1999), 1019.
8) V. Backman, M. B. Wallace, L. T. Perelman, J. T. Arendt, R. Gurjar, M. G. Mueller, Q. Zhang, G. Zonios, E. Kline, T. McGillican, S. Shapsshay, T. Valdes., K. Badizadegani, J. M. Crawford, M. Fitzmaurice, S. Kabani, H. S. Levin, M. Seiler, R. R. Dasari, I. Itzkan, J. V. Dam and M. S. Feld: "Detection of preinvasive cancer cells", *nature*, **406** (2000), 35.
9) S. Alali and A. Vitkin: "Polarized light imaging in biomedicine: emerging Mueller matrix methodologies for bulk tis-

sue assessment", *J. Biomed. Opt.*, **20**(6) (2015), 061104.

10) V. V. Tuchin: "Polarized light interaction with tissues", *J. Biomed. Opt.*, **21**(7) (2016), 071114.
11) T. Novikova, A. Pierangelo, S. Manhas, A. Benali, P. Validire, B. Gayet and A. De Martino: "The origins of polarimetric image contrast between healthy and cancerous human colon tissue", *Appl. Phys. Lett.*, **102** (2013), 241103.
12) Z. Chen, Y. Yao, Y. Zhu and H. Ma: "A collinear backscattering Mueller matrix microscope for reflection Muller matrix imaging", *Proc. of SPIE*, **10489** (2018), 104890M-1.
13) N. Saito, K. Sato, T. Fujii, H. L. Durko, G. L. Goldstein, A. H. Phillips, J. Dominguez-Cooks, G. V. Hutchens, H. T. Thurgood, P. F. Rice and J. K. Barton: "Multispectral Mueller matrix imaging dark-field microscope for biological sample observation", *Proc. SPIE*, **10890** (2019), 10890-46.
14) W. Wang, L. G. Lim, S. Srivastava, J. B.-Y. So, A. Shabbir and Q. Liu: "Investigation on the potential of Mueller matrix imaging for digital staining", *J. Biophotonics*, **9** (4) (2016), 364.
15) R. C. Jones: "A new calculus for the treatment of optical systems. VII. Properties of the N-matrices," *J. Opt. Soc. Am.*, **38** (1948), 671-685.
16) S. R. Claude and E. Pottier: "An Entropy Based Classification Scheme for Land Applications of Polarimetric SAR", *IEEE Transactions on Geoscience and Remote Sensing*, **35** (1997), 68-78.
17) S. R. Claude: "Polarimetry: The characterization of polarization effects in EM scattering", Dr. Thesis University of Birmingham, (1987).
18) J. J. Gil and E. Bernabeu: "Depolarization and polarization indices of an optical system" *OPTICA ACTA*, **33** (1986), 185-189.
19) R. A. Chipman: "Depolarization index and the average degree of polarization", *Appl. Opt.*, **44**(13) (2005), 2490.
20) S-Y. Lu and R. A. Chipman: "Interpretation of Mueller matrices based on polar decomposition", *JOSAA*, **13**(5) (1996), 1106.
21) T. Fujii, Y. Yamasaki, N. Saito, M. Sawada, R. Narita, T. Saito, H. L Durko, P. F. Rice, G. V. Hutchens, J. Dominguez-Cooks, H. T. Thurgood, S. Chandra, V. N. Nfonsam and J. K. Barton: "Polarization characteristics of dark-field microscopic polarimetric images of human colon tissue," *Label-free Biomedical Imaging and Sensing (LBIS), Proc SPIE*, **10890** (2019), 108902J.

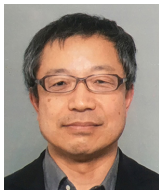

藤井　透
Toru FUJII
研究開発本部
光技術研究所
Optical Research Laboratory
Research & Development Division

山崎康子
Yasuko YAMASAKI
研究開発本部
光技術研究所
Optical Research Laboratory
Research & Development Division

齋藤直洋
Naooki SAITO
研究開発本部
光技術研究所
Optical Research Laboratory
Research & Development Division

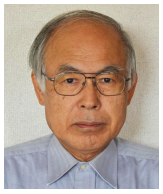

澤田正康
Masayasu SAWADA
株式会社ニコンシステム
Nikon System Inc.

成田　亮
Ryo NARITA
株式会社ニコンシステム
Nikon System Inc.

齋藤　拓
Taku SAITO
株式会社ニコンシステム
Nikon System Inc.

Heather L DURKO
Nikon Research Corporation America

Photini Faith RICE
The University of Arizona

Gabrielle Vanessa HUTCHENS
The University of Arizona

Joceline DOMINGUEZ-COOKS
The University of Arizona

Harrison Taylor THURGOOD
The University of Arizona

Swati CHANDRA
The University of Arizona

Valentine NFONSAM
The University of Arizona

Jennifer Kehlet BARTON
The University of Arizona

エッジ照明法を使ったX線位相コントラストイメージングの産業応用に関するニコン/UCL共同研究：新しい補完的な画像情報とサブピクセル特性の検出

松永教仁，矢野和弘，David BATE，Marco ENDRIZZI，Alessandro OLIVO

The Nikon/UCL collaboration on industrial applications of Edge-Illumination X-ray Phase Contrast Imaging: detection of new complementary information and of sub-pixel features

Norihito MATSUNAGA, Kazuhiro YANO, David BATE, Marco ENDRIZZI and Alessandro OLIVO

2012年以降，ニコンとユニバーシティ・カレッジ・ロンドン（以下，UCL）は，UCLが開発したエッジ照明法と呼ばれる通常の実験室サイズで運用可能な新しいX線位相コントラスト法について，共同研究を行っている．最近，その共同研究の焦点は，産業分野への応用に移行した．X線位相コントラスト法には3つの利点がある．1）従来のX線吸収イメージングでは視認できない被検物の詳細な構造を示すことができる．2）従来のX線吸収イメージングでは得られない補完的な画像コントラスト情報を提供することができる．3）暗視野像を利用することにより，装置解像度の限界を下回る被検物の詳細な構造を検出できる．この論文では，それらすべてについて例示する．特に，3）において，暗視野像が装置解像度よりも小さなスケールの微細構造情報（＝サブピクセル特性）を提供することが知られている．装置解像度よりも細かな溝が彫られた被検物を計測することにより，解像度限界を下回る微細構造も検出できることを示す．より一般的に，産業用途における複合材料の検査において有益な結果が得られる．また，英国研究・イノベーション機構UKRIによるProsperity Partnershipプログラムに採択されたことにより，エッジ照明法をより高いエネルギーにまで拡張できる機会を得た．これにより，高い原子番号の素材より成る厚めの被検物や，新たな積層造形（AM; アディティブ・マニュファクチャリング）分野への応用が可能になる．

Nikon and University College London (UCL) have collaborated since 2012 on of novel, laboratory-based X-ray Phase Contrast Imaging (XPCI) methods; recently, focus has shifted to industrial application. XPCI offers three advantages: 1) it reveals details invisible to conventional X-rays 2) it allows complementary contrast modalities 3) the dark field channel allows detecting details below the resolution limit of the imaging system. This paper presents examples of all three advantages, with emphasis on the third. Specifically on this latter aspect, it is known that dark field provides microstructural information on a scale smaller than the system's resolution. By using a micro-groove sample, we show that individual features below the resolution limit can also be detected. More generally, in industrial applications, important results have been achieved in the testing of composite materials, and the award of a "Prosperity Partnership" Program by United Kingdom Research and Innovation (UKRI) will enable extending XPCI to higher energies, allowing applications to high Z, thick samples and to the emerging field of additive manufacturing.

Key words 産業用非破壊検査，微細欠陥検出，X線イメージング，X線位相コントラスト，暗視野像
Industrial non-destructive inspection, Micro crack inspection, X-ray imaging, X-ray phase contrast, Dark field

1 INTRODUCTION

Since Wilhelm Röntgen's discovery of X-rays in 1895, X-ray imaging has been one of the few technologies that allow visualizing the internal structure of a sample non-destructively. In particular, X-ray Phase Contrast Imaging (XPCI) allows obtaining high contrast for samples presenting a weak X-ray attenuation, and as a consequence it has been actively studied over recent years. Several XPCI approaches have been developed to date, including free-space propaga-

tion (propagation-based imaging)[1)2)], Bonse-Hart interferometry (crystal interferometry)[3)4)], analyzer-based imaging (sometimes referred to as "Diffraction Enhanced" Imaging)[5)~7)], Talbot interferometry (grating-based imaging)[8)~10)] and edge illumination (EI, sometimes referred to as the "coded aperture" technique)[11)~13)]. Details on the various approaches can be found in a series of reviews that were recently published[14)15)].

Among those methods, Talbot interferometry and EI have attracted particular attention thanks to the possibility to implement them with extended sources, which is one of the key requirements in terms of translation from high-end synchrotron facilities to standard labs and, ultimately, commercial systems. Our collaboration focuses on EI, mostly because of its implementation not requiring source collimation[11)~13)], achromatic properties[16)], and robustness against vibrations[17)]. The edge illumination technique was first developed in Elettra Synchrotron of Italy in the late 1990s[18)]. Currently, many experimental results have been reported, mostly based around applications in biohealth and industrial fields[11)~13)]. These highlight the technique's potential in terms of application to market, within which hard X-ray dark field imaging with incoherent sample illumination[12)13)16)] can carve its own niche thanks to its ability to visualize various microstructures of the sample using laboratory scale systems, similarly to what has been demonstrated for dark field imaging in analyzer-based imaging[19)] or Talbot interferometry[20)]. So far, this dark field channel has been related to average microscopic sample features - namely sub-pixel structures averaged over one detector pixel[10)21)~23)]. Here, besides providing additional demonstration of its inherent complementarity to both the attenuation and the differential phase channels, we focus on single, isolated sub-pixel features, showing that these can be detected by the dark field channel down to sizes well below the inherent resolution limits of the imaging system. In EI, this resolution limit (referred to as δ_{RL} in the following to avoid repetitions) extends beyond the detector's intrinsic resolution, and is equal to the smallest between projected focal spot size (= real focal spot size multiplied by sample-to-detector distance and divided by source-to-sample distance) and aperture dimension in the pre-sample mask[24)]. We also show that this limit is mostly respected in the differential phase image, therefore corroborating the theoretical framework of ref. 24, while the dark field channel enables detecting finer isolated details.

2 IMAGING PRINCIPLE

Fig. 1 shows a schematic diagram of the EI XPCI system used in this demonstration experiment. The detector is a Hamamatsu C9732DK CMOS sensor with pixel size of 50 μm. The X-ray source is a rotating anode Rigaku MM007 with a molybdenum target. The tube voltage and current settings were 35 kVp and 25 mA respectively, and the focal spot size is approximately 80 μm. The pre-sample mask, manufactured by Creatv MicroTech (Potomac, MD) by electroplating gold on a patterned graphite substrate, had a period of 79 μm and an aperture width of 23 μm.

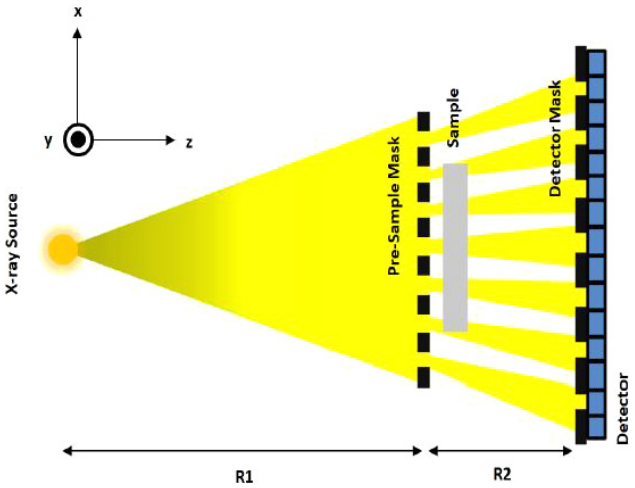

Fig. 1 Schematic representation of the laboratory-based edge-illumination X-ray imaging system used in this experiment.

The detector mask was fabricated in the same way and had a 98 μm period and 29 μm aperture width. The distances R_1 and R_2 between source and pre-sample mask and pre-sample mask and detector mask were of 1.6 m and 0.4 m, respectively which, when beam divergence is taken into account, leads to harmonic matching of the two masks. The detector itself is placed a few cm downstream of the detector mask, so that the 98 μm period of the latter projects into twice the pixel structure, leading to what we refer to as the "skipped" EI configuration[25)], used with indirect conversion detectors to reduce cross-talk between adjacent channels.

To extract the dark field signal, we start by measuring the "illumination" curve (IC) without a sample in place, i.e. the intensity variation observed at the detector when one mask (typically the pre-sample one), is scanned transversally (i.e. along x axis in Fig. 1). Fig. 2 schematizes the measurement method and highlights some key physical quantities of the IC. Following the introduction of a sample, the sample and the sample mask are moved rigidly in a series of points with respect to the stationary detector/detector mask assembly

(indicated as "System dithering" in Fig. 2(a)). The signal in the corresponding detector pixel is measured at each point, and a "sample in" IC is obtained by Gaussian fitting of the signals obtained at the various points. This fit $I_M(x)$ is then compared to the corresponding fit ($I_N(x)$) of the IC without the sample in place.

$$I_N(x) = \frac{t_N}{\sqrt{2\pi\sigma_N^2}} \exp\left[-\frac{(x-\Delta x_N)^2}{2\sigma_N^2}\right] + I_0, \quad (1)$$

$$I_M(x) = t_M\left[\frac{t_N}{\sqrt{2\pi\sigma_M^2}} \exp\left[-\frac{(x-\Delta x_M)^2}{2\sigma_M^2}\right] + I_0\right]. \quad (2)$$

The comparison between $I_M(x)$ and $I_N(x)$ allows extracting the attenuation, refraction and dark-field characteristics of the sample on a pixel-by-pixel basis. In particular, t_N, Δx_N, σ_N and I_0 in Eq. (1) are area, center, standard deviation and background value of the illumination curve without the sample. These values depend only on the characteristics of the imaging system, and are used as reference data to retrieve the sample parameters. t_M, Δx_M and σ_M in Eq. (2) are area ratio (relative area reduction), center and standard deviation of the illumination curve with the sample. These values represent the modification to the IC caused by absorption, refraction and USAXS in the sample. It is therefore possible to extract the absorption image t_M, the differential phase image Δx_M- Δx_N and the dark field (or USAXS) image σ_M^2 - σ_N^2 of the sample by measuring the IC with and without the sample in place[12)13)]. While this procedure yields

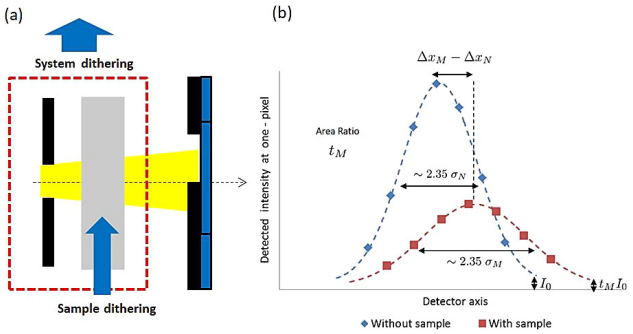

Fig. 2 (a) Schematization of the approach used to measure the illumination curve with and without the sample. "System dithering" indicates the translation in steps used to measure the illumination curve for each pixel, which is always repeated both with and without the sample. "Sample dithering" indicates an additional (optional) scan applied only to the sample, when this is sampled at a pitch finer than the pixel size. This allows accessing the ultimate resolution of the imaging system δ_{RL} as defined in the text. (b) shows example illumination curves measured with and without the sample, with the latter inducing curve broadening, intensity reduction and lateral shifts that allow extracting dark field, attenuation and refraction signals, respectively.

the above three images sampled at a pitch equal to the detector pixel size, finer sampling pitches can be accessed by displacing the sample in sub-pixel steps ("Sample dithering" in Fig. 2(a)), repeating the above procedure at each step, and interleaving the obtained oversampled images (i.e. column 1 of dithering step 1, column 1 of dithering step 2, …. column 1 of dithering step D, column 2 of dithering step 1 etc. if D dithering steps are used in total[25)]).

The ability of this procedure to yield a resolution beyond the pixel size limits is shown in Fig. 3, where the microstructure of coffee grains is highlighted in the phase image in Fig. 3(b) and confirmed by a scan of the same sample with an electron microscope (Fig. 3(c)). The attenuation image is shown in Fig. 3(a), which demonstrates the enhanced contrast provided by the phase channel; note that the two images were extracted from the same dataset according to Eqs. (1-2), and they thus have exactly the same X-ray statistics. This result also highlights that refraction (the integration of which yields the phase shift) and dark-field can be cast as line integrals, which makes 3D (computed tomography) acquisitions possible. Details can be found in references[26)~28)].

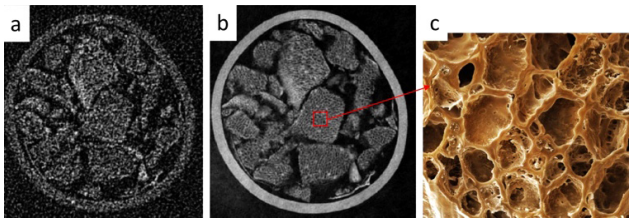

Fig. 3 Microstructure of coffee grains revealed by phase contrast (b), confirmed by al electron microscopy image of the same specimen (c). The figure also shows that conventional attenuation (a) provides much lower contrast at the same X-ray statistics.

3 EXPERIMENT

This paper presents additional data[29)] focusing on a sample specifically designed to assess the ability of the dark field image to detect individual sub-pixel features that are invisible to the other image channels. This consists of a series of microgrooves carved in a 2 mm thick acrylic substrate as shown in Fig. 4. Fig. 4(a) is a photograph of the sample, with the widest grooves clearly visible in the top right corner (highlighted by a dashed red circle). Fig. 4(b) is a schematic providing height and spacing between grooves, and the number coding we will use to refer to their individual width and depth. The depth of all grooves in the top group (1-8) is 10 μm, and their width ranges from 6 μm (groove 1 on the far left) to 200 μm (groove 8, far right). Grooves in the mid-

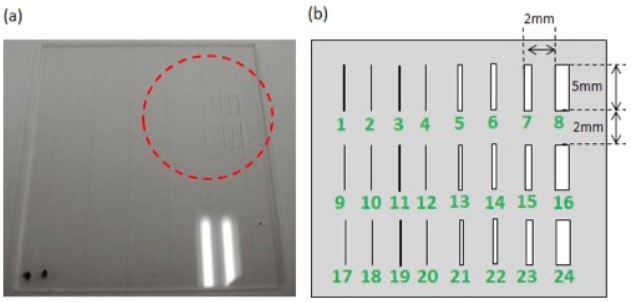

Fig. 4 (a) Photograph of the sample, with some grooves visible in the top right corner (dashed red circle) (b) schematic of the sample where grooves' height and separation are specified, and grooves are coded by numbers for ease of reference in the manuscript.

dle (9–16) and bottom (17–24) groups have the same width distribution, but depths of 50 μm and 100 μm respectively. Optical microscope imaging was used to obtain a more precise assessment of their width, e.g. grooves 17 and 18 (focus of the analysis of Fig. 5 below) had widths of 7.4 μm (as opposed to the design value of 6 μm) and 11.4 μm, respectively. All microgrooves were fabricated using the excimer laser technology.

This sample was imaged with the imaging system and parameters outlined above, and attenuation, differential phase and dark-field images were extracted by using the procedure of Eqs. (1–2). Details from the resulting images of grooves 17–24 (corresponding to the entire bottom line of the phantom) are shown in panels (a), (b) and (c) of Fig. 5, respectively. Horizontal profiles were extracted from each image, and these are reported in the same panel right above the corresponding images.

4 RESULTS AND DISCUSSION

As per the model described in ref. 24, we expect the spatial resolution δ_{RL} of the used EI system to be of the order of 20 μm, corresponding approximately to the projected focal spot and slightly smaller than the apertures in the pre-sample mask. We note that, while the detection of individual objects smaller than δ_{RL} cannot be excluded a priori (as is the case for any imaging system and its resolution), the results obtained from the attenuation and differential phase images, best appreciated in the plots above the images in of Fig. 5, are reasonably aligned with this coarse prediction. However, the visualization of finer details extends further in the dark field image, as visible from the image in Fig. 5(c) and even more clearly in the corresponding plot, where the additional detected details are highlighted by a dashed blue circle. Indeed, these details (17 and 18 in the numbered scheme of

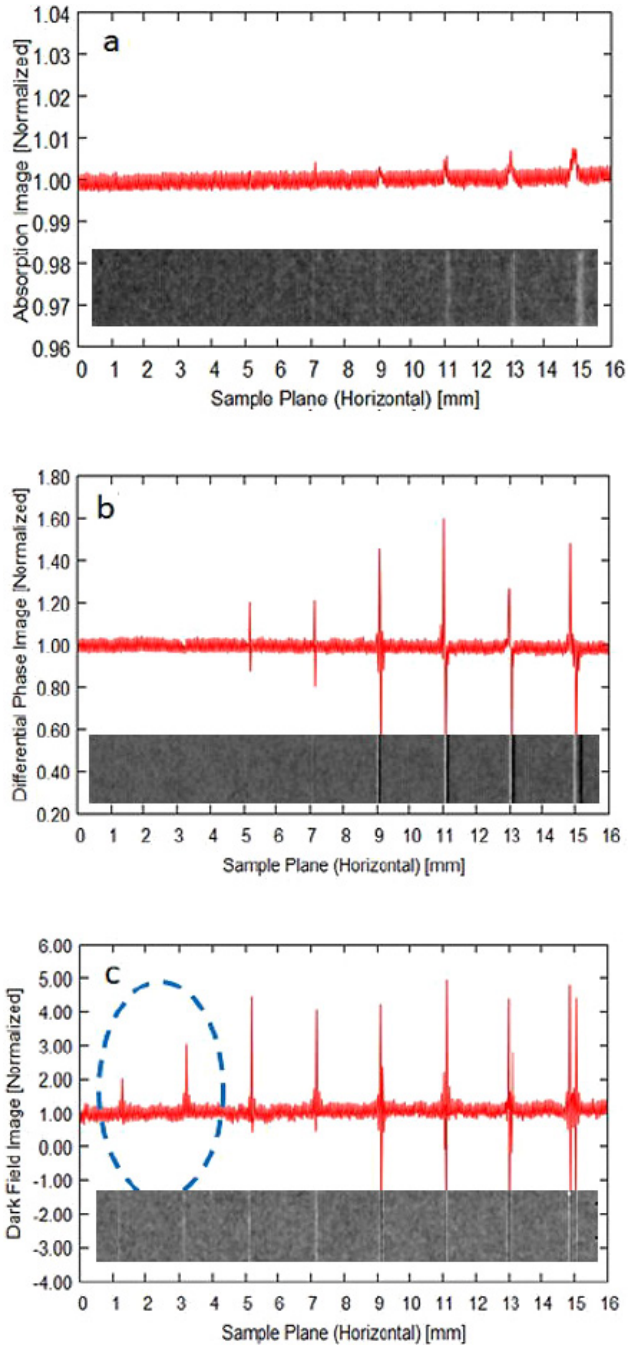

Fig. 5 Attenuation (a), differential phase (b) and dark field (c) images of grooves 17–24 (see Fig. 4(b)). Horizontal profiles were extracted from the images and are reported above all figures. A dashed blue circle in panel (c) highlights profiles of the thinnest grooves which, despite falling below the resolution limit of the imaging system δ_{RL} and indeed being invisible in the attenuation and differential phase images, are detected in the dark field image.

Fig. 4(b)) have a (measured) width of 7.4 μm and 11.4 μm respectively, therefore being significantly smaller than δ_{RL} in both cases.

As well as partly corroborating our previously developed theoretical framework, we find that these results are important, as they might suggest new application opportunities for

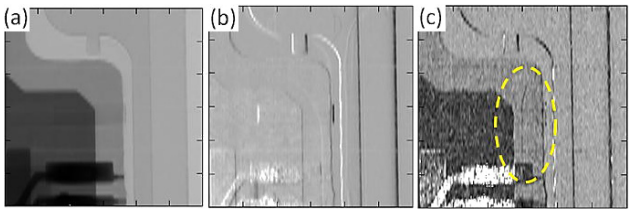

Fig. 6 Attenuation (a), differential phase (b) and dark field (c) images of part of the cracked SD card. The dashed yellow circle in (c) shows the crack, visible only in the dark field image.

the dark field imaging method. Alongside its ability to provide a signal proportional to the average concentration of sub-pixel structures, which has been repeatedly highlighted before[19)~23)], we observe here that dark field can also detect single, isolated features below the resolution limits of the imaging system, which are not picked up by the phase or attenuation channels. As a note of caution, it is important to stress that this sub-resolution detection potential depends on the sample characteristics, and in particular by the extent of the induced phase shifts, as made evident by the fact that the same fine features were not detected for the shallower grooves. This seems to indicate that it is the combination of size and signal strength that pushes a feature about the visibility threshold, an aspect that requires more detailed analysis to determine the effective bounds within which sub-resolution features are detected.

However, within these boundaries, this property may offer an opportunity to detect isolated defects or micro cracks on a scale which would not be accessible to other imaging modalities with the same level of resolution, which would find applications in non-destructive testing. As an example, Fig. 6(a)(b) and (c) show attenuation, differential phase and dark field images of a SD card with a crack respectively. A dashed yellow circle in Fig. 6(c) shows a cracked part can be seen only in the dark field channel. This result suggests that X-ray phase contrast imaging using edge illumination can be applied to non-destructive inspection of micro crack in industrial products such as electronic parts and processed fibers.

5 CONCLUSIONS AND OUTLOOK

The detection of individual sub-pixel features adds a string to the bow of an already powerful and versatile new imaging method, which recently proven transformative capabilities in the detection of damage in composite materials[30)] (Fig. 7).

At present, UCL and Nikon X-Tek Systems Ltd are working together to push the implementation of the multi-modal

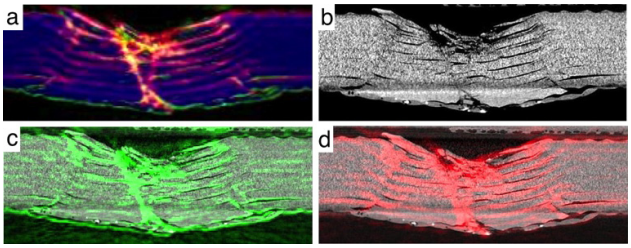

Fig. 7 Application of EI XPCI to cracks in composite materials. Panel (a) shows a “fused” image with attenuation in blue, refraction in green and dark-field in red, showing the complementarity of the channels as they emerge from different parts of the sample. Panel (b) shows a conventional micro CT for comparison. Panels (c) and (d) show an overlay of refraction and dark-field over the conventional micro-CT image, demonstrating detection of damage well beyond what can be revealed by conventional X-rays.

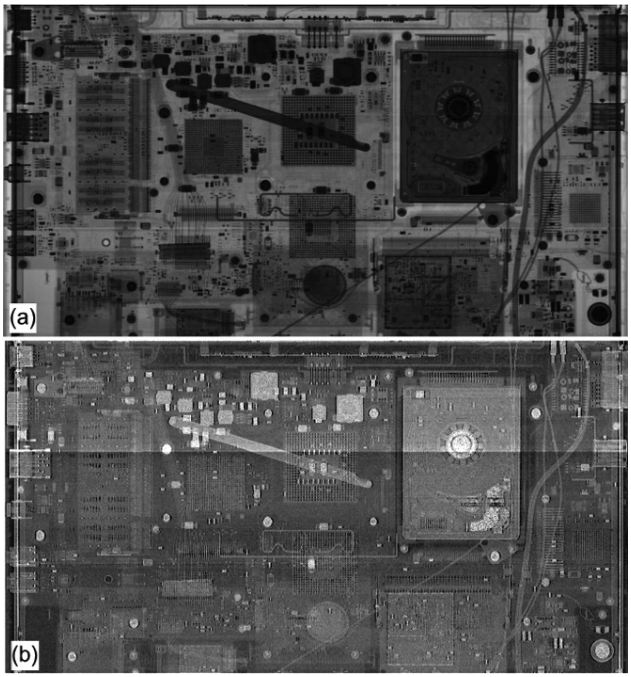

Fig. 8 Complementary images of a full laptop scanned at high X-ray energy – (a) attenuation and (b) dark-field.

X-ray methods to much higher X-ray energies. Feasibility at X-ray spectra up to 120 kVp has already been demonstrated, which enables for example the scan of a full laptop (Fig 8).

Concurrently, a pilot experiment on additive manufacturing has been conducted at the Diamond synchrotron light source in Oxfordshire, UK. Although data analysis is still underway, the ability of the dark field channel to detect small blemishes and unfused powders is already evident; once fully proven, this will be translated to conventional sources. Combining these advances with the new onesallowed by our 5-year prosperity partnership program makes us confident we will develop next-generation X-ray tools with

unprecedented capabilities for additive manufacturing and beyond.

Acknowledgements. This project was part supported by the UK Engineering and Physical Sciences Research Council Grant No. EP/I021884/1. M. E. and A. O. are supported by the Royal Academy of Engineering under the Research Fellowships and Chair in Emerging Technologies schemes, respectively.

REFERENCES

1) A. Snigirev, I. Snigireva, V. Kohn, S. Kuznetsov and I. Schelokov: "On the possibilities of x-ray phase contrast microimaging by coherent high-energy synchrotron radiation", *Rev. Sci. Instrum.*, **66** (1995), 5486.
2) S. W. Wilkins, T. E. Gureyev, D. Gao, A. Pogany and A. W. Stevenson: "Phase-contrast imaging using polychromatic hard X-rays", *Nature*, **384** (1996), 335.
3) U. Bonse and M. Hart: "AN X-RAY INTERFEROMETER WITH LONG SEPARATED INTERFERING BEAM PATHS", *Appl. Phys. Lett.*, **7** (1965), 99.
4) A. Momose: "Demonstration of phase-contrast X-ray computed tomography using an X-ray interferometer", *Nucl. Inst. and Meth. Phys. Res. A.*, **352** (1995), 622.
5) J. Davis, D. Gao, T. E. Gureyev, A. W. Stevenson and S. W. Wilkins: "Phase-contrast imaging of weakly absorbing materials using hard X-rays", *Nature*, **373** (1995), 595.
6) D. Chapman, W. Thomlinson, R. E. Johnston, D. Washburn, E. Pisano, N. Gmür, Z. Zhong, R. Menk, F. Arfelli and D. Sayers: "Diffraction enhanced x-ray imaging", *Phys. Med. Biol.*, **42** (1997), 2015.
7) I. Koyama, A. Momose, J. Wu, T. T. Lwin and T. Takeda: "Biological Imaging by X-ray Phase Tomography Using Diffraction-Enhanced Imaging", *Jpn. J. Appl. Phys.*, **44** (2005), 8219.
8) A. Momose, S. Kawamoto, I. Koyama, Y. Hamaishi, K. Takai and Y. Suzuki: "Demonstration of X-Ray Talbot Interferometry", *Jpn. J. Appl. Phys.*, **42** (2003), L866.
9) F. Pfeiffer, T. Weitkamp, O. Bunk and C. David: "Phase retrieval and differential phase-contrast imaging with low-brilliance X-ray sources", *Nat. Phys.*, **2** (2006), 258.
10) F. Pfeiffer, M. Bech, O. Bunk, E.F. Eikenberry, C. Brönnimann, C. Grünzweig and C. David: "Hard-X-ray Dark-Field Imaging Using a Grating Interferometer", *Nat. Mater.*, **7** (2008), 134.
11) A. Olivo and R. Speller: "A coded-aperture technique allowing x-ray phase contrast imaging with conventional sources", *Appl. Phys. Lett.*, **91** (2007), 074106.
12) M. Endrizzi, P. C. Diemoz, T. P. Millard, J. Louise Jones, R. D. Speller, I. K. Robinson and A. Olivo: "Hard X-ray dark-field imaging with incoherent sample illumination", *Appl. Phys. Lett.*, **104** (2014), 024106.
13) M. Endrizzi, B. I. S. Murat, P. Fromme and A. Olivo: "Edge-illumination X-ray dark-field imaging for visualising defects in composite structures", *Composite Structures*, **134** (2015), 895.
14) A. Olivo and E. Castelli: "X-ray phase contrast imaging: From synchrotrons to conventional sources", *Riv. Nuovo Cimento*, **37** (2014), 467.
15) M. Endrizzi: "X-ray phase-contrast imaging", *Nucl. Instrum. Meth. Phys. Res. A.*, **878** (2018), 88.
16) M. Endrizzi, F. A. Vittoria, G. Kallon, D. Basta, P. C. Diemoz, A. Vincenzi, P. Delogu, R. Bellazzini and A. Olivo: "Achromatic Approach to Phase-Based Multi-Modal Imaging With Conventional X-ray Sources", *Opt.Exp.*, **23** (2015), 16473.
17) T. P. Millard, M. Endrizzi, K. Ignatyev, C. K. Hagen, P. R. T. Munro, R. D. Speller and A. Olivo: "Method for automatization of the alignment of a laboratory based x-ray phase contrast edge illumination system", *Rev. Sci. Instrum.*, **84** (2013), 083702.
18) A. Olivo, F. Arfelli, G. Cantatore, R. Longo, R. H. Menk, S. Pani, M. Prest, P. Poropat, L. Rigon, G. Tromba, E. Vallazza and E. Castelli: "An Innovative Digital Imaging Set-Up Allowing a Low-Dose Approach to Phase Contrast Applications in the Medical Field", *Med. Phys.*, **28** (2001), 1610.
19) L. Rigon, H. J. Besch, F. Arfelli, R. H. Menk, G. Heitner and H.Plotow-Besch: "A new DEI algorithm capable of investigating sub-pixel structures", *J. Phys. D: Appl. Phys.*, **36** (2003), A107.
20) V. Revol, B. Plank, R. Kaufmann, J. Kastner, C. Kottler and A. Neels: "Laminate fibre structure characterisation of carbon fibre-reinforced polymers by X-ray scatter dark field imaging with a grating interferometer", *NDT and E Int.*, **58** (2013), 64.
21) S. K. Lynch, V. Pai, J. Auxier, A. F. Stein, E. E. Bennett, C. K. Kemble, X. Xiao, W.-K. Lee, N. Y. Morgan and H. Wen: "Interpretation of dark-field contrast and particle-size selectivity in grating interferometers", *Appl. Opt.*, **50** (2011), 4310.
22) T. P. Millard, M. Endrizzi, L. Rigon, F. Arfelli, R. H. Menk, J. Owen, E. Stride and A. Olivo: "Quantification of microbubble concentration through x-ray phase contrast imaging", *Appl. Phys. Lett.*, **103** (2013), 114105.
23) P. Modregger, M. Kagias, S. C. Irvine, R. Brönnimann, K. Jefimovs, M. Endrizzi and A. Olivo: "Interpretation and Utility of the Moments of Small-Angle X-Ray Scattering Distributions", *Phys. Rev. Lett.*, **118** (2017), 265501.
24) P. C. Diemoz, F. A. Vittoria and A. Olivo: "Spatial resolution of edge illumination X-ray phase-contrast imaging", *Opt. Exp.*, **22** (2014), 15514.
25) K. Ignatyev, P. R. T. Munro, R. D. Speller and A. Olivo: "Effects of signal diffusion on x-ray phase contrast images",

Rev. Sci. Instrum., **82** (2011), 073702.

26) C. K. Hagen, P. R. T. Munro, M. Endrizzi, P. C. Diemoz and A. Olivo: "Low-dose Phase Contrast Tomography With Conventional X-Ray Sources", *Med. Phys.*, **41** (2014), 070701.

27) F. A. Vittoria, M. Endrizzi, G. K. Kallon, C. K. Hagen *et al.*: "Multimodal Phase-Based X-Ray Microtomography with Nonmicrofocal Laboratory Sources", *Phys. Rev. Appl.*, **8** (2017), 064009.

28) M. Endrizzi, F. A. Vittoria, L. Rigon, D. Dreossi *et al.*: "X-ray Phase-Contrast Radiography and Tomography with a Multiaperture Analyzer", *Phys. Rev. Lett.*, **118** (2017), 243902.

29) N. Matsunaga, K. Yano, M. Endrizzi and A. Olivo: "Detection of individual sub-pixel features in edge-illumination x-ray phase contrast imaging by means of the dark-field channel", *J. Phys. D: Appl. Phys.*, **53** (2020), 095401.

30) D. Shoukroun, L. Massimi, F. Iacoviello. M, Endrizzi, D. Bate *et al.*: "Enhanced composite plate impact damage detection and characterisation using X-Ray refraction and scattering contrast combined with ultrasonic imaging", *Compos. B.*, **181** (2020), 107579.

松永教仁
Norihito MATSUNAGA
研究開発本部
光技術研究所
Optical Research Laboratory
Research & Development Division

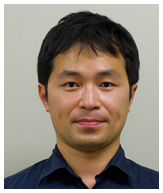

矢野和弘
Kazuhiro YANO
研究開発本部
光技術研究所
Optical Research Laboratory
Research & Development Division

David BATE
Nikon X-Tek Systems Ltd

Marco ENDRIZZI
University College London

Alessandro OLIVO
University College London

バーチャルインターフェログラムを用いたフーリエ変換法の位相解析誤差軽減方法†

鳥羽英光，劉　志強，宇田川里織，藤原直樹，中山　繁，玄間隆志，武田光夫

Virtual interferogram-based method for Fourier transform-based phase analysis

Hidemitsu TOBA, Zhiqiang LIU, Saori UDAGAWA, Naoki FUJIWARA,
Shigeru NAKAYAMA, Takeshi GEMMA and Mitsuo TAKEDA

干渉計などの縞解析のためのフーリエ変換法（FTM）で現れる位相誤差を低減するための新しい手法を提案する．レンズ面の円形の有効径を全面で一括測定する等の場合には，干渉縞のある領域の端で強度分布が不連続になるために，FTM 法で得られた位相にリップル誤差が発生する．このリップル状の位相誤差は，Zernike 多項式のような低次多項式でモデル化できるような位相，振幅，バックグラウンドの緩やかな形状が影響している．このことから，近似的な位相・振幅・バックグラウンドを持つ縞モデルから作成したバーチャルインターフェログラムを解析することでリップル誤差を推定し補正することができる．このバーチャルインターフェログラムを用いた方法は，初期の大まかな推測から始めて，反復的なアルゴリズムによって逐次的に改良することもできる．提案した手法によって効果的にリップル誤差を軽減できることをシミュレーションと実験で確かめた．

We propose a novel method to reduce artefactual phase errors inherent to the Fourier transform method (FTM) in fringe analysis. If the effective diameter of the circular lens is measured over the entire surface, the fringe image data exhibits a discontinuous intensity distribution at the edge of the effective diameter. Phases obtained from such fringes via FTM have been observed to exhibit ripple errors at the boundaries of fringe patterns. Further, such artefactual phase errors have been found to possess certain systematic relations to the form of the phase, amplitude, and background intensity distributions, which can be modeled using low-order polynomials, such as Zernike polynomials, in practical scenarios. Based on this observation, we estimate systematic ripple errors in FTM-generated phases by analyzing a virtual interferogram that is numerically created for fringe models with known phase, amplitude, and background intensity distributions. Beginning with a rough initial estimate, the virtual interferogram is sequentially improved via an iterative algorithm, and the estimated errors are finally subtracted from the experimental data. Moreover, we present the results of simulations and experiments that demonstrate the validity of the proposed method.

Key words　縞解析，干渉計，シングルショット計測
fringe analysis, interferometer, single-shot measurement

1 はじめに

高精度の光学系で用いられるレンズの面形状の評価やレンズの結像性能を決める波面収差の評価にはよく干渉計が用いられる．干渉計で得らえる干渉縞から位相情報を抽出することで精度の高いレンズ面形状分布，波面の情報が得られる．干渉縞から位相を計算する方法はいろいろと提案されているが，中でも位相シフト法（PSI）[1] とフーリエ変換法（FTM）[2] の 2 つがとてもよく知られておりいろいろなところで使われている．PSI で位相を求めるためには正確に位相シフトした縞画像が少なくとも 3 つ必要である．しかしながら，振動などの外乱がある環境での測定では位相シフト量が乱されるため誤差が生じる．また，複数枚の画像を取得する間に静止していることが仮定されているため，運動する物体の測定には適していない．これらの欠点を克服するために，複数台のカメラを用いたり，画素化された偏光カメラを用いたりして，一度に複数ステップに相当する縞画像を取得する工夫がある[3]．

一方，FTM は縞画像 1 つで位相の計算ができるため，動いているものの測定や，振動の大きい環境での測定に適している．しかし FTM で得られる位相分布にはリップル上の大きい誤差が計算領域の端に存在するため，細かい形状

† 本稿は引用文献 8）を基に日本語化し，シミュレーション結果に Gerchberg-Saxton 反復法との比較を加えたものである．

を有効径の端まできちんと見たいような高精度な測定には向かない．これはフーリエ空間でフィルタリング操作を行うFTM特有の誤差である．レンズ面等，計測で得られた干渉縞は多くの場合円形などの限られた領域であるため，これをフーリエ変換した時の空間キャリア周波数に含まれる必要な情報の一部が，FTMで使用するスペクトルを抽出するためのフィルタウィンドウからはみ出してしまうことになる．このスペクトルがはみ出すことが，実空間上の縞がある領域のエッジ付近で位相分布にリップル誤差を生じる原因である．これらの誤差を減らす手法としてこれまで提案されている方法としては，ハニング窓関数等を適用する方法[2)4)]，縞のない領域をダミーの縞で埋める方法[5)]，それにGerchberg-Saxtonの反復法を用いる方法[6)]がある．ハニング窓やハミング窓のような典型的なベル型の窓関数を用いることでリップル誤差を低減することができる．ただし，これらの関数は伝達関数と等価であり，情報の一部を減衰させる．したがって，高い空間周波数の情報が重要な測定の場合には利用すべきではない．一方，縞のない領域をダミーの縞で埋める方法は，干渉縞のバックグラウンド（DC成分）と干渉縞のエンベロープがほぼ一定であることが必要である．そこで我々はバーチャルインターフェログラム法（VIM）と呼ばれる別の手法を提案する．この手法は矩形窓を使用するため，フィルタ窓内の情報を損なう事がなく，また，DC成分と干渉縞のエンベロープを事前に一定にする必要がない．

2 フーリエ変換法

先ず，ここで通常のFTMの計算方法を復習する．

大きなチルトの存在する干渉縞分布は

$$\begin{aligned} I(x,y) &= a(x,y) + b(x,y)\cos\left[\phi(x,y)\right] \\ \phi(x,y) &= 2\pi\left(f_x x + f_y y\right) + \phi_0(x,y) \end{aligned} \tag{1}$$

と書ける．ここで我々が求めたいものは$\phi_0(x,y)$の分布である．また，$a(x,y)$，$b(x,y)$は強度分布のDC成分と干渉縞のエンベロープで緩やかな成分の関数である．(f_x,f_y)はキャリア周波数と呼ばれ，FTMで解析しやすいように干渉縞の測定光と参照光の波面の相対チルト量で調整できる量である．式（1）は

$$\begin{aligned} I(x,y) = a(x,y) &+ \tfrac{b(x,y)}{2}\exp\left[i\phi(x,y)\right] \\ &+ \tfrac{b(x,y)}{2}\exp\left[-i\phi(x,y)\right] \end{aligned}$$

と変形できる．この干渉縞をフーリエ変換するとそれぞれの項が，0次，+1次，および−1次の3つのスペクトル成分として分離して現れる．第一項が0次のスペクトルとなり原点の周辺に，第二項が+1次のスペクトルとなりキャリア周波数(f_x,f_y)の周辺に存在する．

以下，0次を抜き出すフィルタ演算を$\mathcal{F}_0$，+1次を抜き出すフィルタ演算を$\mathcal{F}_{+1}$と書くことにする．これらのフィルタ操作は，ある干渉縞に対してフーリエ変換，矩形窓によって0次若しくは+1次のスペクトル成分を抽出，逆フーリエ変換という3つの演算をまとめたものである．このフィルタ$\mathcal{F}_{+1}$を用いると位相を

$$\phi_{\mathrm{FTM}}(x,y) = \arctan\left[\frac{\mathrm{Im}\left[\mathcal{F}_{+1}\left[I(x,y)\right]\right]}{\mathrm{Re}\left[\mathcal{F}_{+1}\left[I(x,y)\right]\right]}\right] \tag{2}$$

と計算できることが分かる．これがFTMで求められる位相である．

通常のFTMでは特に計算する必要はないが，DC成分$a(x,y)$と干渉縞のエンベロープ$b(x,y)$も計算できて

$$\begin{aligned} a_{\mathrm{FTM}}(x,y) &= \mathrm{Re}\left[\mathcal{F}_0\left[I(x,y)\right]\right] \\ b_{\mathrm{FTM}}(x,y) &= 2\left|\mathcal{F}_{+1}\left[I(x,y)\right]\right| \end{aligned} \tag{3}$$

である．

3 バーチャルインターフェログラム法

バーチャルインターフェログラム法のアイディアを述べる．干渉計で測定される光学レンズの表面は通常滑らかで緩やかな形状（多項式で表した時に低次成分で表せる形状）をしている．この形状がエッジでは不連続になるためにリップル誤差が発生することに注目する．ここで，式（1）の$a(x,y)$，$b(x,y)$と$\phi(x,y)$の低次成分の分布がおおよそ分かっていると仮定する．その近似値を縞モデルのパラメータとして使用して仮想的な干渉縞（バーチャルインターフェログラム）を作成する．バーチャルインターフェログラムは

$$\begin{aligned} I_{\mathrm{VIRTUAL}}(x,y) = a_{\mathrm{MODEL}}(x,y) \\ + b_{\mathrm{MODEL}}(x,y)\cos\left(\phi_{\mathrm{MODEL}}(x,y)\right) \end{aligned} \tag{4}$$

と書ける．この式（4）は式（1）と同じ形をしており，式（2）（3）の計算と同様にDC成分，エンベロープ，位相を求めることができる．

$$\begin{aligned} a_{\mathrm{FTM\text{-}MODEL}}(x,y) &= \mathrm{Re}\left[\mathcal{F}_0\left[I_{\mathrm{VIRTUAL}}(x,y)\right]\right] \\ b_{\mathrm{FTM\text{-}MODEL}}(x,y) &= 2\left|\mathcal{F}_{+1}\left[I_{\mathrm{VIRTUAL}}(x,y)\right]\right| \\ \phi_{\mathrm{FTM\text{-}MODEL}}(x,y) &= \arctan\left[\frac{\mathrm{Im}\left[\mathcal{F}_{+1}\left[I_{\mathrm{VIRTUAL}}(x,y)\right]\right]}{\mathrm{Re}\left[\mathcal{F}_{+1}\left[I_{\mathrm{VIRTUAL}}(x,y)\right]\right]}\right] \end{aligned} \tag{5}$$

いま，モデル$a_{\mathrm{MODEL}}(x,y)$，$b_{\mathrm{MODEL}}(x,y)$と$\phi_{\mathrm{MODEL}}(x,y)$の分布が分かっているので，式（5）のFTMの計算で生じる誤差$\Delta a(x,y)$，$\Delta b(x,y)$と$\Delta\phi(x,y)$を次のように計算できる

$$\begin{aligned} \Delta a(x,y) &= a_{\mathrm{FTM\text{-}MODEL}}(x,y) - a_{\mathrm{MODEL}}(x,y) \\ \Delta b(x,y) &= b_{\mathrm{FTM\text{-}MODEL}}(x,y) - b_{\mathrm{MODEL}}(x,y) \\ \Delta\phi(x,y) &= \phi_{\mathrm{FTM\text{-}MODEL}}(x,y) - \phi_{\mathrm{MODEL}}(x,y) \end{aligned} \tag{6}$$

これが実際の誤差を近似しているので，実際の縞画像のFTM計算結果（2），（3）からこのバーチャルインターフェログラムのFTM計算から得られた誤差（6）を引くことで，

リップル誤差を補正できる．式で書くと

$$\begin{aligned} a_{\mathrm{CORR}}(x,y) &= a_{\mathrm{FTM}}(x,y) - \Delta a(x,y) \\ b_{\mathrm{CORR}}(x,y) &= b_{\mathrm{FTM}}(x,y) - \Delta b(x,y) \\ \phi_{\mathrm{CORR}}(x,y) &= \phi_{\mathrm{FTM}}(x,y) - \Delta\phi(x,y) \end{aligned} \tag{7}$$

が補正された測定結果である．

それでは式（4）で用いる低次成分の $a_{\mathrm{MODEL}}(x,y)$, $b_{\mathrm{MODEL}}(x,y)$と$\phi_{\mathrm{MODEL}}(x,y)$ をどのように推測できるだろうか？

色々な方法が考えられると思うが，従来の FTM の結果を利用する方法を考える．従来の FTM で得られた実験結果（式（2），（3））は，取り除きたいリップル誤差が存在するために直接利用することはできない．しかしながら被検面の形状や干渉計で使用する測定光，参照光の光量分布が滑らかであるとい事前知識を利用すれば，一度従来の FTM で計算した結果を低次の多項式でフィッティングし，そのフィッティング成分を式（4）の $a_{MODEL}(x,y)$，$b_{MODEL}(x,y)$ と$\phi_{MODEL}(x,y)$ として使うことができる．レンズ等の計測では有効径が円であるためフィッティング関数として Zernike 多項式[7] が使える．ここで，式（7）計算後に得られる結果は Zernike 多項式で表せられる量でないことを指摘しておく．バーチャルインターフェログラム法では，$\mathcal{F}_{+1}$ で使用した矩形窓内全ての空間周波数を減衰させずに用いているため，フィッティングされた Zernike で表現される形状よりも細かい成分のプロファイルを取得できる．

以上がバーチャルインターフェログラム法のアイディアである．

このバーチャルインターフェログラム法の計算結果を再度 Zernike 多項式でフィッティングし，これを新たなモデルとして利用すると，より良いバーチャルインターフェログラムのモデル $a_{MODEL}(x,y)$，$b_{MODEL}(x,y)$ と$\phi_{MODEL}(x,y)$ を与えることになるだろう．そこでバーチャルインターフェログラムのモデルを更新して繰り返し計算するとにより，よりリップル誤差を軽減することができることが期待できる．このように繰り返しモデルを更新する方法を反復バーチャルインターフェログラム法（反復 VIM）と呼ぶことにする．具体的な手順は

1. 干渉計で取得した干渉縞画像 $I(x,y)$ の干渉縞のない領域をゼロ等の定数で埋める．
2. $I(x,y)$ から通常の FTM（式（2）-（3））を計算して $a_{\mathrm{FTM}}(x,y)$，$b_{\mathrm{FTM}}(x,y)$ と$\phi_{\mathrm{FTM}}(x,y)$ を求める．
3. 初回は $a_{\mathrm{FTM}}(x,y)$，$b_{\mathrm{FTM}}(x,y)$ と $\phi_{\mathrm{FTM}}(x,y)$ を，２ループ目以降はステップ７で計算した $a_{\mathrm{CORR}}(x,y)$，$b_{\mathrm{CORR}}(x,y)$ と $\phi_{\mathrm{CORR}}(x,y)$ を Zernike 多項式でフィッティングし，そのフィッティング成分を $a_{\mathrm{MODEL}}(x,y)$，$b_{\mathrm{MODEL}}(x,y)$ と$\phi_{\mathrm{MODEL}}(x,y)$ とする．
4. 式（4）のようにバーチャルインターフェログラムを作成する．
5. $I_{\mathrm{VIRTUAL}}(x,y)$ から式（5）を用いて $a_{\mathrm{FTM\text{-}MODEL}}(x,y)$, $b_{\mathrm{FTM\text{-}MODEL}}(x,y)$ と $\phi_{\mathrm{FTM\text{-}MODEL}}(x,y)$ を計算する．ここで使うフィルタ $\mathcal{F}_0$ および $\mathcal{F}_{+1}$ はステップ２で使用したものと同じものを用いる．
6. 式（6）を用いて FTM 計算をバーチャルインターフェログラムに対して行った際に発生する誤差を計算する．
7. 式（7）のようにステップ６で計算した誤差をステップ２で計算した結果から差し引いて誤差補正を行う．

$\phi_{\mathrm{CORR}}(x,y)$ が収束するまでステップ3-7を繰り返す．収束した $\phi_{\mathrm{CORR}}(x,y)$ が我々の求めたい位相分布となる．反復 VIM のアルゴリズムのフローを Fig. 1 に示す．

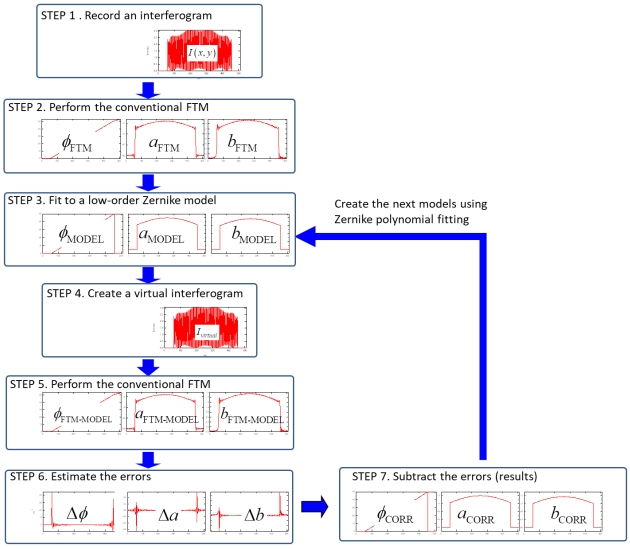

Fig. 1　反復 VIM のアルゴリズム

4 シミュレーション

シミュレーションにより反復 VIM の誤差と従来の FTM の誤差とを比較する．512×512の画像の中心に直径460 pix の円形領域に干渉縞があるとする．このシミュレーションで使用する干渉縞を式で表すと

$$\begin{aligned} I(x,y) &= a(x,y) \\ &\quad + b(x,y)\cos\left(2\pi\left(f_{cx}x + f_{cy}y\right) + \phi_M(x,y)\right) \end{aligned}$$

である．ここで，座標 x, y は，円領域の端で 1 となるように正規化する．DC 成分と干渉縞のエンベロープをそれぞれ

$$\begin{aligned} a(x,y) &= \exp\left[-\left(x^2+y^2\right)/0.9^2\right] \\ b(x,y) &= 0.5\exp\left[-\left(x^2+y^2\right)/0.9^2\right] \end{aligned}$$

とする．また，位相分布 $\phi_M(x,y)$ はニコンで所有する実際の干渉計で測定されたあるレンズ面のデータを使用した（この位相分布 ϕ_M の RMS は 0.0068 rad. Fig. 2 (a) を参照）．FTM を用いた位相計算にはキャリア縞が必要であるため，傾斜した位相を $\phi_M(x,y)$ に追加しており，そのキャリア周波数は $f_{cx} = f_{cy} = 1/8\,pix^{-1}$ とした．

FTM 計算で 0 次，+1 次を切り出すフィルタは矩形窓で，

$$w(f_x,f_y)=\begin{cases}1 & \sqrt{(f_x-f_{0x})^2+(f_y-f_{0y})^2}<f_r \\ 0 & \text{otherwise}\end{cases} \quad (8)$$

とした．ここで (f_x,f_y) は空間周波数，(f_{0x},f_{0y}) と f_r はそれぞれフィルタの中心の空間周波数とその半径で＋1 次および 0 次のフィルタの半径は $1/16pix^{-1}$ とした．フィッティングの時に使用する Zernike 多項式は $\{Z_n^l(\rho,\theta)\,|\,n\le 8, l\le n,(n-l)\text{ is even}\}$ で表されるものを使う．（ρ と θ は極座標のパラメータで $x=\rho\cos\theta$，$y=\rho\sin\theta$ と変換される）．

結果を Fig. 2 と Fig. 3 に示す．Fig. 3 は Fig. 2 の断面．Fig. 3 には従来技術である Gerchberg-Saxton 反復法の結果もプロットしている．従来の FTM の結果に現れている大きなリップル状の誤差は，Gerchberg-Saxton 反復法と反復 VIM の結果には見られない．Gerchberg-Saxton 反復法と同様に反復インターフェログラム法でリップル誤差を軽減することができていることを示している．FTM で得られる位相分布は，+1 次の窓でローパスフィルター処理されたデータであるため，与えた位相分布よりボケた分布になる．そこで，Fig. 3 では位相解析の結果を与えた位相 $\phi_M(x,y)$ に $1/16pix^{-1}$ のローパスをかけたものと比較している．ローパスフィルターを掛けた $\phi_M(x,y)$ の RMS は 0.0035 rad. である．

さまざまな測定条件下での反復 VIM の収束する様子を Fig. 4 にプロットした．横軸は反復計算回数，縦軸はその時の誤差 RMS で，従来の FTM の結果が 0 回目の値と一致する．Fig. 4（a）では与える位相 $\phi_0(x,y)$ の大きさの依存性を示す．$\phi_M(x,y)$ にいくつかの比例係数をかけることで $\phi_0(x,y)$ の大きさを変化させた．Fig. 4（b）は，細かい形状を含む $\phi_M(x,y)$ の量を一定にして，それにモデル関数 $\{Z_n^l(\rho,\theta)\,|\,n\le 8, l\le n,(n-l)\text{is even}\}$ に含まれる緩やかな成分 $Z_5^3(\rho,\theta)=\sqrt{12}(5\rho^5-4\rho^3)\cos 3\theta$ の 0 ～ 2 の比例倍を足し合わせた位相を $\phi_0(x,y)$ として与えたときの結果である．全ての場合に於いて繰り返し回数20回以内に収束している．反復 VIM が，数百回以上の繰り返しが必要な Gerchberg-Saxton 反復法に比べてとても少ない回数で収束するアルゴリズムであることが分かる．Fig. 4（a）をみると，$\phi_0(x,y)=\phi_M(x,y)$ の場合，反復 VIM を用いることで，誤差 RMS を従来の FTM の場合に比べて約1/100まですることができており，$\phi_0(x,y)=0$ の場合は更に，1/6000まで小さくすることができている．

Fig. 4（a）をみると，反復計算で収束した後の誤差が $\phi_M(x,y)$ の量によって変化しているが，Fig. 4（b）をみると，$Z_5^3(\rho,\theta)$ の量に関係なく一定の誤差に収束している．$\phi_M(x,y)$ にはモデル関数 $\{Z_n^l(\rho,\theta)\,|\,n\le 8, l\le n,(n-l)\text{is even}\}$ で表現できない成分が入っていることを考えると，位相 $\phi_0(x,y)$ の中の反復 VIM の計算で使用するモデル関数

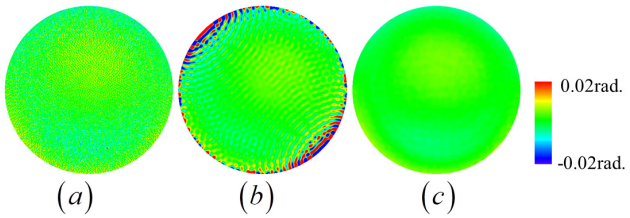

Fig. 2　シミュレーション結果（a）与えた位相分布 $\phi_0(x,y)=\phi_M(x,y)$．（b）従来の FTM での位相復元結果．面内 RMS は 0.041 rad.（c）反復バーチャルインターフェログラム法での位相復元結果．面内 RMS は 0.0035 rad.

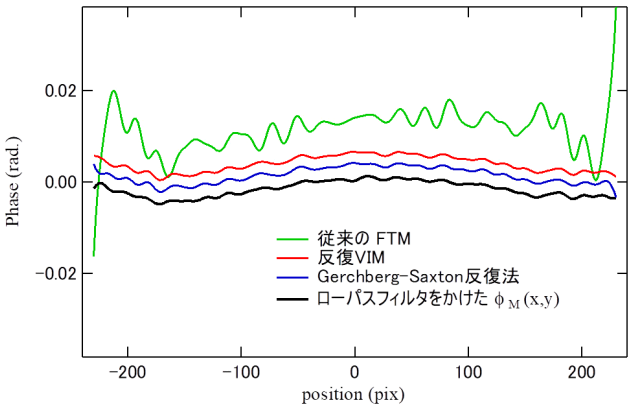

Fig. 3　Fig. 2 の断面．Gerchberg-Saxton 反復法の結果も加えている．

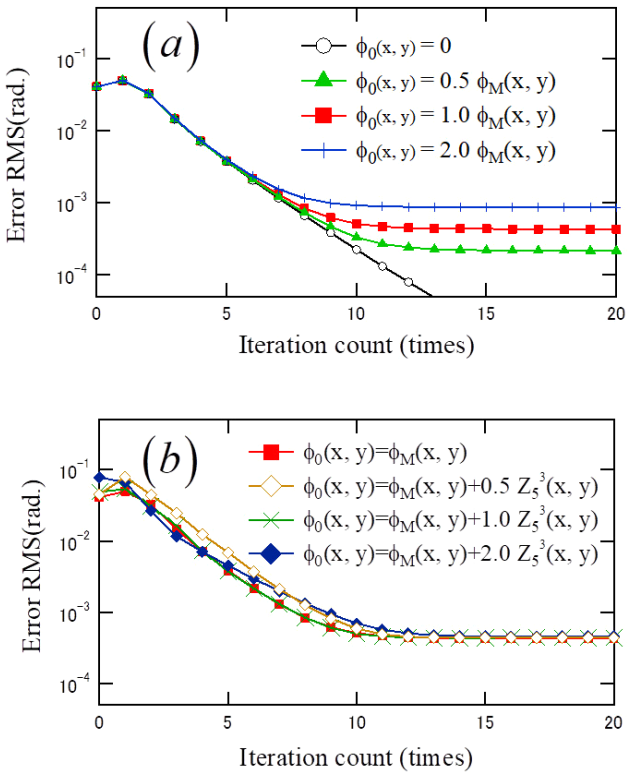

Fig. 4　与える位相 $\phi_0(x,y)$ をいろいろ変えたときの反復 VIM の収束する様子．（a）$\phi_M(x,y)$ に 0 ～ 2 を掛けたものを $\phi_0(x,y)$ とした時の結果．与えた位相の RMS は 0 から 2×0.0068 rad. である．（b）$\phi_0(x,y)$ として $\phi_M(x,y)$ に，0 ～ 2 の比例係数を掛けた $Z_5^3(\rho,\theta)$ を加えた結果．

$\left\{Z_n^l(\rho,\theta)\,|\,n\le 8, l\le n, (n-l)\text{is even}\right\}$ で表せない成分が反復計算後の誤差に効くと考えられる．

5 実　験

社内のフィゾー干渉計で平面の表面を計測した際に取得した縞画像を用いて，実験的にバーチャルインターフェログラム法の有効性を確認する．用いるデータは直径 460 pix の円形領域に干渉縞が存在する512×512の 2 次元データで，被検面に対してフィゾー面を傾けることによりキャリア周波数 f_x と f_y が約 $1/4 pix^{-1}$ となるようにチルト縞を調整してある．この時の干渉縞は概ね斜め45度の右下がりの縞になっている．FTM の＋1 次と 0 次のパスウィンドウ $w(f_x,f_y)$（式（8）を参照）の半径は $1/6 pix^{-1}$．反復アルゴリズムのステップ 2 でフィッティングに使用する Zernike 多項式はシミュレーションの時と同じく $\left\{Z_n^l(\rho,\theta)\,|\,n\le 8, l\le n, (n-l)\text{ is even}\right\}$ を用いる．

この反復 VIM の結果を Fig. 5-7 に示す．1 枚の縞画像から反復 VIM によって求めた位相分布が Fig. 5（a）である．約 0.1 rad. の大きさの緩やかな成分が存在していることが分かる．実験の場合，被検物の形状の本当の正解が分からないため本当の誤差を求めることはできない．が，ここでは位相シフト法（PSI）によって取得された位相を基準に誤差を見積もることにする（Fig. 5（b），（c））．細かい構造が良く見えるように位相分布の X-slope が Fig. 6 である．グレースケールで表示してある．Fig. 5（b），Fig. 6（b），Fig. 7 を見ると，予想どおり従来の FTM の結果にはエッジにリップル状の誤差が存在していることが確認できる．一方，反復 VIM の結果ではこのリップル誤差が見えない（Fig. 5（c），Fig. 6（c））．反復 VIM の結果では細かい凸凹の形状を計測しつつエッジでのリップル誤差を抑えることができている．

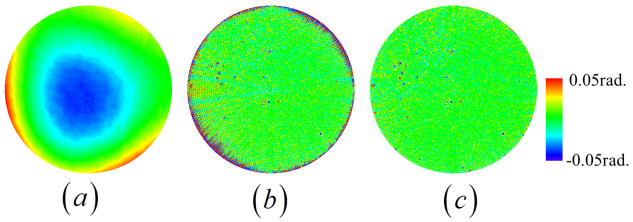

Fig. 5　実験結果．（a）反復 VIM で計算した位相（RMS＝0.30 rad.）．（b）従来の FTM の結果と PSI の結果の差分（RMS＝0.036 rad.）．（c）反復 VIM の結果と PSI の結果の差（RMS＝0.006 rad.）．

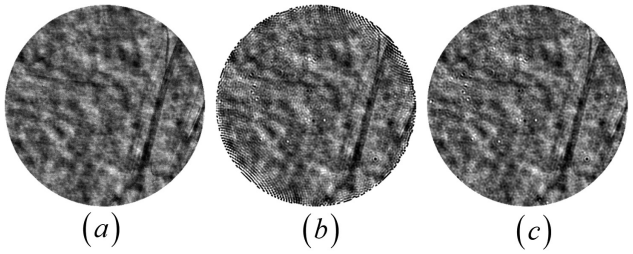

Fig. 6　Fig. 5 の位相分布の x-slope．（a）PSI（b）従来の FTM（c）反復 VIM．

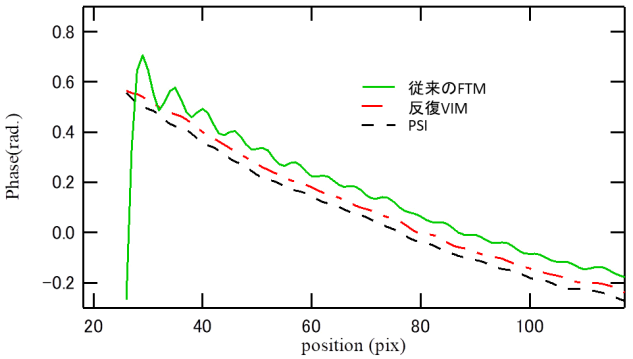

Fig. 7　実験の干渉縞を解析した位相分布のエッジ部分の断面．

6 まとめ

従来のフーリエ変換法の計算過程で現れる固有の誤差を，バーチャルインターフェログラムを用いることで軽減する VIM という手法を提案した．シミュレーションと実験により，VIM は従来の FTM に固有のリップル誤差を低減するための効果的な方法であり，フィッティング成分では表すことができない詳細な形状情報をリップル誤差なしに取得できることを示した．この手法により，位相シフト干渉法での測定が難しい振動や乱気流計測での応用が期待できる．

引　用　文　献

1）K. Creath: “Phase-measurement interferometry techniques”, in *Progress in Optics*, XXVI, E. Wolf, Ed., pp. 349-393, (Elsevier Science Publishers, Amsterdam, 1988).

2）M. Takeda, H. Ina and S. Kobayashi: “Fourier-transform method of fringe-pattern analysis for computer-based topography and interferometry”, *J. Opt. Soc. Am.*, **72** (1982), 156-160.

3）H. Schreiber and J. H. Bruning: “Phase shifting interferometry”, in *Optical Shop Testing*, D. Malacara, Ed., 3rd ed., pp. 564-568, (Wiley-Interscience, Hoboken, New Jersey, 2007).

4）D. J. Bone, H.-A. Bachor and R. J. Sandeman: “Fringe-pattern analysis using a 2-D Fourier transform”, *Appl. Opt.*, **25** (1986), 1653-1660.

5）M. Kujawinska, A. Spik and J. Wojciak: “Fringe pattern analysis using Fourier transform techniques”, *Proc. SPIE* 1121 (1989), 130-135.

6）C. Roddier and F. Roddier: “Interferogram analysis using Fourier transform techniques”, *Appl. Opt.*, **26** (1987), 1668-1673.

7）V. N. Mahajan: “Zernike polynomials and wavefront fitting”, in *Optical Shop Testing*, D. Malacara, Ed., 3rd ed., pp. 498-

546, (Wiley-Interscience, Hoboken, New Jersey, 2007).
8) H. Toba, Z. Liu, S. Udagawa, N. Fujiwara, S. Nakayama, T. Gemma and M. Takeda: "Phase analysis error reduction in the Fourier transform method using a virtual interferogram", *Optical Engineering*, **58** (2019), 084103.

鳥羽英光
Hidemitsu TOBA
研究開発本部
光技術研究所
Optical Research Laboratory
Research & Development Division

劉　志強
Zhiqiang LIU
研究開発本部
光技術研究所
Optical Research Laboratory
Research & Development Division

宇田川里織
Saori UDAGAWA
研究開発本部
光技術研究所
Optical Research Laboratory
Research & Development Division

藤原直樹
Naoki FUJIWARA
生産本部
設備技術開発部
Equipment Engineering Department
Production Technology Division

中山　繁
Shigeru NAKAYAMA
研究開発本部
光技術研究所
Optical Research Laboratory
Research & Development Division

玄間隆志
Takeshi GEMMA
光学本部
開発戦略部
Strategic Technology Development Department
Optical Engineering Division

武田光夫
Mitsuo TAKEDA
宇都宮大学
Utsunomiya University

支配方程式の発見とドメイン知識を持つ学習システムに向けて

大坪洋介，中島伸一

Discovery of Governing Equations and Learning Systems with Domain Knowledge†

Yosuke OTSUBO and Shinichi NAKAJIMA

機械学習は近年様々な分野で成功を収めてきている．しかし一般に，従来のデータ駆動型の機械学習は次のような課題がある．1）解釈性が乏しい，2）不十分なデータやラベルに対して十分な精度がでない．本稿ではまず，解釈可能な予測モデルを構成するため，時系列データから常微分方程式（ODE）を発見する問題に焦点を当て，スパース推定とカーネルリッジ回帰を用いた新しいアルゴリズムを提案する．ODE はこれまで専門家の深い洞察によってモデル化されてきたが，データ駆動で ODE の関数形を発見することは，解釈性を備えた予測モデルを学習するという観点から，物理，化学，生物分野などの様々な科学分野において価値がある．さらに上記 1）と 2）の課題を解決するため，近年提案されたドメイン知識を活用した機械学習のフレイムワークである Informed Machine Leaning について簡単に紹介し，ものづくり企業の立場から機械学習に活用できる知識を整理する．このような試みは，解釈性が高く，不十分なデータについても対応可能な機械学習システムの開発に役立つと考えられる．

Machine learning has been great successful in many areas in recent years. However, in general, the conventional data driven approaches in machine learning may have limitations for the following senses: 1) Lack of interpretability, 2) Low accuracy in insufficient data and annotations. To develop predictive model with rich interpretabilities, we focus on ordinary differential equation (ODE) discovery problem and propose a novel algorithm using kernel ridge regression with sparsity inducing regularizer. The ODEs have been modeled by domain experts based on theoretical deduction and empirical observations. So, automatic discovery of ODEs through data-driven is of great significance in various scientific fields, such as those of physics, chemistry, and biology in terms of interpretable predictions. Furthermore, to remedy the issues 1) and 2), we shortly introduce Informed Machine Learning, a machine learning pipeline framework with prior knowledge, and provide useful knowledge for further development of the learning system from the viewpoint of manufacturing companies. Such an attempt will help us to develop the interpretable learning systems that can deal with insufficient data.

Key words 常微分方程式，スパース推定，再生核ヒルベルト空間，ドメイン知識，知識が導入された機械学習
ordinary differential equations, sparse inference, reproducing kernel space, domain knowledge, Informed Machine Learning

1 Introduction

Many methodologies in machine learning make some inference by using data efficiently. In general, the conventional data driven approaches may have limitations for the following senses.

I. Lack of interpretability. If the machine learning techniques work well, interpretation and explanation are often required for the resultant algorithms and models. Understanding the natural phenomena in science, particularly, can be more important than making accurate predictions. For example, during anomaly detection in manufacturing processes, it is important to interpret the results and suggest next action for engineers.

II. Low accuracy in insufficient data and annotations. We must deal with the lack of enough data or their labels. For example, an adequate amount of customer data cannot be obtained owing to confidentiality and privacy issues or limitations related to the biological and medical experimental environment. Despite the advanced knowledge for annotations, it is difficult to obtain enough labeled datasets.

To remedy these issues, we mainly focus on 1) Ordinary differential equation (ODE) discovery problem for developing predictive model with rich interpretabilities, and shortly

† This article contains a summary of [14]

provide 2) taxonomy of useful prior knowledge for developing further develop the learning systems in manufacturing companies.

1.1. ODE discovery problem

Various types of nonlinear dynamical systems have been developed for characterizing the natural phenomena in science and engineering. For example, Newtonian dynamics, i.e., Newton's second law describes the dynamics of particles, and enzyme kinetics provides insights into the catalytic mechanisms of enzymes in the biochemical context. Such dynamics are often described as nonlinear ODE in the following form:

$$\dot{\boldsymbol{x}} = \frac{d\boldsymbol{x}}{dt} = \boldsymbol{f}(\boldsymbol{x};\boldsymbol{\theta}), \tag{1}$$

where $\boldsymbol{x}$ is the state variable, t is the time, and $\boldsymbol{f}$ is a nonlinear function parameterized by $\boldsymbol{\theta}$. Historically, many important ODEs, e.g., Newton' law, Maxwell equations, enzyme kinetics, were discovered by domain experts based on theoretical deduction and empirical observations.

A question we try to answer in this paper is whether such discovery process can be automated, i.e., we try to find ODEs that the observed time-series data satisfy, automatically by training machine learning models*1. To accomplish this, the following two issues need to be addressed: parameter specification and inference. The former, known as the ODE parameter inference problem, corresponds to the determination of the internal parameter $\boldsymbol{\theta}$, and the latter, known as the ODE discovery problem, corresponds to the identification of the functional form of $\boldsymbol{f}$ in Eq. (1).

We tackle the ODE discovery problem in the first half of this article. In practice, most of the possible applications include the identification of the dynamics of biopathways, which are usually described as ODEs based on their biochemical reactions[1]. Even though various computational models of regulatory and metabolic networks have been proposed by domain experts (e.g.[2]), determining the essential connectivity and structures of these dynamics remains an extremely challenging task. In computer aided engineering (CAE) processes, the dynamics of the flow and temperature on materials need to be mathematically modeled to design and construct mechanical architectures. Thus, inferring the structures and nonlinear dynamics in large systems is a challenging problem.

Additionally, if the predictive models are trained in the form of an ODE function, they can provide rich interpretabilities to domain experts. That is, the terms in the ODEs can be considered relevant in a physical or chemical context (e.g., friction strength or reaction intensity). Therefore, our study may be closely related to the estimation of interpretable predictive models.

1.2. Taxonomy of useful knowledge

To deal with the subjects mentioned in 1) and 2), several works incorporated prior knowledge into machine learning processes[3)~10)]. For example, knowledge gained from a scientific or mechanical perspective can help us to improve the learning accuracy and interpretability. As concrete examples, physics guided neural networks, where a penalty term inspired by scientific knowledge is added to the loss function as regularizer, provide more accurate results than purely data driven approaches[9]. A recent study introduced a systematic taxonomy of integrating knowledge into learning systems, called *Informed Machine Learning*[11]. The study provides definitions of the prior knowledge, its representation, and integration into the machine learning pipeline. In this study, we introduce new useful domain knowledge to further develop the learning system in the context of manufacturing. Such an attempt will help us to develop useful and efficient learning systems for manufacturing companies.

2 ODE discovery in RKHS

In this section, we introduce the ODE discovery problem, our approach, and report on experimental results.

2.1. Problem definition and related works

Consider N time points $t_1 < t_2 \cdots < t_N$ and their corresponding state variables

$$\boldsymbol{X} = \left[\boldsymbol{x}(t_1),\ldots,\boldsymbol{x}(t_N)\right]^T = \left[\boldsymbol{x}_1,\ldots,\boldsymbol{x}_N\right]^T \tag{2}$$

where $\boldsymbol{x}_s \in \mathbb{R}^d$ represents the states at the s-th time-point. Similarly, the matrix of derivatives can be described as

$$\dot{\boldsymbol{X}} = \left[\dot{\boldsymbol{x}}(t_1),\ldots,\dot{\boldsymbol{x}}(t_N)\right]^T = \left[\dot{\boldsymbol{x}}_1,\ldots,\dot{\boldsymbol{x}}_N\right]^T \tag{3}$$

Our problem includes estimating the functional form of $\boldsymbol{f}$ in Eq. (1) from the data $\boldsymbol{X}$ given by Eq. (2). This can be accomplished using a method in which sparse inference is applied to fit the numerical derivatives of a linear regression model using a large set of possible ODE candidate functions[12)13)]. Such methods are called sparse identification of nonlinear dynamics (SINDy). In SINDy, the library of candidates of the nonlinear functions constructed by their states are set as

*1 Although Eq. (1) involves only the first derivative, it covers any finite degree ODE: for expressing an R-th degree ODE, the state vector $\boldsymbol{x}$ should be augmented by its first to the R-1-th degree derivatives. This procedure adequately set the degree of freedom (i.e., the dimension of the state) of the model.

$$\Theta(\boldsymbol{X})=\left[\mathbf{1}\ \boldsymbol{X}\ \boldsymbol{X}^2\ \boldsymbol{X}^3\cdots\right], \tag{4}$$

where $\boldsymbol{X}^k$ denotes the matrix containing all possible column vectors obtained from the time series of k-th degree polynomials in the state vector $\boldsymbol{x}$. Note that the dimension D of $\Theta(\boldsymbol{X})$ with k-th polynomial terms in d variables can be computed as ${}_{k+d}C_d$; the possible combination is given by $N_p=\sum_{i=1}^{D}{}_DC_i$.

The ODE with the possible candidate bases can be modeled in the parametric form:

$$\dot{\boldsymbol{X}}=\Theta(\boldsymbol{X})\boldsymbol{B}, \tag{5}$$

where $\boldsymbol{B}=\left[\boldsymbol{\beta}_1,\ldots,\boldsymbol{\beta}_d\right]$ corresponds to the coefficients of the ODE. Let us focus on the l-th column,

$$\dot{\boldsymbol{X}}_l=\Theta(\boldsymbol{X})\boldsymbol{\beta}_l \tag{6}$$

where $\boldsymbol{X}_l=\left[x_l(\mathrm{t}_1),\ldots,x_l(t_N)\right]$. Then, it is evident that if $\beta_{l,s}=0$, the s-th feature is not effective in the l-th state. Thus, the ODE discovery problem in the formulation is reduced to the inference problem where the coefficients of matrix $\boldsymbol{B}$ contain many zero components. The original SINDy algorithm uses the sequential thresholded least squares (see Algorithm 1 in[14]). Lasso also can be employed as an alternative approach to enforce sparsity:

$$\boldsymbol{\beta}_l=\arg\min_{\boldsymbol{\beta}_l}\left\|\dot{\boldsymbol{X}}_l-\Theta(\boldsymbol{X})\boldsymbol{\beta}_l\right\|_2^2+\lambda\left\|\boldsymbol{\beta}_l\right\|_1,\forall l, \tag{7}$$

where λ denotes the strength of the L1 regularization term that controls the sparsity. Note that in this approach, the derivatives should be computed numerically from the noisy observations, for which stable implementation is non-trivial. However, the numerical computation of the derivatives is not trivial, and several studies have focused on differentiating the variables precisely. Among many methods proposed, SINDy employed the total variation regularized derivatives (TVDiff)[15] method, a well-known robust method for computing the derivatives from noisy data.

Many methods have been proposed to solve the parameter inference problem for ODE, given the function form of $\boldsymbol{f}$. Gradient matching methods, which are effective for inferring the parameters of ODEs[16)~18)], consist of two steps: a smoothing process to fit the data and an optimization process to minimize some metric between the smooth model and the derivatives predicted from ODEs. A recently proposed gradient matching method defined in the reproducing kernel Hilbert space (RKHS)[18] achieved significant improvements in comparison to alternative probabilistic methods[16)17)]. The method minimizes the loss term for the kernel regression term and the gradient matching term simultaneously:

$$\left\{\boldsymbol{A}^*,\boldsymbol{\theta}^*\right\}=\mathrm{argmin}_{\boldsymbol{A},\boldsymbol{\theta}}\,E(\boldsymbol{A},\boldsymbol{\theta}), \tag{8}$$

$$E(\boldsymbol{A},\boldsymbol{\theta})=\sum_{l=1}^{d}\left\|\boldsymbol{g}_l(\boldsymbol{\alpha}_l)-\boldsymbol{X}_l\right\|_2^2 +\rho\sum_{l=1}^{d}\left\|\dot{\boldsymbol{g}}_l(\boldsymbol{\alpha}_l)-\boldsymbol{f}_l(\boldsymbol{g}(\boldsymbol{A});\boldsymbol{\theta})\right\|_2^2, \tag{9}$$

where kernel regression can be expressed as

$$\boldsymbol{g}_l(t;\boldsymbol{\alpha}_l)=\textstyle\sum_{i=1}^{N}\boldsymbol{\alpha}_{l,i}k(t,t_i)=\boldsymbol{\alpha}_l^T\boldsymbol{k}_l(t), \tag{10}$$

and

$$\dot{\boldsymbol{g}}_l(t;\boldsymbol{\alpha}_l)=\boldsymbol{\alpha}_l^T\dot{\boldsymbol{k}}_l(t). \tag{11}$$

Here, $\boldsymbol{\alpha}_l=\left[\alpha_{l,1},\ldots,\alpha_{1,N}\right]^T$ denotes the vector of the kernel regression coefficients of the l-th variable. The vector of l-th kernels of t, $\boldsymbol{k}_l(t)=\left[k_l(t,t_1),\ldots,k_l(t,t_N)\right]^T$ is specified by the hyperparameter $\boldsymbol{\phi}_l$, i.e., $\boldsymbol{k}_l(t)=\boldsymbol{k}(t;\boldsymbol{\phi}_l)$. The first term in Eq. (9) encourages reconstructed by $g_l(t;\boldsymbol{\alpha})$ of the data $\boldsymbol{X}_l$, while the second term penalizes the inconsistency with the ODE model.

2.2. Proposed method

Inspired by the methods provided in the previous subsection, we propose a hybrid algorithm of sparse inference and a gradient matching algorithm in RKHS.

First, we impose L1 and L2 regularization to Eq. (9):

$$E(\boldsymbol{A},\boldsymbol{B})=\sum_{l=1}^{d}E_l(\boldsymbol{A},\boldsymbol{\beta}_l), \tag{12}$$

$$E_l(\boldsymbol{A},\boldsymbol{\beta}_l)=\left\|\dot{\boldsymbol{g}}_l(\boldsymbol{\alpha}_l)-\Theta(\boldsymbol{A})\boldsymbol{\beta}_l\right\|_2^2+\lambda_1\left\|\boldsymbol{\beta}_l\right\|_1+\lambda_2\boldsymbol{\alpha}_l^T\boldsymbol{K}_l\boldsymbol{\alpha}_l+\rho\left\|\boldsymbol{g}_l(\boldsymbol{\alpha}_l)-\boldsymbol{X}_l\right\|_2^2, \tag{13}$$

where the first term corresponds to the gradient matching term, in which the ODE is represented as a library of candidates of possible bases, $\Theta(\boldsymbol{A})$, similar to SINDy. The interpolant functions $\boldsymbol{g}_l(\boldsymbol{\alpha}_l)$ and $\dot{\boldsymbol{g}}_l(\boldsymbol{\alpha}_l)$ are defined by Eqs. (10) and (11), respectively. $\{\lambda_1,\ \lambda_2,\ \rho\}$ are the regularization parameters and the Gram matrix K_l depends on the kernel parameter $\boldsymbol{\phi}_l$. The minimization of Eq. (12) with respect to $\boldsymbol{A}$ encounters a problem of the complicated dependence of the first term on $\boldsymbol{A}$. Introducing an auxiliary variable $\tilde{\boldsymbol{A}}$ detangles the dependency:

$$\tilde{\boldsymbol{E}}(\boldsymbol{A},\tilde{\boldsymbol{A}},\mathbf{B})=\sum_{l=1}^{d}\boldsymbol{E}_l(\boldsymbol{A},\tilde{\boldsymbol{A}},\boldsymbol{\beta}_l), \tag{14}$$

$$\boldsymbol{E}_l(\boldsymbol{A},\tilde{\boldsymbol{A}},\boldsymbol{\beta}_l)=\left\|\dot{\boldsymbol{g}}_l(\boldsymbol{\alpha}_l)-\Theta(\tilde{\boldsymbol{A}})\boldsymbol{\beta}_l\right\|_2^2+\lambda_1\left\|\boldsymbol{\beta}_l\right\|_1+\lambda_2\boldsymbol{\alpha}_l^T\boldsymbol{K}_l\boldsymbol{\alpha}_l+\rho\left\|\boldsymbol{g}_l(\boldsymbol{\alpha}_l)-\boldsymbol{X}_l\right\|_2^2+\lambda_3\left\|\boldsymbol{\alpha}_l-\tilde{\boldsymbol{\alpha}}_l\right\|_2^2. \tag{15}$$

The last term forces $\tilde{\boldsymbol{A}}$ to match $\boldsymbol{A}$ when λ_3 is sufficiently large, thereby leading to $\boldsymbol{E}_l(\boldsymbol{A},\tilde{\boldsymbol{A}},\boldsymbol{B})=E_l(\boldsymbol{A},\boldsymbol{B})$. We optimize each parameter; Eq. (15) can be analytically minimized with respect to $\boldsymbol{A}$ as follows:

$$\boldsymbol{\alpha}_l^{\mathrm{new}}=\left[\boldsymbol{K}_l^T(\lambda_2\boldsymbol{I}_N+\rho\boldsymbol{K}_l)+\dot{\boldsymbol{K}}_l^T\dot{\boldsymbol{K}}_l+\lambda_3\boldsymbol{I}_N\right]^{-1}\times\left[\rho\boldsymbol{K}_l\boldsymbol{X}_l+\dot{\boldsymbol{K}}_l^T\Theta(\tilde{\boldsymbol{A}})\boldsymbol{\beta}_l+\lambda_3\tilde{\boldsymbol{\alpha}}_l\right]. \tag{16}$$

Then, $\tilde{\boldsymbol{A}}$ is replaced with $\boldsymbol{A}$ for the next iteration, giving $\tilde{\boldsymbol{E}}(\boldsymbol{A}^{\mathrm{new}},\boldsymbol{A}^{\mathrm{new}},\boldsymbol{B})$. Minimization with respect to $\boldsymbol{B}$ can be per-

formed by the standard-lasso algorithm, such as coordinate descent, least angle regression, or alternating direction method of multipliers[19]. It is known that L1 regularizer tends to give a significant bias to the LASSO estimator. To remove the bias, we reapply the least squares method for the non-zero components $\Omega_l' = \{i \mid \beta_l \neq 0\}$ as the final step.

$$\beta_l = \left(\Theta'^T \Theta'\right)^{-1} \Theta' \boldsymbol{K}_l \boldsymbol{\alpha}_l, \tag{17}$$

where $\Theta' = \Theta_{:,\Omega_l'}$ and $\beta_l = \beta_{l,\Omega_l'}$. The hyperparameters $\boldsymbol{h} = \{\lambda, \Phi\}$, where $\lambda = \{\lambda_1, \lambda_2, \lambda_3, \rho\}$ and $\Phi = \{\phi_1, \ldots, \phi_d\}$, which correspond to the regularization and kernel parameters, respectively, are determined in preliminary experiment.

2.3. Numerical experimental settings

Baseline methods

To compare the algorithm performances for the ODE discovery problem, we selected the following methods as baselines.

· TVSINDy[12]: the sequential thresholded least-squares method for selecting variables with the total variation method for numerical differentiation.

· TVLasso: the lasso for selecting variables with the total variation method for numerical differentiation.

· RKHS-Lasso (1): special case of proposed method without the iteration, i.e., the solution obtained after a single epoch.

· RKHS-Lasso: our proposed method.

TVSINDy was the first method proposed for the ODE discovery problem, as demonstrated in Section 2.1; it was implemented using the MATLAB code provided by the authors. TVLasso represents our minor modifications to the TVSINDy method; we used the lasso algorithm in the MATLAB library after the total variation method for numerical differentiation. The third and fourth methods are proposed by us; note that the former corresponds to the easy version of our method. The hyperparameters were tuned manually.

Benchmark ODE models

· *1D-Spring model*, given by

$$\dot{x} = v, \quad \dot{v} = -kx - vv, \tag{18}$$

where $\boldsymbol{x}(t) \equiv [x(t), v(t)]$ consisting of the position and velocity, k and v are the model parameters expressing spring constant and air resistance constant, respectively.

· *Lotka-Volterra model* [20] is a model for ecological system that is used to describe the interactions between two species corresponding to predators and preys. The accurate ODE can be described as follows:

$$\dot{H} = H(\alpha - \beta P), \quad \dot{P} = -P(\gamma - \delta H) \tag{19}$$

· *Lorentz system*[21] was developed as a simplified mathematical model for atmospheric convection. The true ODE can be described by

$$\dot{x} = \sigma(y - x), \dot{y} = x(\rho - z) - y, \dot{z} = xy - \beta y \tag{20}$$

where $\boldsymbol{x}(t) \equiv [x(t), y(t), z(t)]$ correspond to the rate of convection, horizontal temperature, and vertical temperature, respectively.

· *Enzyme kinetics*[2] is a well-known mathematical formulation for enzyme-catalyzed reactions that can be described by four-dimensional ODE systems:

$$\begin{aligned}
[\dot{S}] &= -k_1[E][S] + k_{-1}[ES], \\
[\dot{E}] &= -k_1[E][S] + (k_{-1} + k_2)[ES], \\
[\dot{ES}] &= k_1[E][S] - (k_{-1} + k_2)[ES], \\
[\dot{P}] &= k_2[ES]
\end{aligned} \tag{21}$$

where $\boldsymbol{x}(t) \equiv [[S], [E], [ES], [P]]$ correspond to a substrate, enzyme, complex, and product, respectively.

Settings of kernels and library

In this study, the least-square kernel, $k(t,t') = a\exp\left((t-t)^2 / 2b^2\right)$, was used for the spring, Lotka-Volterra, and Lorentz systems and the sigmoid kernel, $k(t,t') = \sigma^2 \arcsin(a + btt'/Z)$, where $Z = \sqrt{(a+bt^2+1)(a+bt'^2+1)}$, was used for enzyme kinetics. Note that the derivatives of each kernel with respect to t can be analytically computed (see supplement in[17]). The library of the candidates of nonlinear functions were set to be second order polynomials: $\Theta(\mathbf{X}) = [\mathbf{1}, \boldsymbol{X}, \boldsymbol{X}^2]$. Thus, the numbers of features, D, in each variable was 4 for the spring and Lotka-Volterra models, 10 for the Lorentz system, and 15 for enzyme kinetics.

2.4. Results

Two criteria were used to compare the performances: the MSE of $\boldsymbol{B}$ defined by $\Delta\boldsymbol{B} = 1/Dd \sum_{i=1}^{Dd} \left\|\hat{\boldsymbol{B}} - \boldsymbol{B}_{\text{true}}\right\|_2^2$ and Fscores defined by the harmonic mean of precision and recall, where $\hat{\boldsymbol{B}}$ denotes the value estimated by each method.

In Fig. 1, each component of $\hat{\boldsymbol{B}}$ is compared with the ground truth $\boldsymbol{B}_{\text{true}}$ in two cases with different noise levels for the (a) Lorenz system and (b) Enzyme system, where the regularization parameter λ_s is tuned so as to give the best Fscore by changing it systematically. Note that λ_s corresponds to the threshold of the iterative scheme in TVSINDy and the L1 regularized parameter in TVLasso, RKHS-Lasso(1), and RKHS-Lasso respectively. When the noise is large, more misidentifications occur; while, the parameters obtained with RKHS-Lasso are close to the true value.

Table 1 summarizes the performance in four benchmark ODE models with two different noise levels. It is evident that the proposed method outperforms the baselines in most cases.

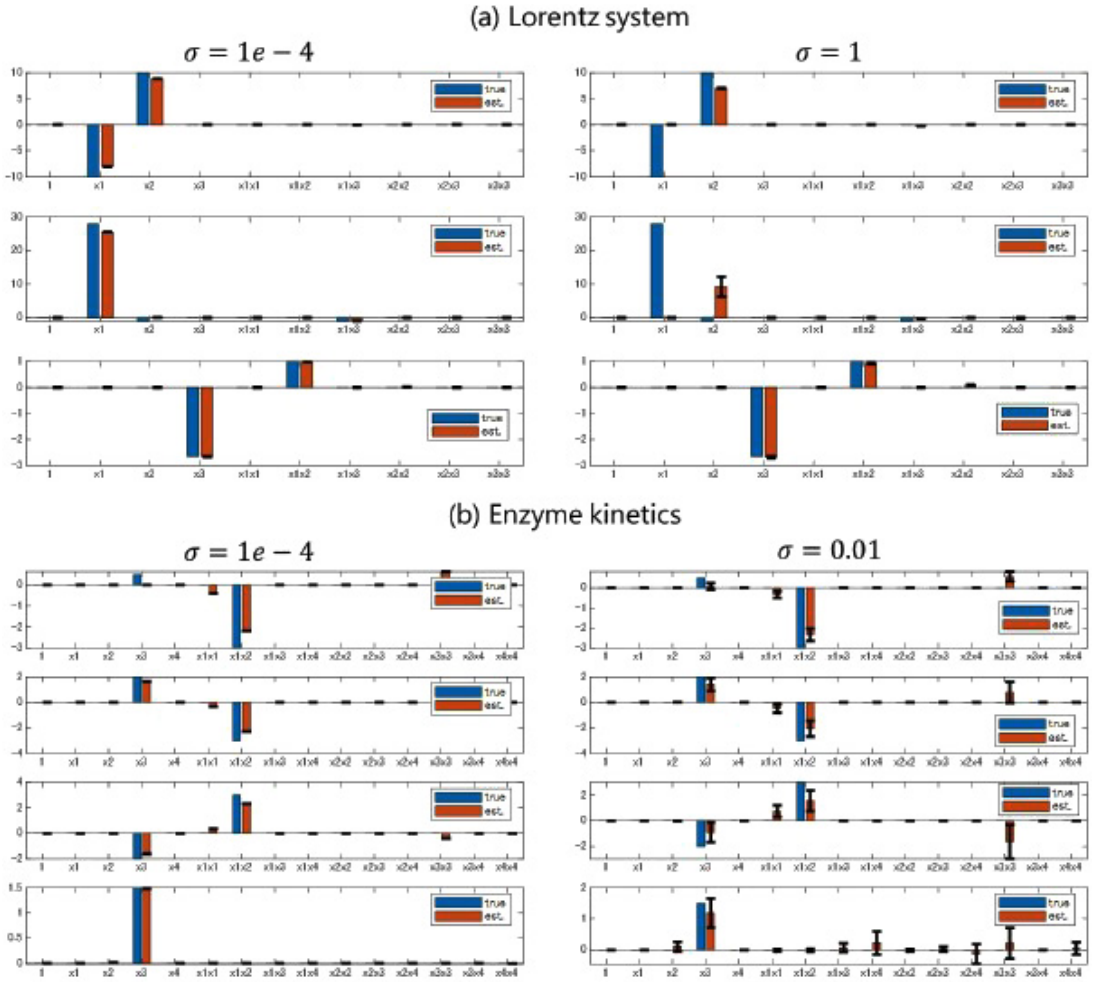

Fig. 1 Each panel shows both the ground truth (blue bars) and the estimated parameters (red bars) in each candidate function.

Table 1 MSE and Fscores in four benchmark ODE models. The means and standard deviations (values in the bracket) over 10 simulation trials are shown with the regularization parameter optimized for the Fscores.

			TVSINDy	TVLasso	RKHS-Lasso (1)	RKHS-Lasso
Spring model	sigma = 1	MSE (min)	0.3128 (0.0943)	0.0485 (0.0522)	0.0334 (0.0322)	**0.0148 (0.0215)**
		Fscore (max)	0.7250 (0.0876)	**1.0000 (< 1e-6)**	**1.0000 (< 1e-6)**	**1.0000 (< 1e-6)**
	sigma = 5	MSE (min)	1.9133 (2.0197)	0.6157 (0.6381)	0.4620 (0.365127)	**0.4096 (0.3473)**
		Fscore (max)	0.6810 (0.0698)	0.7490 (0.1797)	0.8062 (0.1946)	**0.8157 (0.1838)**
Lotka-Volterra model	sigma = 1	MSE (min)	0.1667 (< 1e-6)	5.2e-4 4 (1.3e-4)	2.3e-4 4 (6.3e-5)	**1.3e-5 (1.2e-5)**
		Fscore (max)	0.6667 (< 1e-6)	**0.8000 (< 1e-6)**	**0.8000 (< 1e-6)**	0.7782 (0.0351)
	sigma = 5	MSE (min)	0.1667 (< 1e-6)	0.0014 (0.0012)	3.4e-4 (3.7e-4)	**2.8e-4 (4.0e-4)**
		Fscore (max)	0.6667 (< 1e-6)	0.7442 (0.0534)	0.7648 (0.0486)	**'0.8004 (0.1244)**
Lorentz system	sigma = 1e-4	MSE (min)	29.8885 (1.7e-4)	5.5922 (1.2e-4)	0.5169 (2.9e-5)	**0.0091 (2.4e-5)**
		Fscore (max)	0.6667 (< 1e-6)	0.7143 (< 1e-6)	0.7368 (< 1e-6)	**0.7778 (< 1e-6)**
	sigma = 1	MSE (min)	23.4052 (12.9023)	9.1514 (0.8997)	3.620779 (0.5580)	**1.964616 (0.5135)**
		Fscore (max)	0.6808 (0.0403)	**0.7143 (< 1e-6)**	**0.71433 (< 1e-6)**	**0.7143 (< 1e-6)**
Enzyme kinetics	sigma = 1e-4	MSE (min)	> 1e + 3	0.5599 (1.7e-4)	'0.3145 (0.2169)	**0.04343 (2.0e-4)**
		Fscore (max)	0.2093 (0.0010)	0.2908 (0.0333)	36 (0.0685)	**0.57711 (0.0120)**
	sigma = 0.01	MSE (min)	> 1e + 3	0.6229 (0.004699)	0.2953 (0.2719)	**0.2491 (0.2606)**
		Fscore (max)	0.2285 (0.0238)	0.2000 (< 1e-6)	0.4651 (0.0901)	**0.4831 (0.0849)**

2.5. Short summary

We proposed a new method to solve the ODE discovery problem that combined the RKHS-based method for interpolating the signals from the time series measurements and the sparse inference for selecting relevant bases from the library of possible features.

Our simulation studies showed that the proposed method compared favorably with the baseline methods based on sparse inference with the total variation regularized derivatives.

3 Useful domain knowledge to introduce in machine learning systems

We briefly review the Informed Machine Learning and provide the useful prior knowledge in manufacturing for developing interpretable learning systems that deal with insufficient data.

3.1. Overview of Informed Machine Learning

Informed Machine Learning is a framework where prior knowledge is explicitly integrated into the machine learning pipeline (Fig. 2). Rueden et al. defined "*knowledge*" as validated information about the relations between entities in certain contexts[11]. Such additional information will make the conventional machine learning techniques performed by data driven approaches more powerful in the following aspects:

・Incorporating what we have accumulated in a domain so far into a new system; prediction accuracy may be higher.

・By effectively utilizing the "knowledge and human resources" assets of a domain, unique systems can be developed.

・Interpretability for the learning processes and predicted results can be improved.

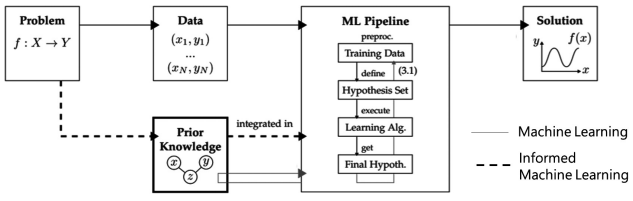

Fig. 2 Concept of Informed Machine Learning[11].

The taxonomy of the knowledge source, knowledge representation, and knowledge integration was elaborated[11), *2]. Here, we reconsider the part of "knowledge sources" from the manufacturing perspective.

3.2. Useful domain knowledge

Knowledge source refers to the origin of prior knowledge, which means various types of knowledge. They can be categorized as follows.

Natural Science: it is typically validated explicitly through scientific experiments (e.g., the universal laws of physics, bio-molecular descriptions of genetic sequences, or material-forming production processes).

Design information*: it denotes the specifications and mechanical information used in product design, including component dimensions, design layout, and structure of the products.

Process flows*: it represents the product manufacturing process and manufacturing settings. It sometimes includes staffing, inspection equipment settings, factory size, and inventory for the production.

Confidence*: it denotes the reliability for annotations or data. Sometimes, data labels may vary; in such cases, the confidence is given at the same time as data.

Domestic reports/ Past cases*: it denotes the past cases and considerations confirmed in-house, which are often given heuristically.

Aggregated human knowledge: it represents the facts from everyday life that are known to almost everyone and can also be called general knowledge.

(Expert's) Intuition: it denotes the knowledge based on the experiences and insights of experts that may not always have scientific evidence.

It should be noted that the knowledge sources marked with * are newly introduced in addition to the original form (Fig. 2 in[11]) from the viewpoint of manufacturing companies. The framework enriches our approaches of machine learning development.

4 Summary

We introduced two topics in this article: 1) ODE discovery problem and 2) useful domain knowledge to introduce in machine learning systems. In the former, we proposed an algorithm for discovering the functional form of ODE from time-series data that combined the gradient matching method and sparse inference; the proposed method outperformed other baseline methods. The latter provided an effec-

*2 In the original paper, the process of integrating prior knowledge into the machine learning pipeline was systematically investigated as following perspectives: 1) "what type of knowledge is integrated?", 2) "how is the knowledge represented or transformed?", 3) "where is the knowledge integrated in the machine learning pipeline?".

tive and usable domain knowledge in manufacturing processes for developing the Informed Machine Learning that is effective framework for integrating the prior knowledge into the machine learning pipeline. Our proposition will be useful for future machine learning techniques and data science development.

References

1) James D. Murray: Mathematical Biology: I. An Introduction, Third ed. (Springer, 2002).
2) G. M. Suel, J. Garcia-Ojalvo, L. M. Liberman and M. B. Elowitz: "An excitable gene regulatory circuit induces transient cellular differentiation", *Nature*, **440** (2006), 545–550.
3) A. Karpatne, G. Atluri, J. Faghmous, M. Steinbach, A. Banerjee, A. Ganguly, S. Shekhar, N. Samatova and V. Kumar: "Theory-guided Data Science: A New Paradigm for Scientific Discovery from Data", *IEEE Transactions on Knowledge and Data Engineering*, **29** (2017), 2318–2331.
4) Geoffrey G. Towell and Jude W. Shavlik: "Knowledge-based artificial neural networks", *Artificial Intelligence*, **70** (1994), 119–165.
5) Y. Otsubo: "AI Research in Manufacturing—Thinking Away from Science", *Bulletin of the Japan Society for Industrial and Applied Mathematics (in Japanese)*, **29** (2019), 26–30.
6) M. L. Minsky: "Logical versus analogical or symbolic versus connectionist or neat versus scruffy", *AI magazine*, **12** (1991).
7) W. J. Murdoch, C. Singh, K. Kumbier, R. Abbasi-Asl and B. Yu: "Definitions, methods, and applications in interpretable machine learning", *PNAS,* **116** (2019), 22071–22080.
8) T. Yu: "Incorporating Prior Domain Knowledge Into Inductive Machine Learningg: Its implementation in contemporary capital markets", Ph.D. thesis, Faculty Inf. Technol., Univ. Technology, Sydney, Australia (2007).
9) A. Karpatne, W. Watkins, J. Read and V. Kumar: "Physics-guided neural networks (pgnn): An application in lake temperature modeling", *arxiv*., 1711.11157 (2017).
10) Y. Otsubo, N. Otani, M. Chikasue and M. Sugiyama: "Failure factor detection in production process", JSAI2020, 2I4-GS-2-04, (2020) (in Japanese).
11) L. von Rueden, S. Mayer, K. Beckh, B. Georgiev, S. Giesselbach, Raoul Heese, Birgit Kirsch, Julius Pfrommer, Annika Pick, R. Ramamurthy, M. Walczak, J. Garcke, C. Bauckhage and J. Schuecker: "Informed Machine Learning - A Survey and Taxonomy of Integrating Knowledge into Learning Systems", *arxiv*., 1903.12394*v*2 (2016).
12) Steven L. Brunton, Joshua L. Proctor and N. Kutz: "Discovering governing equations from data by sparse identification of nonlinear dynamical systems", *PNAS*, **113** (2016), 3932–3937.
13) R. Tibshirani: "Regression shrinkage and selection via", *Journal of the Royal Statistical Society. Series B*, **58** (1996), 267–288.
14) Y. Otsubo and S. Nakajima: "Discovery of Governing equations in Reproducing Kernel Hilbert space", *IEICE Technical Report (IBISML2019-65)*, **118** (2018), 159–166.
15) R. Chartrand: "Numerical Differentiation of Noisy, Nonsmooth Data", *International Scholarly Research Network, ISRN Applied Mathematic*, **2011** (2011).
16) B. Calderhead, M. Girolami and N. D Lawrence: "Accelerating Bayesian inference over nonlinear differential equations with Gaussian processes", *In Proceedings of Advances in Neural Information Processing Systems (NIPS)* (2013), 217–224.
17) F. Dondelinger, M. Filippone, S. Rogers and D. Husmeier: "ODE parameter inference using adaptive gradient matching with Gaussian processes", *In Proceedings of the Sixteenth International Conference on Artificial Intelligence and Statistics (AISTATS)* (2013), 216–228.
18) M. Niu, S. Rogers, M. Filippone and D. Husmeier: "Fast inference in nonlinear dynamical systems using gradient matching", *In Proceedings of the 33rd International Conference on Machine Learning (ICML)* (2016), 1699–1707.
19) S. Boyd, N. Parikh, E. Chu, B. Peleato and J. Eckstein: "Distributed Optimization and Statistical Learning via the Alternating Direction Method of Multipliers", *Foundations and Trends in Machine Learning*, **3** (2011), 1–122.
20) Alfred J. Lotka: "Analytical Note on Certain Rhythmic Relations in Organic Systems", *PNAS*, **6** (1920), 410–415.
21) Edward N. Lorenz: "Deterministic nonperiodic flow", *Journal of the atmospheric sciences*, **20** (1963), 130–141.

大坪洋介
Yosuke OTSUBO
研究開発本部
数理技術研究所
Mathematical Sciences Research Laboratory
Research & Development Division

中島伸一
Shinichi NAKAJIMA
ベルリン工科大学
理化学研究所
Technische Universität Berlin
RIKEN

小規模スポーツイベントにおける観客の盛り上がり分析手法

阿部和広，中村ちから，大坪洋介，小池哲也，横矢直人

Spectator Excitement Analysis Method in Small-scale Sports Events†

Kazuhiro ABE, Chikara NAKAMURA, Yosuke OTSUBO, Tetsuya KOIKE and Naoto YOKOYA

観客の盛り上がりを検知することによって自動ハイライト生成や自動映像編集などの様々な応用が可能であり，観客分析が幅広く研究されている．観客分析の手法として，全体論的手法とオブジェクトベース手法がある．先行研究の多くは全体論的手法を用いているが，大規模な試合と比べて観客の数が少ない小規模な試合では有効ではない．そこで，本研究では，オブジェクトベース手法を用いた小規模な試合における観客の盛り上がり検知手法を提案する．本手法の有効性を検証するために，観客と選手を撮影したデータセットを構築した．実験を行った結果，全体論的手法のベースラインと比べて性能が良く，観客個人の盛り上がり検知も可能になった．また，検知結果から盛り上がりシーン分析を行った結果，盛り上がりスコアが高いシーンが高得点ゴールシーンに対応していることが分かった．

The detection of the excitement of spectators in sports is useful for various applications, such as automatic highlight generation and automatic video editing. Therefore, spectator analysis has been widely studied. Two main approaches used for this include holistic and object-based approaches. Holistic approaches have been applied in most previous studies; however, they are not applicable to small-scale games, where the number of spectators is fewer compared to those of large-scale games. We herein propose a method for detecting the excitement state of spectators in small-scale games using an object-based approach. To evaluate our method, we build our own datasets comprising both spectator and player videos. Experimental results show that our method outperforms a holistic baseline method and allows the excitement detection of individual spectators. Moreover, we discovered that scenes with higher excitement scores correspond to high-score-goal scenes through the analysis of scenes pertaining to excitement using our method.

Key words スポーツ映像分析，大衆行動分析，盛り上がり検知，行動認識
sports video analysis, crowd behavior analysis, excitement detection, action recognition

1 Introduction

Understanding and analyzing crowd dynamics is important in various fields, such as surveillance, advertising, determining movie ratings, and automatic video editing. Even in sports, the reactions and motions (i.e., excitement) of spectators can be utilized to extract information regarding games because they are significantly related to the impressiveness of the sports events. In particular, the excitement state is a useful parameter as it enables one to measure the appeal of gaming events. Information regarding spectator excitement has been used for highlight generation[1)~3)] and automatic video editing[4)].

Spectator analysis has been well studied for crowd analysis. Crowd analysis has attracted attention in past decades in the field of computer vision. It has been studied in the context of crowd behavior analysis[5)], crowd density estimation[6)], and crowd motion detection[7)]. Typically, two different approaches are used in crowd analysis: holistic and object-based ones[8)]. Holistic approaches address crowds themselves rather than the details of each individual. Meanwhile, object-based approaches focus on the behavior of individuals rather than that of crowds. Both approaches can be applied for spectator analysis; however, most previous studies relied on holistic approaches[2)9)]. This is because these studies focused on large and major games, where the number of spectators is high.

In this study, we performed an excitement detection of

† This article contains the review of the paper[24)]

spectators for small-scale games, where the number of spectators was fewer compared with those of large-scale games. The following factors were considered in this study: 1) the density of spectators was sparse, 2) the accommodation of facilities was small, and 3) the positions of cameras were restricted. Conventional holistic approaches, although applicable to the case of dense spectators, fail in small-scale settings because of the problems above; this is because it is difficult to record videos that include only spectators due to factors 2) and 3). Hence, we propose a novel method for spectator excitement detection, which is based on an object-based approach. Our method comprises three aspects: a) upper body detection based on face detection, b) spectator classification, and c) scoring for excitement based on convolutional neural network (CNN) architectures.

As mentioned, distinguishing between spectators and other people (e.g., players or referees) is necessary, which corresponds to b). To achieve this, we performed a) as a preprocessing step. For c), we input an optical flow of spectators into a two-stream CNN[10] and defined the excitement score based on the features of the neural network.

Our contributions are summarized as follows:

- We proposed an approach to detect the state of spectator excitement for the case of sparse spectators.
- We acquired the video datasets of both spectators and players in 3 × 3 basketball games.
- We applied our method to our datasets and evaluated the performance.

This paper is organized as follows. In Section 2, we explain the details of our datasets and methods to annotate the states of spectator excitement. In Section 3, we describe our method in detail; in Section 4, results including performance evaluations are provided. Finally, we summarize our study in Section 5.

2 Dataset

(1) Dataset preparation

Several datasets are available for crowd analysis[11)~13)]. However, these datasets are primarily designed for public crowd analysis. In the study of spectator analysis in sports, the motion patterns of spectators are significantly related to player actions and game events. Therefore, to analyze crowd excitement, datasets that include game information corresponding to crowd motions are desirable.

Furthermore, publicly available datasets have been presented to analyze sports such as soccer[14)], volleyball[15)], and ice hockey[9)]. In particular, the S-Hock dataset[9)] is a unique dataset that captures both players and spectators simultaneously and contains dense annotations of each spectator. While the S-Hock dataset is valuable for our study, it primarily focuses on dense crowds in large games and excludes detailed appearances, which we aim to capture.

To evaluate our approach, we built our own dataset comprising videos recorded during a 3 × 3 basketball tournament organized by Alborada in Tsukuba city, Japan. This tournament included 12 games and lasted approximately 154 min.

We set up three types of cameras: spectator, field, and overlooking cameras. Six spectator cameras were used to record the motions of spectators from their seats. In addition, we set up five field cameras to record the actions of the players. Additionally, we set up four overlooking cameras to capture the overlooking view of the game. In each game, all cameras were temporally synchronized. The overall camera configuration is shown in Fig. 1. We used 4K resolution cameras to obtain fine-grained appearance information of spectators. Some example frames are shown in Fig. 2.

(2) Annotation

We annotated the moment spectator excitement detected during the game. It was difficult to determine whether an individual was excited/not excited only by watching spectator videos because they exhibited various behaviors and reactions, which varied by person. Hence, we conducted frame-level labeling based on events occurring in the field.

We assumed that the spectators were generally excited immediately after a goal was achieved, and that the excitement continued for a few seconds. After localizing the moment of the goal achievement as the time when the ball was shot into the target, we identified the excitement duration. Excitement was defined by spectator actions, such as

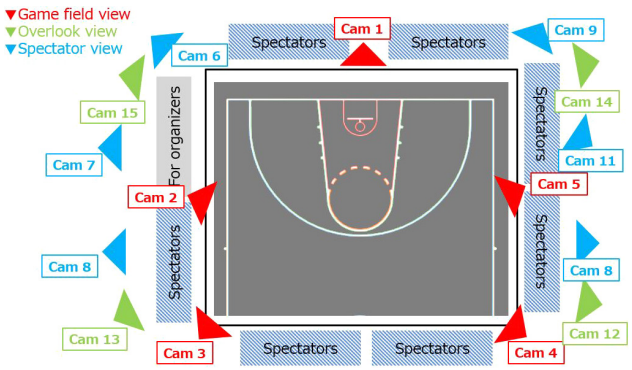

Fig. 1 Camera configuration. Red triangles indicate the field cameras that capture players. Green triangles indicate overlooking cameras that cover the overlooking view of the game. Blue triangles indicate spectator cameras that cover spectator seats.

(a) Spectator cameras

(b) Field cameras

(c) Overlooking cameras

Fig. 2 Example frame of our dataset. We obtained 4K resolution videos; however, these example images are resized to reduce image size. Videos are captured by Jiro Akiba/Getty Images.

clapping and arm raising.

3 Method

We propose an excitement detection algorithm based on an object-based approach, illustrated in Fig. 3. To capture individual appearance features, our method starts by detecting and tracking as a preprocessing step. After each person was tracked, we used a motion CNN with a two-stream architecture[10] to extract deep features; output features were generated through a trainable fully connected neural network. Subsequently, discriminative motion features of each person were aggregated to form the final frame-level score. Our

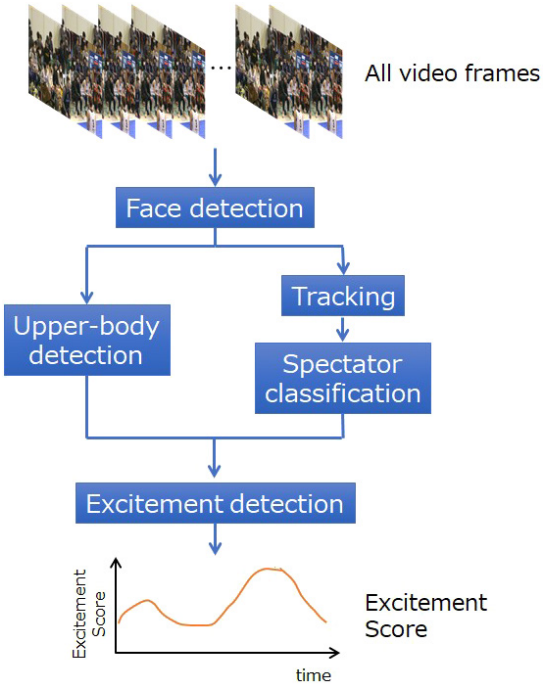

Fig. 3 Overview of our object-based excitement detection algorithm.

motion CNN architecture can be end-to-end trained without information regarding the excitement of each person.

(1) Upper body detection based on face detection

We analyzed the features of each person based on face detection. Human detection is extremely difficult because the bodies of spectators are generally occluded and overlapped. By contrast, their faces are clearly visible and have no overlaps. Hence, it is reasonable to extract information from faces.

In general, detecting small faces is challenging. We used Single Shot Scale-invariant Face Detector (S3FD)[16] pretrained on WIDER FACE[17] as a face detector. S3FD is based on an anchor matching strategy where small faces can be detected with high accuracy. Furthermore, S3FD offers reliability in face detection. To remove misdetections, we accepted bounding boxes with reliabilities higher than 0.5.

After detecting faces, we determined the bounding box of each spectator in the following manner. Assuming the ratio of the face to the upper body regions is almost the same for each person, we determined the upper body bounding box using the following linear relationships:

$$b^B_{x1} = b^F_{x1} + a_{x1} * w, \quad (1)$$

$$b^B_{y1} = b^F_{y1} + a_{y1} * h, \quad (2)$$

$$b^B_{x2} = b^F_{x2} + a_{x2} * w, \quad (3)$$

$$b^B_{y2} = b^F_{y2} + a_{y2} * h, \quad (4)$$

where (b_{x1}, b_{y1}), (b_{x2}, b_{y2}) are the x, y coordinates of the upper-left and lower-right bounding boxes, respectively;

superscript B and F indicate the upper body and face, respectively; w and h denote the width and height of the bounding box of the face, respectively; a_{x1}, a_{x2}, a_{y1}, and a_{y2} are fitting coefficients set as $a_{x1} = -2$, $a_{y2} = -0.5$, $a_{x2} = 2$, and $a_{y2} = 4$ from empirical observation.

(2) Spectator classification

Although our target was the audience sitting on the seats, they were sometimes occluded by the players because the seats were set up close to the basketball field. In addition, some people were standing behind the seats to watch the game. Therefore, we had to distinguish the audience sitting on the seats from other people in the videos.

We classified the persons in the video into two groups: the static group and the dynamic (moving) group; the people of the latter group were excluded from spectator analysis.

First, we tracked all the persons in the videos throughout the game by the SORT tracker[18]. We then obtained the trajectories of the coordinates for each person. We classified them into two groups, in which we assigned a person into the static group if his/her coordinates of the center of the bounding box had changed within a fixed threshold; otherwise, they were assigned to the other group. We fixed the threshold parameter as 800 pixels for our 4K videos (3840 × 2160 pixels). Fig. 4 shows the qualitative result.

(3) Excitement detection

To detect the excitement state, we introduced a neural network architecture based on the temporal stream of a two-stream CNN[10]. Fig. 5 illustrates the overview of the architecture. First, following the procedures of a two-stream CNN, we prepared optical flow images containing two channels: a horizontal and a vertical component.

For a series of optical flow images, the optical flow images of 10 consecutive frames corresponding to the position of the detected upper body bounding boxes were stacked and treated as a patch. In all consecutive frames, we selected n_p patches randomly and fed them as inputs to the motion CNN. The outputs of the motion CNN were then pooled to aggregate individual scores and form the final score. We investigated the average pooling and max-pooling for person aggregation. The cross-entropy loss was used to learn from the label (excited/not excited).

We used 101-layer residual network (ResNet-101) as the backbone of the two-stream CNN architecture[19]. To avoid overfitting and leverage general motion features acquired

Fig. 4 Qualitative result of spectator classification. Bounding boxes of non-spectators are filled out. Original videos are captured by Jiro Akiba/Getty Images.

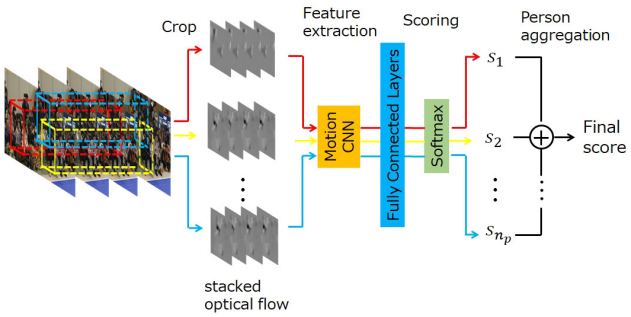

Fig. 5 Architecture of our module for excitement detection.

from a large dataset, we used a model[20] pretrained for action recognition on the UCF-101 dataset[*1, 21] and fine-tuned it. Because the feature to be captured was motion, we did not use the spatial stream and only used the temporal stream in the two-stream network. For fine tuning, fully connected layers of ResNet-101 were replaced with two fully connected layers having 10 and 2 output units; the output was the softmax score.

The optical flow was computed using the OpenCV implementation of the TV-L1 algorithm[22]. Following the implementation[20], the extracted optical flow was clipped to the range $[-20, 20]$, rescaled to the range $[0, 255]$ by linear transformation and compressed to JPEG.

In this study, we used only videos of the final and semifinal games because the spectators exhibited excitement clearly. Generally, whether one exhibits excitement depends on the team support. Therefore, we used the excitement labels from only the home team. Among 116,628 training frames, only 5,376 frames had positive labels (i.e., "excited"). For each set of 10 consecutive frames, we simply used the label of the first frame. To learn from biased data, we sampled positive and negative frames equally. We treated a set of 10 consecutive frames including n_p patches

[*1] Standard action recognition benchmark dataset.

as a batch and set the batch size to 2. We trained 20 epochs and used the Adam optimizer[23] with a learning rate of 0.0001, $\beta_1 = 0.9$, and $\beta_2 = 0.999$.

4 Evaluation

(1) Baseline method

To compare our methods with a conventional holistic method, we considered a baseline method based on a holistic approach, similar to that in[2]. This baseline method does not detect or track individuals; it is different from our method only in the cropping stage, as shown in Fig. 5. This baseline crops a fixed rectangular area (480 × 540 pixels) of the frame to form a patch and processes it as shown in Fig. 5 to obtain the final score. This patch contains one or two persons. We randomly sampled eight patches from the entire rectangular area by a sliding window with a 240 × 270 pixel (half the size of the patch) overlapped area.

(2) Comparison with baseline method

We evaluated our method on a test set corresponding to the second half of each game. Because our data were highly biased, we sampled the same number of frames from the "excited" and "not excited" classes in the following evaluations. Table 1 shows the recall, precision, and average precision of the baseline method and our proposed method. We considered different pooling methods: average pooling and max pooling. Moreover, we considered two cases of the following number of patches: $n_p = 8$ and $n_p = 16$. In both cases, the training was conducted only for $n_p = 8$. For all cases, the recall–precision curves are shown in Fig. 6.

As shown in Table 1, our method clearly outperformed the baseline method. For different types of pooling of our methods for person aggregation, the max pooling method achieved a better average precision score; however, the performance gap was relatively small. In both pooling methods, increasing n_p improved the performance, which was expected considering that more spectator information was obtained.

(3) Individual excitement detection

Next, we conducted an individual excitement detection. In our method, the frame-level score was calculated by pooling the sigmoid scores of individual patches. Therefore, once training was completed, we obtained the individual-level score by extracting the score before pooling. Fig. 7 shows the individual- and frame-level scores in a certain period of the game. Although the scores were calculated for all individual patches, n_p was set to 8 in the training phase.

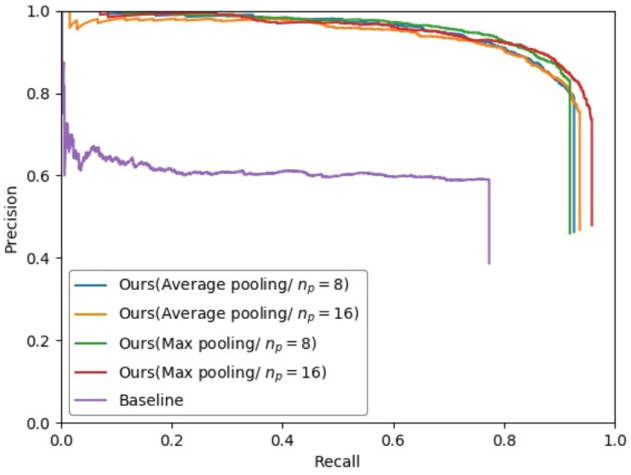

Fig. 6 Recall–precision curve for our methods and baseline method.

Table 1 Recall, precision, and average precision (AP). (Ave: average pooling, Max: max pooling, n_p: number of patches)

Method	Recall	Precision	AP
Baseline	57.3%	77.3%	46.6%
Ours (Ave./ $n_p = 8$)	77.5%	92.7%	88.5%
Ours (Ave./ $n_p = 16$)	76.3%	93.7%	90.0%
Ours (Max/ $n_p = 8$)	**80.7%**	91.9%	88.8%
Ours (Max/ $n_p = 16$)	76.5%	**95.9%**	**91.7%**

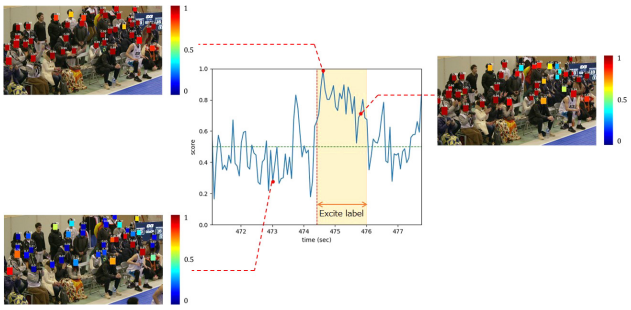

Fig. 7 Qualitative results of individual excitement. Red dotted vertical line is the moment a goal is achieved, and the following span (orange) is the moment of excitement set as a ground truth label. Score is visualized on the bounding box of each individual in each frame. Original videos are captured by Jiro Akiba/Getty Images.

Although we could not evaluate the quantitative performance because the ground truth excitement scores of each individual were unknown, as shown in Fig. 7, our method can successfully provide the excitement score of each individual.

(4) Scene analysis

Finally, we analyzed the scene with high excitement score

calculated using our method. A scene is defined as a sequence of consecutive 30 frames. To extract the scene, we first calculated the frame-level score using the excitement detection method described in Section 3. Subsequently, we calculated the scene score by the sliding window approach, which yielded the mean value for sliding the window size. The sliding window size was 30 frames, and each sliding window was non-overlapping.

We extracted scenes with the top-five highest scene scores from the second half of the final game and analyzed each scene, as shown in Table 2. We confirmed that each scene signified the goal scene from the home team by observing the video clip corresponding to the detected scene. Additionally, we discovered four scenes that were two-point scenes, which encompassed all two-point scenes in the second half of the final game. The two-point goal was the highest point goal in the 3 × 3 basketball game.

From the analysis above, we can conclude that scenes with higher excitement scores corresponded to the high-score goal scenes.

Table 2 Top-five highest scenes from calculated scene score

Rank	Frame #	Score	Point
1	24949	0.92	Two
2	22885	0.83	Two
3	21712	0.80	One
4	28469	0.80	Two
5	19741	0.79	Two

5 Conclusion

We herein proposed an object-based approach for spectator excitement detection. To evaluate the performance of our approach, we built original video datasets comprising spectators and players. Through several evaluations, we demonstrated the effectiveness of our algorithm over the traditional holistic method for our dataset and the qualitative performance of the individual excitement detection method. Using our algorithm, we analyzed the excitement scene and showed that higher excitement scores corresponded to high-point goal scenes.

References

1) D. Conigliaro, F. Setti, C. Bassetti, R. Ferrario and M. Cristani: “Attento: Attention observed for automated spectator crowd analysis”, *Human Behavior Understanding*, (2013), 102–111.
2) M. Godi, R. Paolo and F. Setti: “Indirect match highlights detection with deep convolutional neural networks”, *New Trends in Image Analysis and Processing – ICIAP* 2017, (2017), 87–96.
3) V. Bettadapura, P. Caroline and E. Irfan: “Leveraging contextual cues for generating basketball highlights”, *Proceedings of the 24th ACM international conference on Multimedia*, (2016), 908–917.
4) M. Merler, D. Joshi, Q.-B. Nguyen, S. Hammer, J. Kent, J. R. Smith and R. S. Feris: “Automatic Curation of Sports Highlights using Multimodal Excitement Features”, *IEEE Transactions on Multimedia*, **21** (2018).
5) R. Mehran, B. E. Moore and M. Shah: “A streakline representation of flow in crowded scenes”, *European Conference on Computer Vision*, (2010), 439–452.
6) X. Wu, G. Liang, K. K. Lee and Y. Xu: “Crowd density estimation using texture analysis and learning”, *2006 IEEE International Conference on Robotics and Biomimetics*, (2006), 214–219.
7) S. Wu, B. E. Moore and M. Shah: “Chaotic invariants of lagrangian particle trajectories for anomaly detection in crowded scenes”, *2010 IEEE Computer Society Conference on Computer Vision and Pattern Recognition, IEEE*, (2010), 2054–2060.
8) J. C. S. Jacques Junior, S. R. Musse and C. R. Jung: “Crowd analysis using computer vision techniques”, *IEEE Signal Processing Magazine*, **27** (2010), 66–77.
9) D. Conigliaro, P. Rota, F. Setti, C. Bassetti, N. Conci, N. Sebe and M. Cristani: “The s-hock dataset: Analyzing crowds at the stadium”, *2015 IEEE Conference on Computer Vision and Pattern Recognition*, (2015), 2039–2047.
10) Simonyan Karen and Z. Andrew: “Two-stream convolutional networks for action recognition in videos”, *Advances in Neural Information Processing Systems*, (2014), 568–576.
11) Robotics and Vision Laboratory, University of Minnesota, Department of Computer Science and Engineering: “A project of the Artifical Intelligence”, *Monitoring Human Activity*. http://mha.cs.umn.edu/proj_events.shtml#crowd, (accessed 2020–05–29).
12) S. Ali and M. Shah: “A lagrangian particle dynamics approach for crowd flow segmentation and stability analysis”, *2007 IEEE Conference on Computer Vision and Pattern Recognition*, (2007), 1–6.
13) B. Solmaz, B. E. Moore and M. Shah: “Identifying behaviors in crowd scenes using stability analysis for dynamical systems”, *IEEE Transactions on Pattern Analysis and Machine Intelligence*, **34** (2012), 2064–2070.
14) S. A. Pettersen, D. Johansen, H. Johansen, V. Berg-Johansen, V. R. Gaddam, A. Mortensen, R. Langseth, C. Griwodz, H. K. Stensland and P. Halvorsen: “Soccer video and player position dataset”, *Proceedings of the 5th ACM Multimedia*

Systems Conference, (2014), 18–23.

15) G. Waltner, T. Mauthner and H. Bischof: "Indoor activity detection and recognition for sport games analysis", *Austrian Conference on Pattern Recognition*, (2014).

16) S. Zhang, X. Zhu, H. S. Zhen Lei, X. Wang and S. Z. Li: "S3fd: Single shot scale-invariant face detector", *Proceedings of the IEEE International Conference on Computer Vision*, (2017), 192–201.

17) S. Yang, P. Luo, C. C. Loy and X. Tang: "Wider face: A face detection benchmark", *2016 IEEE Conference on Computer Vision and Pattern Recognition*, (2016), 5525–5533.

18) A. Bewley, Z. Ge, L. Ott, F. Ramos and B. Upcroft: "Simple online and realtime tracking", *2016 IEEE International Conference on Image Processing*, (2016), 3464–3468.

19) K. He, X. Zhang, S. Ren and J. Sun: "Deep residual learning for image recognition", *2016 IEEE Conference on Computer Vision and Pattern Recognition*, (2016), 770–778.

20) Jeffrey Huang: "Using two stream architecture to implement a classic action recognition method on UCF101 dataset", Github. https://github.com/jeffreyhuang1/two-stream-action-recognition, (accessed 2020–05–29).

21) A. R. Z. M. S. Khurram Soomro: "UCF101: A dataset of 101 human actions classes from videos in the wild", *arxiv preprint*, (2012).

22) C. Zach, T. Pock and B. Horst: "A duality based approach for realtime TV-L1 optical flow", *Pattern Recognition*, (2017), 214–223.

23) D. P. Kingma and J. L. Ba: "Adam: A method for stochastic optimization", *International Conference on Learning Representation*, (2015).

24) K. Abe, C. Nakamura, Y. Otsubo, T. Koike and N. Yokoya: "Spectator Excitement Detection in Small-scale Sports Events", *Proceedings of the 2nd International Workshop on Multimedia Content Analysis in Sports*, (2019).

阿部和広
Kazuhiro ABE
研究開発本部
数理技術研究所
Mathematical Sciences Research Laboratory
Research & Development Division

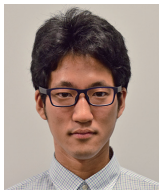

中村ちから
Chikara NAKAMURA
研究開発本部
数理技術研究所
Mathematical Sciences Research Laboratory
Research & Development Division

大坪洋介
Yosuke OTSUBO
研究開発本部
数理技術研究所
Mathematical Sciences Research Laboratory
Research & Development Division

小池哲也
Tetsuya KOIKE
研究開発本部
数理技術研究所
Mathematical Sciences Research Laboratory
Research & Development Division

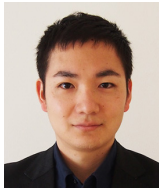

横矢直人
Naoto YOKOYA
東京大学
理化学研究所
The University of Tokyo
RIKEN

2段階触覚フィードバックを用いた空中クリック

伊藤　充，國米祐司，篠田裕之

Midair Click Using Two-State Haptic Feedback

Mitsuru ITO, Yuji KOKUMAI and Hiroyuki SHINODA

本研究では，我々は強度と質の異なる2種類の触感に基づいて，空中で擬似クリック感を提示する方法を提案する．空中触覚ボタンは，空間中の2層の触覚領域により提示される．ユーザの手はセンサーにより追跡され，手の位置に応じて2つの方法で刺激される．ユーザの手が上層にあるとき手の皮膚に弱い触覚が提示され，下層にあるとき強い触覚が提示される．これらの2つの状態は，ニュートラルな接触と操作完了を示す．この空中クリックは，皮膚における超音波の焦点の空間変調が，固定された位置の振幅変調よりも強く知覚される近年の発見により可能になった．我々は，2つの触覚層を知覚できるかを確認する実験を行ない，さらにブラインド状態でのボタン選択操作が可能かどうか調査した．この空中クリックは，視覚や聴覚フィードバックを必要としない空中インタフェースに応用できると考えられる．

In this study, we propose a method to present a non-contact tactile click sensation using airborne ultrasound. This midair click sensation is generated based on two types of tactile sensations having different intensity and quality. We consider two-layers of regions in the space that forms a virtual button. A user's hand is tracked by a sensor and stimulated by the two methods according to the hand position. Within the two tactile layers, a weak or strong tactile sensation is presented on the hand skin when the user's hand is in the upper or lower layer, respectively. These two tactile sensations correspond a contact and action completion. This midair click was enabled by the recent finding that an ultrasound focus motion on the skin produces a stronger perception than amplitude modulation given at a constant position. We conducted experiments to confirm whether two haptic layers can be perceived. In addition, we investigated whether a blind operation of button selection can be performed. This midair click can be applied to midair interfaces where no visual or auditory feedback.

Key words 空中触覚，クリック感，空中超音波，音響放射圧
midair haptics, click sensation, airborne ultrasound, acoustic radiation pressure

1 Introduction

An important tactile function of mechanical input devices, such as a keyboard or a mouse, is to provide users with two sensations corresponding to two states, one indicating a neutral position and the other an action completion position. When a user operates a mouse, the user can hold their finger in the neutral position by perceiving the tactile sensation of the static contact between the finger and the device. Owing to this neutral position, the user can quickly click and convey an input intention to the computer. With this click feedback, a user can reliably perceive action completion by touch.

Such haptic feedback is an effective technique for performing reliable operations in midair haptics. This feedback informs the user's skin of a contact sensation between the virtual object and the hand positioned in a midair gesture.

Midair haptic feedback can be provided by an air vortex[1], an air jet[2], and ultrasound[3)~5)]. Midair haptics using ultrasound can generate a localized pressure distribution on the skin and present a sufficiently perceptible tactile sensation by vibrational stimulation using amplitude modulation.

With this feedback, the user can quickly and comfortably operate an aerial virtual button even in a blind state. This operation requires a slight tactile sensation indicating contact between the skin and the device and a tactile sensation indicating operation completion that can be clearly distinguished from the contact sensation. However, it has been difficult to provide such haptic feedback because the force of the ultrasound stimulus is weak and it cannot clearly generate two distinguishable states with different qualities and intensity in haptic stimulus.

In this paper, we propose a method to generate a quasi-click sensation in the air using unidirectional lateral modulation (LM), which is one of the recently discovered spatial modulation methods[6)7)]. Using vibration stimulation is effective for efficiently stimulating human skin[8)] on devices such as midair tactile displays. Amplitude modulation (AM) has been used as a method for inducing a vibration stimulus in a user. LM can present a tactile sensation that is 10 dB or more stronger than AM. AM mainly stimulates the pacini corpuscle, tactile mechanoreceptors. In contrast, LM stimulates the mechanoreceptors on the surface of the skin, so that in addition to a difference in tactile intensity, LM can cause a tactile sensation different in quality from AM.

The concept of the quasi-click is shown in Fig. 1. Here, we consider a two-layer region in space. The position of the user's hand is tracked with a depth camera, and AM and LM stimuli are presented depending on whether the hand is on the upper layer (AM layer) or the lower layer (LM layer). The user can confirm the position of the virtual button with the sensation of AM and perceive the completion of the button operation with a perception of LM. These two types of haptic feedback present two states: contact, such as a mouse click, and action completion. In addition, this technique can be applied as an aerial version of full/half press, such as a shutter button on a camera, or as a pressure-sensitive touch on a touchpad.

The rest of this paper is organized as follows. First, the implementation of this two-layer tactile button is described. An experiment was performed to see if two tactile layers could be perceived. Next, it was investigated whether blind operation of the button selection can be performed.

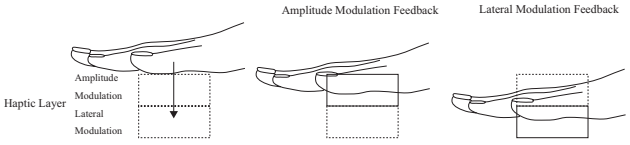

Fig. 1 Midair click using dual-layer haptic feedback. The intensity and quality of haptic feedback are switched according to the hand position.

2 Principle of Midair Tactile Display

Acoustic Radiation Pressure

The relation between sound pressure and radiation pressure[9)10)] is summarized below for the readability of the manuscript. The acoustic radiation pressure P [Pa] is proportional to the sound energy density given by

$$P = \alpha E = \alpha \frac{p^2}{\rho c^2} \tag{1}$$

where E [J/m^3], p [Pa], ρ [kg/m^3], and c [m/s] denote the sound energy density, sound pressure, density of the medium, and sound velocity, respectively. α denotes a constant between 1 and 2 depend on the reflection properties of the object surface. When ultrasound propagates through air and is blocked by the surface of an object, almost all of the ultrasound is reflected at the boundary and in this case the coefficient α becomes nearly 2. Thus, we can control the radiation pressure P by controlling the ultrasound pressure p.

Ultrasound Phased Array

Figure 2 shows the appearance of a phased array. The ultrasound focus was generated using nine units of phased arrays driven at 40 kHz[11)~13)]. The device was composed of 2241 transducers. The focal point could be moved freely by controlling the phase of the ultrasound wave emitted from each transducer. The aperture of the phased array was 576 mm (W) × 454.2 mm (H).

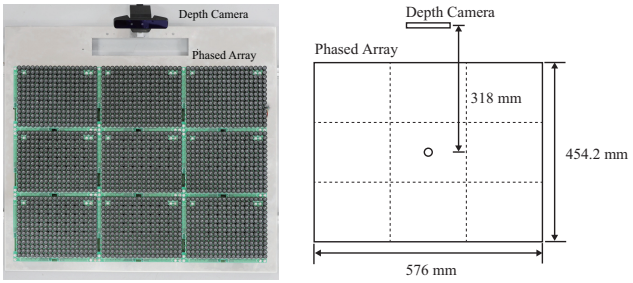

Fig. 2 Prototype device. (a) Photograph of the phased arrays. (b) Schematic diagram of a nine-unit phased array and depth camera.

3 Dual-Layer Haptic Button

Lateral Modulation

The LM modulates the focal point of the ultrasonic wave in one direction using two parameters, the LM vibration amplitude and the LM frequency. The LM oscillation amplitude indicates the spatial movement width of the focal point. The LM frequency indicates the moving speed of the focal point.

The instantaneous values of the sound pressure at AM and LM are as follows.

$$\begin{aligned} p_{AM}(t) &= p_0 \sin(\omega_c t) \sin(\omega_m t), \\ p_{LM}(t) &= p_0 \sin(\omega_c t) \end{aligned} \tag{2}$$

Here, the radiation pressure is proportional to the acoustic energy density and is as follows.

$$P_{AM}(t) = \alpha \frac{\overline{p_{AM}^2}}{\rho c^2}$$
$$P_{LM}(t) = \alpha \frac{\overline{p_{LM}^2}}{\rho c^2} \quad (3)$$

where α is a constant. Assuming that p_{AM}^2, p_{LM}^2 indicates a time average, the relationship of $P_{LM} = 2P_{AM}$ holds. LM can generate twice the radiation power of AM on skin over an average long enough for the modulation frequency of AM.

Dual Haptic Layer

Figure 3 shows the configuration of the dual-layer haptic button. The user's hand position was measured, and stimulated by AM and LM when the hand enters upper and lower layers, respectively. The hand position was used only for layer switching. The focal position of the AM/LM layer was fixed. The AM frequency was 150 Hz. In LM, the LM vibration amplitude and the frequency were 4.5 mm and 50 Hz, respectively, and the LM vibration amplitude was defined as the displacement amplitude of the focal spot on the skin. The depths of the AM layer and LM layer were 50 mm and 100 mm, respectively. The output of the nine phased arrays was 144 mN at maximum intensity. In this experiment, the driving intensities of the phased arrays in the AM and LM layers were 10% and 100%, respectively.

The AM and LM stimuli conveyed two states - a neutral position and action completion, respectively, and produced a quasi-click sensation. To increase the contrast between the two stimuli, we selected specific AM and LM frequencies, such that the tactile feel quality and perceived strength were clearly different following the previous study[7].

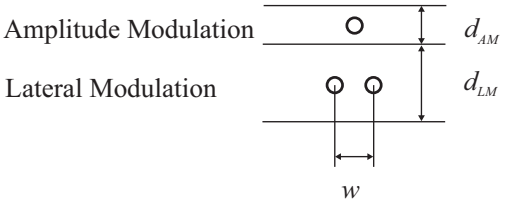

Fig. 3 Schematic diagram of the dual-layer haptic button. The depth d of each layer indicates the region where the AM or LM stimulus is presented. w indicates a value twice that of the LM vibration amplitude.

Acoustic Radiation Pressure Distribution

In this section, the acoustic radiation pressure distributions for the tactile presentations are shown. Figure 4 and 5 are the acoustic radiation pressure distribution shown by the AM and LM layers of the haptic button in Fig. 3, respectively. The focal length is 600 mm, which will be used in the next user study experiment.

Figure 5 shows the time average of the instantaneous sound pressure distribution of the two focal points of the LM stimulus for a sufficiently long period.

Figure 6 shows the sound pressure distribution in the x-z plane for a single focus.

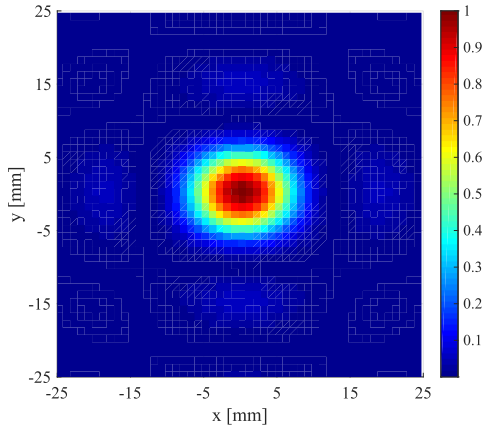

Fig. 4 Simulated normalized acoustic radiation pressure distribution. (AM Layer, Focal distance = 600 mm) The width of the zero points in horizontal section of this distribution is 26 mm.

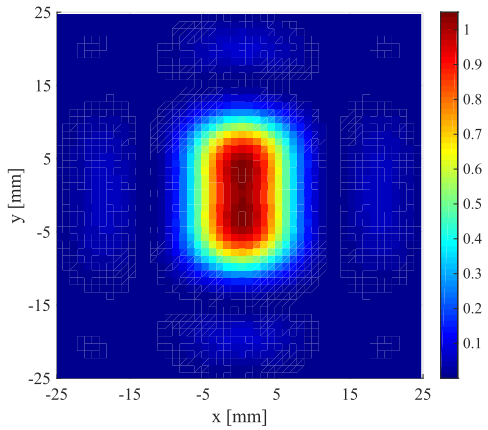

Fig. 5 Simulated normalized acoustic radiation pressure distribution. (LM Layer)

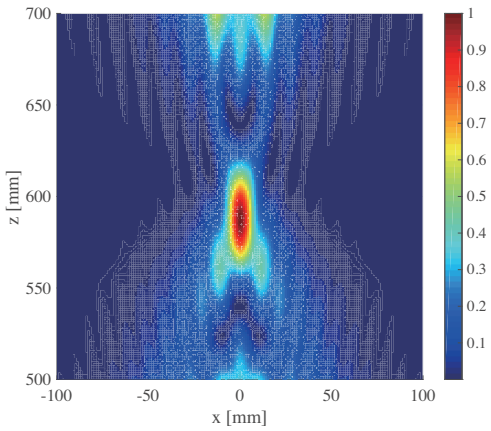

Fig. 6 Simulated normalized acoustic radiation pressure distribution. (AM Layer, x-z plane, Focal distance = 600 mm)

4 Experiment

In this experiment, we presented the tactile sensations of the above-mentioned haptic button and evaluated whether the difference could be perceived by the palm. We presented three buttons in space and investigated whether the buttons could be operated in a blind state. Informed consent was obtained individually from all participants included in the study.

Figure 2 shows the experimental device. The XY coordinates of the focus were determined by the position of the user's hand. The hand position was measured using a Realsense Depth Camera SR300 (Intel).

A. Experiment 1: Identification of the tactile sensation

The experiment setup is shown in Fig. 7. The experimental procedure was as follows. Before the experiment, it was explained to the participants that the haptic button consisted of two layers and they were then were directed to find the upper AM layer by themselves. They were informed that the positions of the buttons were on the front side and the lower side of the initial hand position, as shown in Fig. 8. They wore headphones and listened to white noise to block the audible sounds from the phased array. They identified the height of the top surface of the two tactile layers by matching the center of the palm with the XY coordinates of the focal point. The hand positions of the participants were guided manually to the starting position by the examiner. The participants, with their eyes closed, identified the surface position of the upper AM layer first, followed by the position of the lower LM layer. They freely moved their hands to find the button position and then held the position of their right hand and answered "yes" to inform the examiner that the search was completed. Subsequently, the examiner measured the position of the participants' hand. No time limit was imposed. The answers were obtained from an average of three trials. There were a total of eight participants. All participants were male, aged 23–27 years.

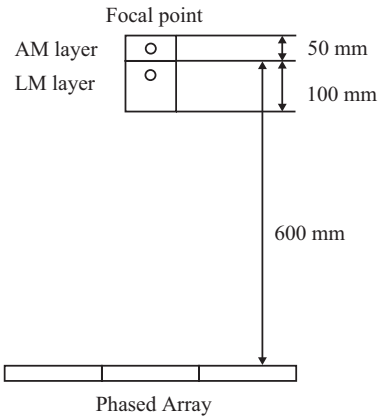

Fig. 7 Experimental setup (front view). The top-surfaces of the upper (AM) and lower (LM) layers were located at heights of 625 mm and 575 mm.

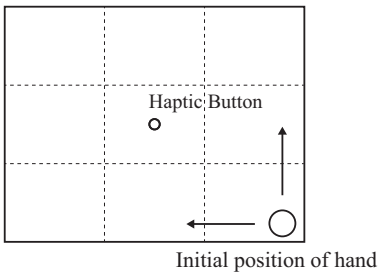

Fig. 8 Experimental setup (top view). The participants placed their hands in the initial position (Z = 800 mm) and started the experiment.

B. Experiment 2: Tactile button operation

In this experiment, which was carried out in a manner similar to experiment 1, three haptic buttons were placed in different positions. Figure 9 shows the arrangement of the haptic buttons. The experimental procedure was as follows. Before the experiment, the participants were informed that three buttons were located side by side in the horizontal direction; however, they were not informed of the distance between the adjacent buttons. At the start of the experiment, the examiner informed the participant using letters and orally, which button out of the three they should select. With their eyes closed, they placed their right hand in the same position as in experiment 1 and identified the position of the instructed button in the same manner as in experiment 1. Next, they identified the position of the top surface of the lower LM layer. The position of the button was presented randomly to them. The answers were obtained from the average of three trials.

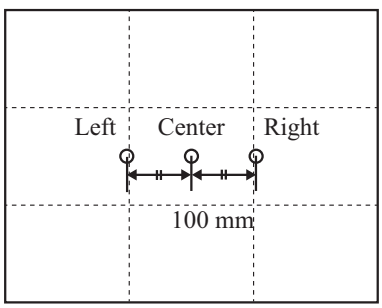

Fig. 9 Experimental setup (top view). Three buttons are arranged at intervals of 100 mm.

5 Results

A. Experiment 1

Figure 10 shows the position of the haptic layer as perceived by the palm. “Distance” indicates the distance from the phased array surface. The error bars indicate the standard deviation. The average of the positions of the top surface positions of the perceived AM and LM layers were 649.6 and 575.5 mm, respectively. The range of the identified top-surface heights of the upper and lower layers were 47.4 and 44.7 mm, respectively.

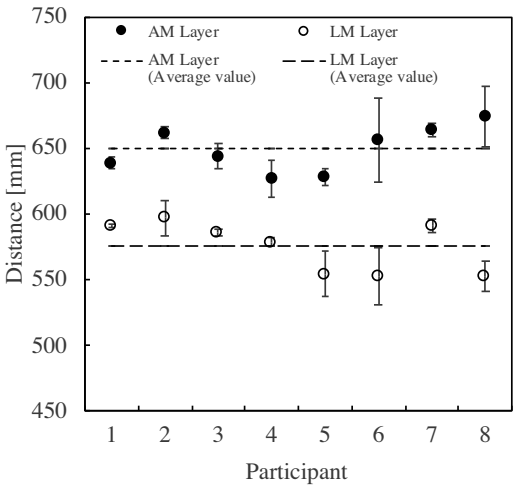

Fig. 10 Perceived top surfaces of two layers. Error bars show the standard deviations in the position that the participants identified.

B. Experiment 2

Figure 11 shows the average values of the answers for each button position of all participants. The average values of the perceived left, center and right button’s X-axis were −95.9, 1.1 and 102.5 mm, respectively.

Figure 12 shows the position of the tactile button as perceived by the palm. The origin of the graph corresponds to the X-, Y-coordinates of the center of the phased array.

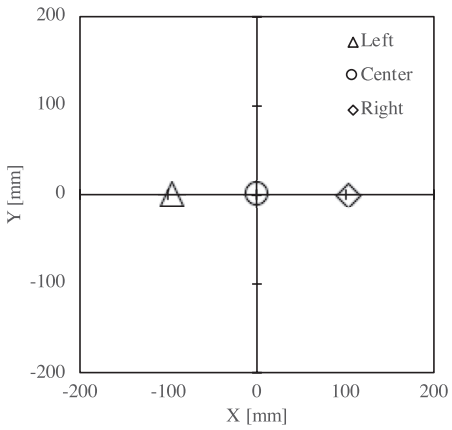

Fig. 11 Three perceived focal points. The plots show the average values of all the participants.

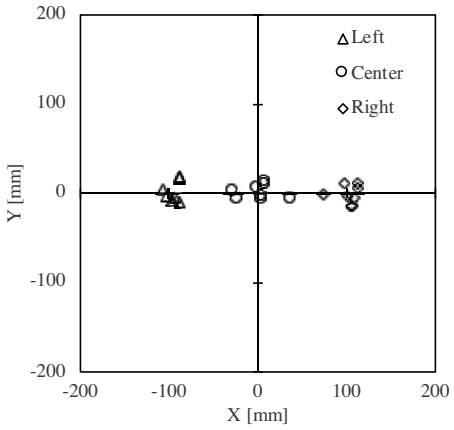

Fig. 12 Three perceived focal points. The plots show the answered value of the eight participants.

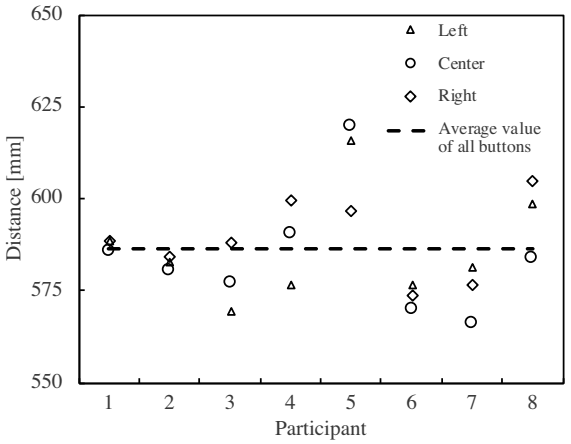

Fig. 13 Perceived top surface of the lower layer. The average value of participants’ answers for all buttons was 586.4 mm.

Figure 13 shows the Z-axis value of the participants’ answers. The average values of the perceived left, center and right button’s Z-axes were 586.2, 584.1, and 586.0 mm, respectively. The ranges in the answers regarding the heights of the buttons were 46.3 (left), 53.7 (center), and 31.1 mm (right), respectively.

6 Discussions

Experiment 1:

The results depicted in Fig. 7 show that the participants perceived the surface of each layer surface correctly. The surface of the LM layer was set to a position of 600 mm, while the average height perceived by the participants was 575.5 mm. This indicates that the perceived button was felt at a lower height than the author’s assumption. However, this result still suggests that the user’s hand stopped at the

LM layer surface and felt a two-step feedback. This indicates that the differences in stimulation between the AM and LM layers could be clearly perceived. The AM layer presents a stimulus that eases the perception of the button position. The LM layer increases the resistance to the action of pushing a button compared with the perception in the AM layer. No repulsive force exists to push the hand back, but when moving from the AM layer to the LM layer, a weak click feeling could be felt by the palm.

Experiment 2:

Among the 72 trials in experiment 2, three participants answered four times in total at different positions. This may be because they could not touch all three buttons simultaneously with their palm. However, this result indicates that the participants could operate the button correctly with a probability of 94.4%, suggesting that a sufficiently practical interface can be realized with an improved button placement.

The result of Fig. 10 shows the differences in the position of the LM layer as identified by the participants. The height of the button perceived by the participants exhibited a range of 53.7 mm in the case of the center button. One of the reasons for this error is that the haptic layer was thick. In the experiment, the participants were instructed to identify the top surface of each haptic layer, but AM stimulation and LM stimulation were presented in a range of 50 mm and 100 mm, respectively. The other factor is that the participants were not restricted when identifying the position of the haptic layer as to whether to explore from the higher side or from the lower side. Nevertheless, we confirmed that the participants could stop the button operation within the specified range after receiving two-step feedback.

7 Conclusions

A dual-layer haptic button placed in midair was proposed and evaluated in this study. A user finds the button position and its surface by AM stimulation of the user's palm. AM stimulation was provided when the user's hand was in the AM (upper) layer of a thickness of 50 mm. The completion of the click was conveyed by the LM stimulation provided when the user's hand was in the LM (lower) layer of a thickness of 100 mm.

The experimental results indicated that the top surfaces of the AM and LM layers could be recognized separately, within the errors of 12.4 and 9.4 mm, respectively, in the standard deviation. Each haptic layer could be identified without symbolic learning of tactile pattern differences. In addition, three buttons were explored within errors of 7.2 (center), 20.2 (left), and 12.9 mm (right) in the standard deviation, and the accuracy rate was 94.4%. The participants in the blind state could explore by hand where a specified button out of three was located.

References

1) R. Sodhi, I. Poupyrev, M. Glisson and A. Israr: "AIREAL: interactive tactile experiences in free air", *ACM Transactions on Graphics*, **32** (2013), 134.
2) Y. Suzuki and M. Kobayashi: "Air jet driven force feedback in virtual reality", *IEEE Computer Graphics and Applications*, **25** (2005), 44–47.
3) T. Hoshi, M. Takahashi, T. Iwamoto and H. Shinoda: "Noncontact tactile display based on radiation pressure of airborne ultrasound", *IEEE Transactions on Haptics*, **3** (2010), 155–165.
4) G. Wilson, T. Carter, S. Subramanian and S. A. Brewster: "Perception of ultrasonic haptic feedback on the hand: localisation and apparent motion", *In Proceedings of the 32nd annual ACM conference on Human factors in computing systems*, (2014), 1133–1142.
5) G. Korres and M. Eid: "Haptogram: ultrasonic point-cloud tactile stimulation", *IEEE Access*, **4** (2016), 7758–7769.
6) G. A. Gesheider, S. J. Bolanowski and K. R. Hardick: "The frequency selectivity of infor- mation-processing channels in the tactile sensory system", *Somatosensory & motor research*, **18** (2001), 191–201.
7) J. Awatani: "Studies on acoustic radiation pressure. I. (General considerations)", *The Journal of the Acoustical Society of America*, **27** (1944), 278–281.
8) T. Hasegawa, T. Kido, T. Iizuka and C. Matsuoka: "A general theory of Rayleigh and Langevin radiation pressures", *Acoustical Science and Technology*, **21** (2000), 145–152.
9) W. Frier, D. Ablart, J. Chilles, B. Long, M. Giordano, M. Obrist and S. Subramanian: "Using Spatiotemporal Modulation to Draw Tactile Patterns in Mid-Air", *In International Conference on Human Haptic Sensing and Touch Enabled Computer Applications*, (2018), 270–281.
10) R. Takahashi, K. Hasegawa and H. Shinoda: "Lateral Modulation of Midair Ultrasound Focus for Intensified Vibrotactile Stimuli", *In International Conference on Human Haptic Sensing and Touch Enabled Computer Applications*, (2018), 276–288.
11) T. Iwamoto, M. Tatezono and H. Shinoda: "Non-contact method for producing tactile sensation using airborne ultrasound", *Haptics: Perception, Devices and Scenarios*, (2008), 504–513.
12) K. Hasegawa and H. Shinoda: "Aerial vibrotactile display based on multiunit ultrasound phased array", *IEEE Trans-*

actions on Haptics., (2018), 367–377.
13) S. Inoue, Y. Makino and H. Shinoda: “Scalable Architecture for Airborne Ultrasound Tactile Display”, *In International AsiaHaptics conference*, (2016), 99–103.

伊藤　充
Mitsuru ITO
研究開発本部
技術戦略部
Technology Strategy Department
Research and Development Division

國米祐司
Yuji KOKUMAI
次世代プロジェクト本部
第三開発部
3rd Development Department
Next Generation Project Division

篠田裕之
Hiroyuki SHINODA
東京大学
The University of Tokyo

外部発表一覧（2019年）
List of papers presented/published externally (2019)

題名 Article Title	著者名 Author	掲載誌名，発表学会・協会 Journal title	巻，号，頁，年，論文番号 等 Publication information
Segmentation Method of Three Dimensional SEM Images of Biological Tissu	Kohki Konishi, Masafumi Mimura, Takao Nonaka, Ichiro Sase, Keisuke Ohta*, Hideo Nishioka*, Mitsuo Suga*	Microscopy/日本顕微鏡学会第62回シンポジウム（招待講演）	Vol. 68, Iss. Supplement_1, p. 12, November 2019
Detection of individual sub-Pixel features in Edge-Illumination X-ray Phase contrast imaging by means of dark- field channel	Norihito Matsunaga, Kazuhiro Yano, Marco Endrizzi*, Alessandro Olivo*	Journal of Physics D: Applied Physics	Vol. 53, Iss. 9, 2020, Article number 095401
Evaluation of Navigation Operations in Immersive Microscopic Visualization	Tomomi Takashina, Mitsuru Ito, Yuji Kokumai	Proceedings of the ACM Symposium on Virtual Reality Software and Technology 2019/25th ACM Symposium on Virtual Reality Software and Technology, VRST 2019	November 2019, Article No. 68
Midair Haptic Representation for Internal Structure in Volumetric Data Visualization	Tomomi Takashina, Mitsuru Ito, Yuji Kokumai	SIGGRAPH Asia 2019 Posters - International Conference on Computer Graphics and Interactive Techniques	November 2019, Article No. 45
The stability condition for the FDTD of the optical diffusion equations	Hidemitsu Toba, Satoru Odate, Katsura Otaki, Goro Nishimura*	Optical Review	Vol. 27, Iss. 1, pp. 81–89, 2020
Spectator excitement detection in small-scale sports events	Kazuhiro Abe, Chikara Nakamura, Yosuke Otsubo, Tetsuya Koike, Naoto Yokoya*	MMSports '19/27th ACM International Conference on Multimedia	October 2019, pp. 100–107
ナノフォーカスX線源を用いたスラリー中のガラス球状観察	樋口浩太，松成秀一，梅本高明	第80回 応用物理学会秋季学術講演会	応用物理学会秋季学術講演会講演予稿集（CD-ROM）Vol. 80th Page. ROMBUNNO. 20a-E305-8
すべての光学顕微鏡を扱う統一結像理論	福武直樹	第80回 応用物理学会秋季学術講演会	応用物理学会秋季学術講演会講演予稿集（CD-ROM）Vol. 80th Page. ROMBUNNO. 18a-PA1-6
反射型エシェロンを用いたテレヘルツ時間領域分光ラインイメージング	秦　大樹，原田真太郎*，浅井　岳，嵐田雄介*，片山郁文*	第80回 応用物理学会秋季学術講演会	応用物理学会秋季学術講演会講演予稿集（CD-ROM）Vol. 80th Page. ROMBUNNO. 19a-PA2-15
高信号雑音比・低歪みシングルショットテラヘルツ波形検出手法の開発	浅井　岳，原田真太郎*，秦　大樹，嵐田雄介*，片山郁文*	第80回 応用物理学会秋季学術講演会	応用物理学会秋季学術講演会講演予稿集（CD-ROM）Vol. 80th Page. ROMBUNNO. 18p-E206-1
小スポット 950 Kev 線形加速型X線源の産業用非破壊検査への応用	在家正行，松永教仁，佐藤智哉，山田篤志，鶴谷敏則，山本昌志*，畑農　督*，城野　哲*	2019年度精密工学会秋季大会	精密工学会大会学術講演会講演論文集 Vol. 2019 秋季（CD-ROM）Page. ROMBUNNO. J07（2019.08.20）冊子体：精密工学会学術講演会講演論文集, 2019, 2019A 巻, 2019年度精密工学会秋季大会，p. 419–420
ニコン初FXフォーマットミラーレスカメラの開発	尾崎浩二，斉藤義久	日本写真学会誌	2019年 82巻 3号 pp. 224–227
Development overview and practical applications in stereomicroscope with "Perfect Zoom System"	Norio Miyake, Masahiro Mizuta, Nobuhiro Shinada, Takao Nonaka, Seiji Nakano, Shoko Hara, Hirofumi Kami	Proceedings / ZooM Lenses VI - SPIE The International Society for Optical Engineering	Vol. 11106, Article Number 1110608
Fundamental properties of broadband dual-contact diffractive optical elements	Toru Nakamura, Kenzaburo Suzuki, Yosuke Inokuchi, Shiho Nishimura	Optical Engineering	Vol. 58, Iss. 8, 2019, Article Number 085103
The direct absorption measurement of fused silica, CaF2, MgF2, and sapphire at VUV and IR region	Kato Katsuyoshi, Chika Higashimura, Shunsuke Niisaka	Proc. SPIE. Laser-induced Damage in Optical Materials 2019	111731K（20 November 2019）
Phase analysis error reduction in the Fourier transform method using a virtual interferogram	Hidemitsu Toba, Zhiqiang Liu, Saori Udagawa, Naoki Fujiwara, Shigeru Nakayama, Takashi Gemma, Mitsuo Takeda*	Optical Engineering	Vol. 58, Iss. 8, 1 August 2019, Article number 084103
Midair Click of Dual-Layer Haptic Button	Mitsuru Ito, Yuji Kokumai, Hiroyuki Shinoda*	2019 IEEE World Haptics Conference（WHC）	2019 IEEE World Haptics Conference, WHC 2019 July 2019, Article number 8816101, pp. 349–352
Application of a compact X-ray source with small focal spot using a 950 keV linear accelerator	Norihito Matsunaga, Tomoya Sato, Atsushi Yamada, Masayuki Zaike, Toshinori Tsuruya, Tadashi Hatano*, Masashi Yamamoto*, Kazuaki Suzuki	International Symposium on Digital Industrial Radiology and Computed Tomography – DIR2019	NDT. net Issue - 2019-11 - Articles
High-resolution nonlinear fluorescence microscopy using repetitive stimulated transition implemented with two-color continuous-wave lasers	Fumihiro Dake, Seri Hayashi	Optics Letters	Vol. 44, Iss. 13, pp. 3402–3405, 2019
Finding an optimal algorithm for predicting human embryo development using deep learning and high-resolution time-lapse cinematography（hR-TLC）	Masafumi Mimura, Ryo Tamoto, Masakazu Sato*, Toko Shimura*, Keitaro Yumoto*, Yasuyuki Mio*	ESHRE　2019	WWW.HUMREP.OXFORDJOURNALS.ORG VOLUME 34, SUPP 1 2019 ABSTRACT BOOK ESHRE 2019 – VIENNA, AUSTRIA I 23–26 JUNE 2019, p. 176
無容器法による中赤外発光ガラスの開発（特集 ガラスの発光）Mid-infrared emitting glasses prepared by a containerless processing	吉本幸平，江面嘉信，上田　基，増野敦信，井上博之	NEW　GLASS	Vol. 34, No. 1, pp. 7–10, 2019–03
Practical method of cell segmentation in electron microscope image stack using deep convolutional neural network	Kohki Konishi, Masafumi Mimura, Takao Nonaka, Ichiro Sase, Hideo Nishioka, Mitsuo Suga	MICROSCOPY	Vol. 68, Iss. 4, pp. 338–341, August 2019
Automatic parameter setting for lens aberration control during product lot exposure	Yutaka Kanakutsu, Yukio Koizumi, Hironori Ikezawa, Shigeru Eto, Junji Ikeda, Takenori Takeuchi, Tomoyuki Matsuyama, Edward Stan*, Ronald Hiltunen*	Proceedings / Optical microlithography XXXII・SPIE-The International Society for Optical Engineering	Vol. 10961, Article number 109610M
四診システムによる不定愁訴の診断と治療	横山　楓	未来医学	2019年 No. 32 pp. 22–28
民俗芸能3Dデータアーカイブの活用による継承支援	中川源洋，笹垣信明	デジタルアーカイブ学会誌	2019年 3 巻 2 号 pp. 103–106
RtoR直描露光装置を用いた有機トランジスタ湿式作製プロセスの開発	小泉翔平，堀　正和，林田洋祐，内藤一夫，川端誠司，石垣雄大，中積　誠，岩堀恒一郎，鬼頭義昭	映像情報メディア学会技術報告	Vol. 43, No. 7 pp. 7–9
Standalone alignment technology enabling feed-forward compensation of on-product overlay errors	Takehisa Yahiro, Junpei Sawamura, Sonyong Song, Sayuri Tanaka, Yuji Shiba, Satoshi Ando, Hiroyuki Nagayoshi, Jun Ishikawa, Masahiro Morita, Yuichi Shibazaki	Proceedings / Metrology Inspection, and Process Control for Microlithography XXXIII - SPIE The International Society for Optical Engineering	Vol. 10959, Article Number 1095908
Development of 950 kV X-ray source with small focal spot using a linear accelerator	Norihito Matsunaga, Tomoya Sato, Atsushi Yamada, Masayuki Zaike, Toshinori Tsuruya, Kosuke Nakanishi*, Tadashi Hatano*, Masashi Yamamoto*, Kazuaki Suzuki	9 th Conference on Industrial Computed Tomography（iCT）2019	NDT. net Iss. 2019-03
Polarization characteristics of dark-field microscopic polarimetric images of human colon tissue	Toru Fujii, Yasuo Yamasaki, Naooki Saito, Masayasu Sawada*, Ryo Narita*, Taku Saito*, Heather L. Durko*, Photini F. Rice*, Gabrielle V. Hutchens*, Joceline Dominguez-Cooks*, Harrison T. Thurgood*, Swati Chandra*, Valentine N. Nfonsam*, Jennifer K. Barton*	Proceedings / Label-free Biomedical Imaging and Sensing（LBIS）2019	Vol. 10890, Article Number 108902J
Multispectral Mueller matrix imaging dark field Microscope for biological sample observation	Naooki Saito, Kenji Sato, Toru Fujii, Heather L. Durko*, Goldie L. Goldstein*, Alton H. Phillips*, Joceline Dominguez-Cooks*, Gabrielle V. Hutchens*, Harrison T. Thurgood*, Photini F. Rice*, Jennifer K. Barton*	Proceedings / Label-free Biomedical Imaging and Sensing（LBIS）2019	Vol. 10890, Article Number 108901A
Fluorescence characterization of heavily Eu^{3+}-doped lanthanum gallate glass spheres with high quenching concentration	Kohei Yoshimoto, Yoshinobu Ezura, Motoi Ueda, Atsunobu Masuno*, Hiroyuki Inoue*, Masafumi Mizuguchi	Optics Letters	Vol. 44, Iss. 4, pp. 875–878

*印は，株式会社ニコン外の共同研究者
*Co-researcher outside NIKON CORPORATION

Nikon Research Report Vol. 2
Published September 2020

NIKON CORPORATION